MASTER

Microfluidic single-cell encapsulation

towards a spatially controlled three-dimensional neuronal culture for brain on a chip technology

Sleeboom, Jelle

Award date:
2016

Department of Mechanical Engineering
Microsystems Research Group

Microfluidic single-cell encapsulation

Towards a spatially controlled three-dimensional neuronal culture for brain on a chip technology

Jelle J. F. Sleeboom

Committee:

Prof.dr.ir. Jaap M. J. den Toonder
Department of Mechanical Engineering
Microsystems
Dr. Regina Luttge
Department of Mechanical Engineering
Microsystems
Dr. Cecilia Sahlgren
Department of Biomedical Engineering
Soft Tissue Biomechanics & Tissue Engineering
Dr. Hans M. Wyss
Department of Mechanical Engineering
Microsystems
Alex J. Bastiaens
Department of Mechanical Engineering
Microsystems

A thesis submitted for the degree of Master of Science

Eindhoven, January 2016

Abstract

Brain disorders, such as epilepsy and Alzheimer´s disease, are becoming more prevalent in the general population. However, no adequate treatments or therapies are currently available, due to a lack of understanding of the underlying mechanisms. Since conventional research methods, such as animal models and 2D tissue cultures, do not capture the complexity of human physiology, new methods are needed to study the human brain.

Therefore, brain on a chip technology is currently being developed at Eindhoven University of Technology, in order to obtain more knowledge about the physiology of both the healthy and diseased human brain. The goal is to create a chip in which human neuronal cells can be cultured in a 3D configuration and under physiological conditions, while they can be analyzed using both optical and electronic measurement methods. One of the main challenges is to engineer a system that promotes the formation of a physiologically relevant neuronal network, while retaining the controllability, observability, and reproducibility of organ-on-a-chip technology.

In this thesis, a novel approach to control the spatial distribution of neuronal cells is presented, based on the encapsulation of single cells in hydrogel beads and subsequent bead self-assembly to create an organized three-dimensional (3D) tissue.

In order to achieve single cell encapsulation, a microfluidic flow-focusing chip with integrated temperature control was engineered, in which cells can be encapsulated in Matrigel droplets with a dispersity of below 3%. Cell encapsulation took place at a temperature below 4°C, after which bead gelation was initiated by transporting the droplets to a region at 37°C on the same chip. The cells are shown to survive the encapsulation process, and remain viable over at least 9 days, as shown by live/dead cell staining. Moreover, the cells retain their potential for differentiation inside the Matrigel beads, as indicated by the formation of neurites and inter-cellular connections in the established 3D cultures. The cells also stained positively for the neuron specific protein β-tubulin III. Organization through self-assembly of the manufactured beads was demonstrated inside oil, and recommendations are provided for microfluidic approaches to achieve self-assembly in cell culture medium.

In future work, the method can be applied in the 3D bioreactor for neuronal cell culture that is currently under development, aiming to enhance the experimental reproducibility, facilitate the formation of a 3D spatially standardized neuronal network, and enable more advanced co-culture brain models. Additionally, the method can be applied to create spatial organization in other organ-on-a-chip applications.

Preface

> The more comfortable we become with being stupid, the deeper we will wade into the unknown and the more likely we are to make big discoveries.
>
> ---
>
> Martin A. Schwartz

When I was younger, I always wanted to be an inventor, dreaming of big machines, rockets, and airplanes. There is an audio recording from me in my youngest days, where I'm trying to explain to my mother – she was very patient with me – that the universe is infinite. I believe I was still in primary school at that time, and feeling very smart. I also knew perfectly well what rockets were made of: *Dingetjes, dangetjes, en dongetjes*, which roughly translates to *stuff, staff, and stoff.* Needless to say, I was well prepared for a scientific career.

Now, about two decades later, I can proudly present you this thesis, which is the fruitful result of many months of hard work. During my endeavor, I've spent countless days in the microfab lab, trying to develop new technology and answer difficult questions. I also encountered seemingly simple questions, such as "*What is this gooey mess?*", or "*How do I get this thing watertight?*". Not being able to directly answer these questions made me feel very stupid at times, but eventually – and with support from my amazing colleagues – I always managed to find some solutions that worked. And that's the key reason I have also thoroughly enjoyed myself; I got to play around with high-tech machinery in the lab, mess up, try again, and eventually achieve something new.

Of course, I wouldn't be here today if it wasn't for the support of many people. Firstly, I'd like to thank Jaap den Toonder, Regina Luttge, and Alex Bastiaens, for their excellent supervision and for giving me the opportunity to work on this interesting project. I'd also like to thank my other colleagues for their support, interesting discussions, and encouragement during my time in the lab. I am looking forward to continue to work with all of you in the Microsystems group.

I would also like to thank my family, girlfriend, and friends for always supporting me. I would probably have perished in the lab if you hadn't occasionally told me to relax a bit more. In honor of my father, who would have been immensely proud of me, I have included one of his most beautiful poems on the next page.

Laatste reis

Ik weet niet hoe het zijn zal in die dagen
wanneer ik scheep ga voor de laatste reis:
zal dan mijn schip de laatste storm verdragen
en landen aan Gods eeuwig paradijs?

Want ik weet niet hoe lang de tocht zal duren
en welke haven ik voorgoed verlaat.
Zal ik dan zwijgend in de verte turen
en alles wat ik schreiend achterlaat

niet zachtjes langs de reling horen klagen,
of zal de wind, hoog gillend in de mast,
alleen de stem van storm en branding dragen
waarin mijn ziel zich van zijn angst ontlast?

Neem mij, heer God, het roer dan maar uit handen
en laat me zingend op de voorplecht staan;
dan zal mijn schip niet op de rotsen stranden
maar veilig in Uw haven binnengaan.

Freerk Jan Sleeboom
In de naam van de vader

Contents

List of Figures

List of Tables

Chapter 1

Introduction

Neurological disorders that arise from disruptions of the brain cellular network, such as epilepsy and Alzheimer's disease, are becoming more prevalent in the general population [1, 2]. However, no adequate treatments or therapies are currently available, due to a lack of knowledge about the underlying mechanisms. Therefore, new strategies for investigating these mechanisms are required.

In a healthy brain, cognitive functions arise from coordinated interactions between large numbers of interconnected cells, distributed over specialized regions in the brain [3]. An adult male human brain contains approximately 86.1 billion neurons, and 84.6 billion non-neuronal, supportive cells [4], such as astrocytes, microglia, and oligodendrocytes. Neurons constitute neuronal networks, and can receive and send signals through extensions from their cellular membrane, referred to as dendrites and axons. Signals are transferred between neurons via neurotransmitters in synapses, where axons and dendrites connect. Astrocytes are a type of glial cell, responsible for maintaining homeostasis in the brain, but also involved in the regulation of neuronal interaction [5]. Microglia are the immune cells of the central nervous system, also thought to be involved in the shaping of cellular networks [6]. Oligodendrocytes are mainly responsible for electrically insulating axons to increase signal propagation speed, by enveloping them in a myelin sheath [7].

When the intricate network in the brain is disrupted, breakdown of the coordinated interactions required for normal brain functionality can lead to a number of diseases. For epilepsy, disruption of interactions between neurons can lead to seizures, characteristic for this disorder. Although generally, epilepsy is viewed as caused by excessive synchronization of firing neurons, recent findings indicate that more complex changes in synchronization of interacting neurons are the underlying causes of seizures [8]. Alzheimer's disease, one of the most common causes of dementia, is a neurodegenerative disease that is characterized by the buildup of protein plaques and breakdown of myelin sheaths. As a result, neuronal cells are damaged and the propagation speed of electrical signals is reduced, disrupting the normal communication between neurons [9].

It is clear that in order to gain a deeper understanding of the mechanisms that lead to these disruptions, studying cellular interactions in neuronal networks is essential. Currently, the most common research tools for studying the brain are animal models, brain slice cultures, and 2D neuronal cell cultures. Animal models for disorders such as epilepsy [10] and Parkinson's disease [11] have greatly contributed to our knowledge and the development of therapeutics. However, the translation of data from animal models to human biology is limited [12]. Newly developed epilepsy models, for instance, did not contribute to the development of more effective treatments [13]. Moreover, animal models are very expensive, which is illustrated by the estimated $330,000 cost of pre-clinical drug testing for just one compound [14].

Brain slice cultures have been employed for studying stem cell therapies for neurological disorders [15], and for studying development of epilepsy in the brain [16]. These cultures are established from live tissue, and can be kept alive for several weeks. The main advantages over animal models are the reduced cost and the increased ability to measure molecular and cellular processes at the small scale, while retaining the *in vivo* tissue characteristics. However, in these cultures the viability of neurons decreases over time, while other cells, such as microglia become highly proliferative. This changes the cellular composition, reducing the representativeness of the slice for *in vivo* physiology. Additionally, since these cultures are established from variable living sources, there is a need for many experiments to gain statistical significance. The most important limitation, however, is that brain slices offer no control over the local environment, such that no systematic variation of environmental factors is possible [17].

Two-dimensional (2D) neuronal cultures have been employed to overcome some of the issues associated with the previously described methods, providing a basis for systematic variation of environmental factors, and reducing variability. Moreover, culturing cells *in vitro* enables the integration of components that facilitate measurements at the cellular level. These planar cultures have for instance been used to evaluate the impact of several drugs on the electrophysiology of a randomly formed network of dissociated cortical neurons, measured using a microelectrode array [18].

A key challenge in these *in vitro* models is the application of the right environmental cues to not only elicit network formation, but also control it. During brain development, neurites are guided by different cues, such as diffusible growth factors, substrate-bound factors, electrical and magnetic fields, and topological features [19, 20]. By incorporating such factors in the culturing system, network formation can be guided. For example, spatially controlled network formation has been achieved through local micropatterning of the culture substrate with an adhesion promoting material, such that reproducible measurements of neurotoxicity could be performed [21].

The main limitation of these 2D cultures, however, is the fact that these models generally do not fully recapitulate *in vivo* cell behavior, which is related to the difference in adhesive, topographical, mechanical, and soluble cues the cells are exposed to. *In vivo*, neuronal cells reside in a three-dimensional (3D) soft extracellular matrix (ECM), while in 2D they reside on a flat surface with typically high stiffness [22]. An illustration of the enormous impact on neuronal cells is the differential expression of over 1700 genes in a 3D collagen gel as opposed to planar culture conditions [23]. Thus, 3D brain tissue models are essential for studying cellular interactions in a physiologically relevant context. However, directing the formation of a neuronal network in 3D is more challenging.

Several different approaches have been investigated for directing the cellular growth, distribution, and alignment in 3D neuronal cultures. For instance, the growth of primary cortical neurons was guided in 3D by an organized packing of spherical silica beads. Additionally the developed tissue was connected to a 2D microelectrode array (MEA), such that the different electrophysiological properties of 3D networks as opposed to 2D networks could be assessed [24]. Another example is the use of nanostructured superhydrophobic substrates to direct 3D neuronal growth in a suspended culture [25]. However, despite the 3D conformation of the formed neural networks, these approaches still do not accurately mimic the ECM that cells normally reside in.

Therefore, multiple researchers have developed methods to direct neuronal cell development and network formation in 3D scaffolds that mimic the ECM. For instance, a 3D scaffold that mimics the mechanical properties of the ECM has been developed for culturing primary hippocampal neurons [26]. Other methods rely on the 3D structuring or patterning of hydrogel materials whose properties resemble those of the ECM. For example, protein fiber alignment in Matrigel, achieved through gelation under continuous flow, was used to direct neurite outgrowth [27]. In other work, a micropatterned hydrogel matrix, containing both growth permitting and growth inhibitive materials, was used to direct axonal outgrowth [28]. For control over the distribution of neuronal cells, a microchanneled bi-modal hydrogel was employed, enabling control over cellular spacing in one direction [29].

Despite these advances in controlling network formation in 3D cultures, some important challenges still remain. First, the increased complexity of 3D tissue models has reduced the experimental reproducibility, which is essential for generating reliable data [30]. Second, the distribution of cells throughout a 3D culture can greatly influence the formation of a network, but control over the position of individual cells is yet to be achieved.

Therefore, the main challenge addressed in this work is to engineer a system that promotes the formation of a physiologically relevant neuronal network in an ECM mimicking hydrogel, while retaining reproducibility by controlling the 3D spatial distribution of neuronal cells. In order to tackle this challenge, a novel approach to control the 3D spatial distribution of neuronal cells is presented, based on the encapsulation of single neurons in hydrogel beads and subsequent self-assembly of these bead to create an organized 3D tissue. By tuning the dimensions of the self-assembling beads, the spacing between individual neurons can be controlled.

1.0.1 Project goals and outline

The main aim is to develop an approach for spatially organizing neurons in a 3D cell culture, by encapsulating single neuronal cells into monodisperse hydrogel beads, and using the self-assembling properties of these spherical beads to create a 3D tissue (Figure 1.1). This technology is developed for future use in a bioreactor, originally developed by B. Schurink and R. Luttge [31], which is currently being further developed at Eindhoven University of Technology. The main aim of this reactor is to provide an appropriate microenvironment for 3D culture of neuronal cells, while facilitating electrical measurements using a microelectrode array (MEA) [32].

Currently, cells from the SH-SY5Y neuroblastoma cell line are used in the bioreactor. These cells can be differentiated into neurons by applying external chemical cues. When the cells are differentiated, neuron specific markers are expressed, such as β-tubulin III, which is a cytoskeletal component [33]. Additionally, the SH-SY5Y cells can become electrically active [34]. The advantages of using this cell line is that large numbers of cells are readily available, as opposed to primary neurons, which have to be isolated prior to each experiment.

The 3D culture of SH-SY5Y cells in the bioreactor is established in growth-factor reduced Matrigel, a solubilized basement membrane preparation extracted from mouse sarcoma. This matrix material has a stiffness between 200 and 500 Pa, which is comparable to brain tissue [32]. Using Matrigel, successful 3D cultures have been established, in which SH-SY5Y cells could be induced to differentiate and form networked structures, with a cell morphology similar to *in vivo* neurons. The same hydrogel material and cell line is used in this thesis, because of the described advantages, and in order to facilitate future integration of the developed technology.

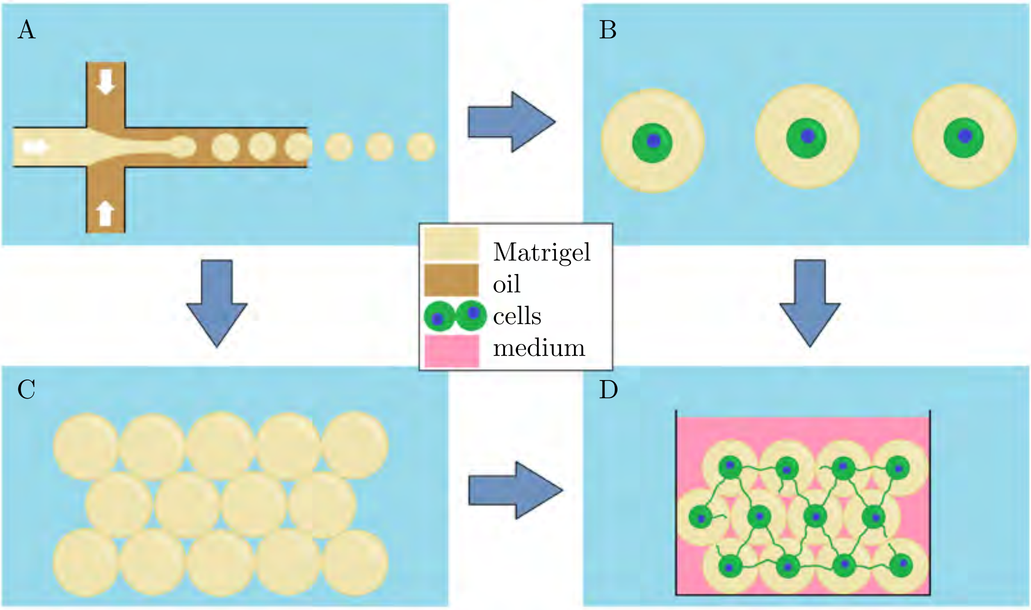

Figure 1.1 – Schematic overview of the proposed technology: Microfluidic generation of Matrigel beads (A), microfluidic encapsulation of SH-SY5Y cells in Matrigel beads (B), self-assembly of the beads (C), and a spatially organized neuronal culture from encapsulated SH-SY5Y cells (D).

Several sub-goals are defined to develop the spatially organized culture (Box 1). First, a microfluidic system has to be developed that can generate monodisperse Matrigel beads. The temperature of this device has to be controlled in order to achieve this, since Matrigel is liquid only at low temperatures [35]. Second, single SH-SY5Y cells have to be encapsulated in Matrigel beads, while retaining their viability and differentiation potential. Third, using the self-assembling properties of spherical particles, the beads have to be assembled in an organized 3D stacking. Combined with the encapsulation of cells, this should facilitate the formation of a spatially organized neuronal culture, that is able to form a network.

BOX.1: The aims of this project.

1. Develop a temperature control method for a microfluidic droplet generator
2. Implement the developed temperature control method in a microfluidic device that can generate monodisperse Matrigel beads.
3. Achieve single-cell encapsulation in monodisperse Matrigel beads of live SH-SY5Y cells.
4. Assemble the encapsulated cells into an organized and viable culture, that can form a network.

The structure of this thesis reflects the defined sub-goals: First, relevant theoretical background on physics at the microscale and an overview of relevant microfluidic technologies is provided in chapter 2. Using the information from this chapter, the microfluidic device to achieve the first three sub-goals is designed in chapter 3. The design is then separately assessed with respect to the first three goals: The developed temperature control method is validated in chapter 4, the generation of monodisperse Matrigel beads is tested in chapter 5, and the encapsulation of single SH-SY5Y cells is tested in chapter 6. Next, the final goal is treated in chapter 7: Assembling a spatially organized, viable, differentiated, and network forming cell culture. Finally, the main conclusions of this work are presented in chapter 8, along with recommendations for future work on the spatial organization of cells through encapsulation.

Chapter 2

Microfluidics: Relevant background and theory

Microfluidics – the science of manipulating fluids at the micrometer scale – has found its way into many biological applications over the past few decades, such as DNA amplification by polymerase chain reaction (PCR) [36, 37, 38, 39], directed evolution of enzymes [40, 41], single-cell analysis [42, 43, 44], and tissue engineering [45, 46]. The main reason for this trend towards small scale systems is the unprecedented level of control over flow parameters, such as pressure, temperature, shear stress, and concentration, that is achievable in microfluidics. This useful property arises from the fact that the physics of fluids at this scale are dominated by different forces than at a macroscopic scale, resulting in predictable and controllable fluid behavior.

Apart from the achievable level of control, some other properties of microfluidic technology make it an excellent tool for biological research. First, microfluidic systems inherently work with small volumes, which is an advantage for working with samples that are either very costly or only available in small volumes, as is the case in most biological applications. Second, the fabrication methods used to produce microfluidic systems, originating from the microelectronics industry, enable the integration of a multitude of measurement techniques into the same microfluidic device, such as optical, electrical, and magnetic methods. Finally, microfluidic systems operate at similar length scales as biological systems, such that for example physiological mass-transport properties and biomechanical stresses and strains can be accurately replicated. This enables the creation of *in vitro* tissue models, in which live cells are cultured in an environment that provides the physiologically relevant cues to elicit recapitulation of the function and behavior of the *in vivo* tissue it represents.

One of the microfluidic technologies that has gained considerable attention is droplet microfluidics, which is based on high-throughput generation and handling of droplets as isolated sample containers. These droplets can be generated at high rates and with low dispersity, and used, for example, for isolated (bio-) chemical reactions or directed evolution. In the context of this thesis, the main focus will be on the use of droplet microfluidics for cell encapsulation.

In this chapter, physical principles that are relevant to microfluidic systems are discussed in section 2.1, after which a more in depth review of droplet microfluidics is provided in section 2.2. Next, cell encapsulation methods are reviewed in section 2.3. Finally, temperature control methods for microfluidic systems are discussed in section 2.4.

2.1 The physics of microfluidics

Physical principles at the microscale relevant to cell encapsulation are discussed in this section. This includes the physical mechanism behind laminar flow in microfluidic systems, and the importance of interfacial forces. Additionally, diffusion at the microscale is briefly discussed. This section is by no means exhaustive. For a complete overview of the physics relevant to all microfluidic systems, the reader is referred to more extensive reviews in literature [47, 48].

2.1.1 Viscous forces and flow

As stated before, different forces dominate the behavior of fluids at the micro-scale. One of the main differences is the relative influence of viscous and inertial forces on fluid flow. The importance of inertial forces relative to viscous forces can be estimated by evaluating the dimensionless Reynolds number (Re), shown in equation 2.1. Here, U is the characteristic velocity, L the characteristic length, ν the kinematic viscosity of the fluid.

$$Re = \frac{UL}{\nu}, \tag{2.1}$$

Re can be derived from the dimensionless incompressible Navier-Stokes equation, as shown in equation 2.2, where $\vec{u^*}$ is the dimensionless local velocity vector, t^* the dimensionless time, and p^* the dimensionless pressure.

$$\frac{\partial \vec{u^*}}{\partial t^*} + \vec{u^*} \cdot \nabla \vec{u^*} = -\nabla p^* + \frac{1}{Re} \nabla^2 \vec{u^*} \tag{2.2}$$

Due to the small length scales in microfluidics, Re is typically in the low $\mathcal{O}(10^{-6}) - \mathcal{O}(10)$ range, indicating that the fluid flow is dominated by viscous forces [48]. As a result, fluid flow is almost always laminar in microfluidic systems, and therefore highly predictable.

Solving the Navier-Stokes equation for a microfluidic channel yields the velocity field as a function of the pressure difference over the length of the channel, which can be integrated to yield the relation between pressure and flow-rate (Q). For a circular channel with radius R and length L, transporting a liquid with dynamic viscosity μ, this solution is shown in equation 2.3.

$$\Delta p = \frac{8\mu L Q}{\pi R^4} \tag{2.3}$$

This equation can also be written as in equation 2.4, where R_h is the hydraulic resistance of the channel. This is the generalized form of the relation between pressure and flow-rate for laminar, low Reynolds number flow, in which the hydraulic resistance depends on the fluid viscosity, and channel dimensions. For channels with circular cross-section, R_h can be derived from equation 2.3: $R_h = 8\mu L/\pi R^4$.

$$\Delta p = R_h \cdot Q \tag{2.4}$$

Equation 2.4 is very similar to Ohm's law ($U = I \cdot R$), which describes the relation between electric potential U, electrical resistance R, and current I. Using this analogy, the pressure differences and flow-rates in large and complex microfluidic circuits can be computed using the same laws for parallel and serial connections in electrical circuits.

However, most microfluidic devices contain square or rectangular channels, due to the fabrication methods that are used to manufacture them. For high aspect ratio rectangular channels, the hydraulic resistance can be approximated using $R_h = \frac{12\mu L}{wh^3}$, where h is the channel height and w the channel width, which is valid for $h << w$. For square and low aspect ratio ($w = h$) rectangular channels, expressions for the hydraulic resistance and velocity (u) have been derived analytically, as shown in equations 2.5 and 2.6 [49].

$$R_h = \frac{12\mu L}{wh^3} \left[1 - \frac{h}{w} \left(\frac{192}{\pi^5} \sum_{n=1,3,5,...}^{\infty} \frac{1}{n^5} tanh\left(\frac{n\pi w}{2h} \right) \right) \right]^{-1} \tag{2.5}$$

$$u(x,y) = \frac{16a}{\mu\pi^3} \left(-\frac{dp}{dz} \right) \sum_{n=1,3,5,...}^{\infty} (-1)^{(n-1)/2} \left[1 - \frac{cosh(n\pi y/2a)}{cosh(n\pi b/2a)} \right] \times \frac{cos(n\pi x/2a)}{n^3} \tag{2.6}$$

In equation 2.6, a and b refer to half the channel height and width (Figure 2.1 A). Using this equation, the velocity distribution throughout the channel cross-section can be computed (Figure 2.1 B).

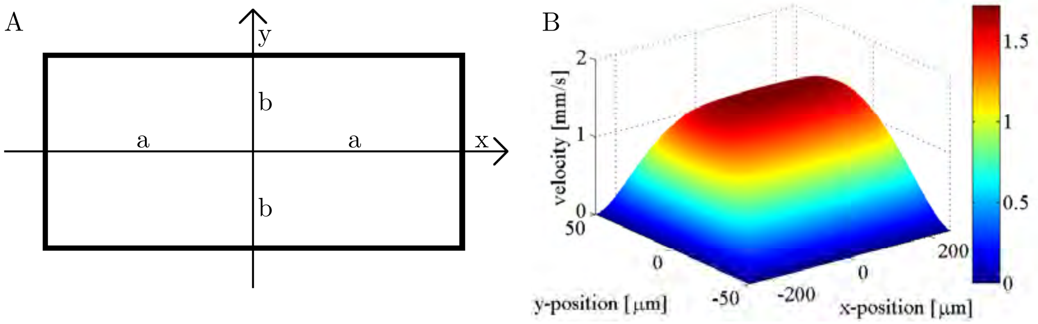

Figure 2.1 – The dimensions of a rectangular channel (A), and an example of the velocity distribution for a 100x500 μm channel subject to a flow-rate of 3 μL/min, calculated using equation 2.6 (B). The ratio between the x and y axes is not to scale.

2.1.2 Interfacial effects

At the microscale, the ratio between surface area and volume can be several orders of magnitude higher than at the macroscopic scale, such that the relevance of all surface effects increases relative to the bulk fluid properties. This includes all types of interfaces between solids, fluids, and gases. The interaction between water molecules and a solid surface, for instance, determines the contact angle of a water-air interface inside a microchannel. When this angle is less than 90°, the surface is referred to as hydrophilic or *wall-wetting*, and the surface tension at the water-air interface can physically force the water interface forward in a microchannel. This mechanism is referred to as capillarity, and can be used to passively fill a microchannel, without providing an external driving force.

In this context, both the properties of the solid and the liquid can have an enormous influence. If the surface is rendered hydrophobic, for instance, the interface curves in the opposite direction. This causes the capillary effect to change direction, forcing the liquid out of the microchannel.

Fluid motion at the microscale as a result of capillarity is determined by the interplay between viscous and interfacial forces. The relative importance of surface tension relative to viscosity can be estimated using the capillary number (Ca) given in equation 2.7, where μ is the dynamic viscosity of the fluid, U the characteristic velocity, and γ the interfacial tension between the two phases.

$$Ca = \frac{\mu U}{\gamma} \tag{2.7}$$

Naturally, the physical properties of interfaces are highly relevant to droplet generation, since this involves their deformation and breakup. This is discussed in more detail in section 2.2.

2.1.3 Diffusion and mixing

An effect of the laminar flow at the microscale is that there generally are no convective mechanisms to induce mixing, as opposed to the chaotic, turbulent mixing mechanisms present at the macroscale. This means that mixing in microfluidics is dominated by diffusion. Since this mechanism is typically slow, driven by Brownian motion, concentration gradients within microchannels tend to have a long lifespan.

The importance of convection relative to diffusion can be estimated using the dimensionless Péclet number, defined in equation 2.8, where U is the characteristic velocity, L the characteristic length, and D the mass diffusion coefficient.

$$Pe = \frac{UL}{D} \tag{2.8}$$

A high Péclet number (Pe) indicates that convection is dominant over diffusion. When this is the case, mixing is typically very slow, due to the lack of turbulent mixing mechanisms in laminar flow. This enables the presence of two co-flowing streams in which virtually no mixing occurs. By tuning the flow-rate and channel dimensions, the relative influence of convection can be modified, which enables the controlled generation of precise concentration gradients.

2.2 Droplet microfluidics

In microfluidics, a wide range of techniques for the generation and manipulation of droplets are available. Most commonly, monodisperse droplets are generated in passive nozzles with flow-focusing, co-flowing, or T-junction geometries (Figure 2.2). All of these methods are referred to as passive droplet generation methods. They rely on the flow field to deform the interface between two phases and promote the growth of interfacial instabilities, leading to the breakup of a fluid stream into droplets. Since flow-focusing enables a larger flexibility in droplet size tuning, this method is used for cell encapsulation, and discussed in more detail in this section. For more information regarding co-flowing, T-junction, and other droplet generation methods, the reader is referred to more elaborate reviews of droplet microfluidics [50, 51, 52].

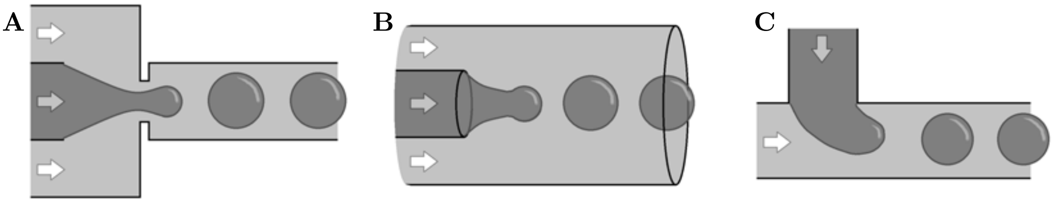

Figure 2.2 – Schematic images of the most common microfluidic droplet generators: Flow-focusing (A), co-flowing (B), and T-junction (C) geometries.

In a microfluidic flow-focusing droplet generator, first implemented by Anna et al. [53], both the dispersed and continuous phase are forced through an orifice. The continuous phase flows from two channels on either side of the dispersed phase, enveloping the center dispersed phase fluid stream. In this region, both phases are subjected to large elongational flow, drawing the inner fluid into a jet that breaks up into droplets. In order to prevent droplet coalescence in the downstream channel, interface stabilizing surfactants are generally added to the continuous phase.

Several droplet generating regimes have been reported, of which the dripping and jetting regimes are the most common. The dripping regime (Figure 2.3 B) is characterized by droplet breakup very close to the flow-focusing contraption, generating highly monodisperse droplets that have a size similar to the orifice width. The jetting regime (Figure 2.3 C) is characterized by the formation of a long jet that breaks up further downstream, typically creating more polydisperse droplets.

In both regimes, the process is dependent on a number of fluid parameters, such as the viscosities, the flow-rates, and the surface tension at the interface. Moreover, the geometry and surface properties of the flow-focusing orifice have a large influence on the generation process. However, no model exists that can reliably predict the droplet size and generation frequency as a function of the flow parameters and device dimensions [51]. Fortunately, many experimental and numerical studies have been performed to obtain scaling laws, based on the dominant physics in each regime.

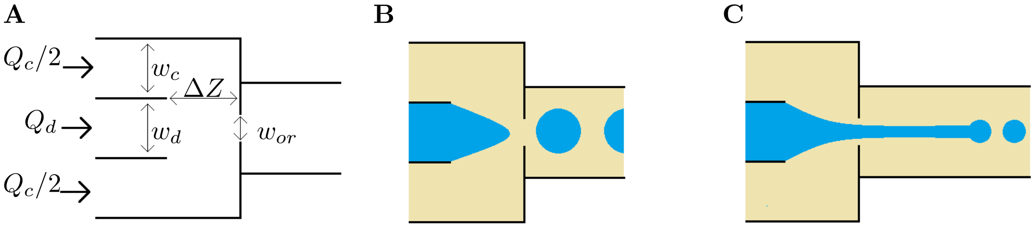

Figure 2.3 – The dimensions of a typical flow-focusing device (A), and schematic representations of two common droplet generation regimes: Dripping (B), and jetting (C).

It is common to evaluate droplet breakup as a function of the flow-rate ratio $\phi = Q_c/Q_d$ and a modified capillary number (Ca_m), where Q_c and Q_d are the volumetric flow-rates of the continuous and dispersed phase respectively. The modified capillary number, shown in equation 2.9, is based on the viscosity of the continuous phase μ_o, and the effective elongation rate $G = \Delta V/\Delta Z$ [54]. Here, γ is the surface tension, μ_o the dynamic viscosity of the continuous phase, and ΔZ the distance between the dispersed phase channel and the orifice. ΔV is the velocity difference experienced by the continuous phase: $\Delta V = V_{orifice} - V_{upstream}$, where $V_{upstream}$ is the average velocity of the continuous phase upstream of the flow-focusing section, and $V_{orifice}$ is the average velocity of the continuous phase in the orifice.

$$Ca_m = \frac{\mu_o G w_d}{2\gamma} = \frac{\mu_o \Delta V w_d}{2\gamma\Delta Z} = \frac{\mu_o w_d Q_c}{2\gamma h \Delta Z}\left[\frac{1}{w_{or}} - \frac{1}{2w_c}\right] \tag{2.9}$$

In equation 2.9, w_{or} is the width of the orifice, w_c the width of the continuous phase channels, and w_d the width of the dispersed phase channel (Figure 2.3 A). Another relevant dimension is the channel height h. The modified capillary number is independent of the viscosity of the dispersed phase, since the shearing effect of the continuous phase flow is mostly responsible for drawing out the dispersed phase.

In the dripping regime (Figure 2.3 B), typically found at low capillary numbers, a combination of physical mechanisms is responsible for droplet breakup: Rayleigh capillary instability, end-pinching, and viscous drag. Viscous drag draws out a finger from the dispersed phase liquid, forming a neck. The Rayleigh instability arises from small perturbations along the neck, that eventually lead to droplet pinch-off by surface tension. End-pinching refers to the pinching effect of an increase in pressure around the neck. This increase arises when the dispersed fluid is drawn into the orifice, limiting the flow of the continuous phase. This causes pressure to build upstream of the orifice, effectively squeezing the neck. The droplets generated in this regime are roughly equal to or smaller than the orifice size, depending on the capillary number and flow-rate ratio. The diameter decreases with increasing capillary number and decreasing flow-rate ratio.

For higher capillary numbers, the dripping regime transitions into the jetting regime (Figure 2.3 C). This occurs when the Rayleigh instability, which normally contributes to droplet pinch-off, is carried downstream before the disturbances can be amplified. The transition also occurs when inertial forces become more important than interfacial forces, as indicated by the Weber number $We = ReCa$. No exact We limit is known for the transition to the jetting regime in a flow-focusing device, but in a three-dimensional co-flowing device the transition occurs when the sum of Ca and We is approximately 1 [55]. The droplets generated in this regime are typically more polydisperse, as it relies on the more unstable Rayleigh plateau instability. Droplet sizes scale with the product of the characteristic pinch time and the flow-rate of the dispersed phase [51].

Important to note is that, as mentioned before, fluid-solid interactions can greatly influence the formation process of droplets. All theory up until now has been focused on the case where the continuous phase is wall-wetting, causing it to envelop the finger formed by the dispersed phase. However, when the continuous phase is not wall-wetting, the dispersed phase might adhere to the wall, disturbing the generation process.

Flow-focusing devices can be operated by either applying a controlled pressure difference over the device, or by enforcing a flow-rate, which is typically achieved using a syringe pump. However, flow-rate control enables more gradual control over the droplet size compared to pressure control [56].

2.3 Cell encapsulation techniques

Most cell encapsulation techniques are based on the previously discussed droplet generation technology, by suspending cells in the dispersed phase. However, several important factors have to be taken into consideration when encapsulating live cells. This includes the (bio-) chemical properties of the environment and the mechanical stresses the cells are subjected to. These factors are discussed in a brief review of cell encapsulation techniques and their application. Another important property of cell encapsulation from suspension is that the distribution of cells throughout the generated droplets is stochastic in nature, which is discussed in more detail in section 2.3.1. At the end of this section, and overview table of all discussed encapsulation methods is found (table 2.1).

In high throughput screening applications, cells are generally encapsulated in aqueous droplets, and maintained for some time. After subjecting them to biochemical factors, such as different drugs, assays can be performed to test for cell viability, or the presence of a specific compound. A fluorescent assay for cell viability has for instance been employed in droplets to perform a toxicity assay on human lymphoblasts. Based on the fluorescent signals, a dose response curve could be derived using a library of different concentrations of mitomycin C [57]. Other applications include the screening of antibiotics against bacteria inside microparticles [42], and the screening and selection of single hybridoma cells for their ability to generate certain antibodies [43].

Especially in this type of screening application, the properties of both the oil and surfactant in the continuous phase can have a large impact on the survival rate of cells, since cells typically reside inside the droplets for a significant amount of time. Moreover, proteins can be adsorbed or denatured by the interface, interfering with the biological processes inside the droplet. Therefore, much research has focused on *biocompatible* oils and surfactants, a term that refers to materials that do not negatively influence cell viability and function.

Traditionally, hydrocarbon oils such as mineral oil and hexadecane are used as the continuous phase in droplet generators. For this type of oil, many different surfactants are commercially available. The downside of using hydrocarbon oils is that they are generally not very permeable to gases, such as oxygen and carbon dioxide, which results in rapid cell death due to the lack of gas exchange. Additionally, some hydrophobic compounds can phase partition into the oil, which limits the containing properties of the droplets. These oils are thus not biocompatible when used for longer term cell cultures in droplets.

Therefore, fluorinated oils have gained considerable attention for cell culturing in droplets. These oils are highly soluble to gases and insoluble to most organic compounds [58]. The downside of using fluorinated oils is that only a limited number of fluorosurfactants is commercially available, all of which have questionable biocompatibility. An example is Krytox (DuPont), which consists of perfluoropolyether with a carboxylic head group (PFPE-COOH). Through chemical synthesis, researchers have replaced the carboxylic head group with several alternative groups to improve the biocompatibility of this commercially available fluorosurfactant. Currently a block-copolymer of perfluoropolyether and polyethylene glycol (PFPE-PEG) is the most promising fluorosurfactant in terms of biocompatibility [58]. Alternatively, a block-copolymer of perfluoropolyether and dimorpholinophosphate (PFPE-DMP) has shown similar biocompatibility and better emulsion stability [59].

Next to high-throughput screening, another application of cell encapsulation is the controlled generation of 3D micro-tissues, by encapsulating cells in hydrogel. This is typically achieved by first encapsulating cells inside droplets of liquid hydrogel, after which solidification of the gel is induced by some external stimulus. In both flow-focusing and T-junction geometries, several different hydrogels have been used to encapsulate cells, such as Alginate [60, 61, 62, 63, 64, 65, 66], Agarose [42, 67], Extracel [68], Puramatrix [66], hPG-PEG [69], and Matrigel [70]. These gels are

Table 2.1 – Summary of microfluidic cell encapsulation techniques

Method	Material	Oil / surfactant	Cell Types	Ref.
Flow-focusing	Aqueous solution	FC-40/PFPE-PEG	HL60	[71]
		HFE-7500/PFPE-PEG	PC9	[44]
		FC-40/PFPE-DMP	Jurkat cells, HEK293T	[59]
		n.a./carboxy-PFPE	monocytic U937 cells	[57]
		mineral oil/Span 80	Jurkat cells	[72]
		HFE-7500/EA surfactant	hybridoma cells	[43]
		FC-40/PFPE-PEG	2C6 hybridoma cells	[73]
	Alginate	oleic acid/-	P19 EC, MCF7, HepG2	[60]
		oleic acid/-	P19 EC	[61]
		Hexadecane/Span-80	HeLa cells	[63]
		Novec 7500/PFPE-PEG	9E10, M6C	[62]
	Agarose	mineral oil/Span80	*Escherichia coli* cell	[42]
	Extracel	perfluoropentane/PFPE-PEG	HCT116	[68]
	hPG-PEG	paraffin oil/-	Yeast cells, fibroblasts, lymphoblasts	[69]
	Matrigel	HFE-7500/PFPE-PEG	RWPE1,MCF10A-GFP	[70]
T-junction	Aqueous solution	silicone oil/Span-85	Mouse mast cell mitochondrion, mouse B lymphocytes	[74]
	Alginate	corn oil/lecithin	Jurkat cells	[64]
		hexadecane/Span-80	Yeast cells	[65]
	Agarose	mineral oil/Span-80	mES	[67]
	Alginate, Puramatrix	mineral oil/Span-80	HepG2	[66]

either synthetic, such as hPG-PEG, or derived from natural proteins, such as Matrigel. Synthetic hydrogels have the added advantage of full control over their composition and chemistry, while nature derived hydrogels usually offer a more physiological environment due to the present growth factors and adhesion proteins. The application of either type is dependent on the type of cell used, as well as the purpose of the experiment.

The gelation method for hydrogels can also influence cell viability, especially when reagents are required to induce cross-linking, such as for Alginate. For this gel, Ca^{2+} ions are used to induce gelation. However, the methods used to bring Ca^{2+} ions in contact with the alginate droplets can adversely affect cells. When Ca^{2+} ions are introduced in oleic acid, the change in pH can significantly reduce cell viability. In order to overcome this, a device has been developed to rapidly exchange the oil after gelation [60]. Another method of introducing Ca^{2+} ions is the co-encapsulation of $CaCO_3$ nanoparticles and subsequent exposure to acetic acid. However, the nanoparticles can physically damage cells when colliding inside the droplet, which has been solved by introducing a heterogeneous encapsulation approach that separated the cells from the particles [62]. It is clear that the gelation of droplets introduces another step during which cells can be negatively affected, and innovative solutions are required in order to achieve successful encapsulation in hydrogel beads.

For Matrigel specifically, the temperature conditions can be detrimental to cells. Prolonged cell exposure to the low temperature at which Matrigel is liquid can reduce cell viability [70].

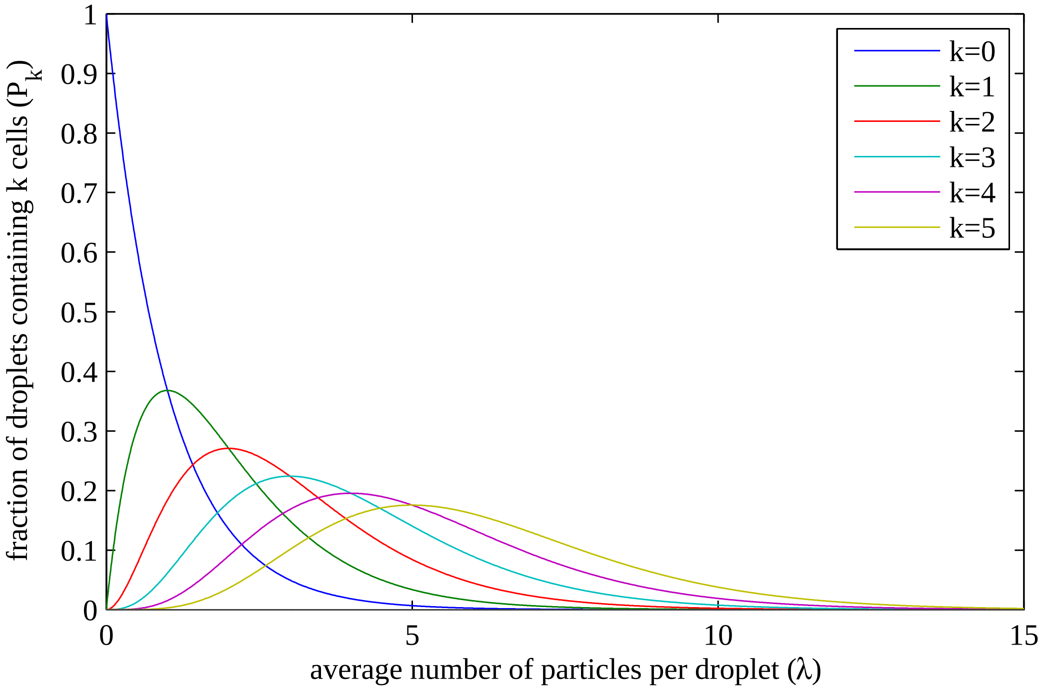

Figure 2.4 – The Poisson distribution for cell encapsulation: The probability of encapsulating k cells into droplets, as a function of the average number of particles per droplet (λ).

2.3.1 The statistics of encapsulation

When a cell suspension is passed through a droplet generator, the number of cells per droplet is governed by Poisson statistics, due to the random distribution of cells in the suspension [75]. The fraction of droplets containing k cells is described by equation 2.10, where P_k is the probability that a droplet contains k particles, and λ is the average number of particles per drop.

$$P_k = \frac{\lambda^k e^{-\lambda}}{k!} \tag{2.10}$$

λ can be related to the cell density as shown in equation 2.11, where Q_d is the flow-rate of the dispersed phase, f_d the droplet generation rate, and n_c the cell density in the dispersed phase. Here, the relation between the flow-rate Q_d and the generation frequency f_d is already dictated by the flow-focusing geometry, the material properties of the liquids used, and the flow-rate of the continuous phase Q_c. Thus, selecting a certain value of λ is achieved by changing the cell density (n_c), and requires some knowledge about the properties of the used device.

$$\lambda = \frac{Q_d n_c}{f_c} \tag{2.11}$$

In many applications, such as single cell analysis, loading a single particle per droplet is essential. From equation 2.10 the maximum percentage of droplets that contain a single particle is derived to be equal to 36.8% at $\lambda = 1$ (Figure 2.4). The downside of loading particles at an average of 1 particle per drop is that 36.8% of the droplets remain empty, and 26.4% contains two particles or more. Therefore, it is more common to select a lower value for λ, such as 0.3 used in a high-throughput hybridoma screening study [73], where less than 4% of the droplets contain two or more cells. This reduction in droplets with multiple particles comes at the expense of the encapsulation efficiency; only 22.2% of the droplets contain a single particle and 74% is empty.

Several researchers have investigated methods to overcome these statistics, using either a pre-encapsulating ordering mechanism, or post-encapsulation sorting. Ordering mechanisms can rely on hydrodynamic effects in specific channel geometries, such as Dean flow in curved channels [76], high aspect-ratio channel flow [71], and alternating contracting and expanding flow pinching [44]. The percentage of single cell containing droplets can be increased to 55-80% using these methods. Alternatively, optical tweezers can also been employed to encapsulate single cells in an actively controlled manner [74]. However, this method is not suitable for high-throughput droplet generation, as it relies on the manipulation of individual cells using optics.

Post-sorting methods typically rely on fluorescent labeling of the encapsulation target, optical detection, and active separation of the droplets that give a positive signal. This has for instance be achieved using commercially available Fluorescent Assisted Cell Sorting (FACS) equipment for large particles [70], or using a microfluidic device with optical detection [63]. A passive hydrodynamic method, based on spontaneous self-sorting behavior in boundary layers, has also been employed [72]. This passive method is very sensitive to cell size differences, enabling the selective encapsulation of T-lymphocytes from whole blood. The droplets generated in this approach, however, are not monodisperse, since they scale with cell size.

2.4 Temperature control in microfluidics

For encapsulation in Matrigel, which gelates as a function of temperature, control over the temperature of the encapsulation device is essential. Therefore, the most relevant techniques for microfluidic temperature control are briefly reviewed in this section.

Over the past few decades, many different temperature control strategies for microfluidic systems have been developed. One of the applications named before is found in DNA amplification on a chip through PCR, a process that requires thermo-cycling between 50°C and 95°C [77]. Apart from this application, microfluidic temperature control has also been applied to a number of other complex temperature sensitive processes, such as protein crystallization [78] and Temperature Gradient Focusing (TGF) [79].

The majority of studies into temperature control for microfluidic applications rely on external approaches, such as macroscopic Peltier elements or pre-heated liquids flowing through the microfluidic chip [80]. These methods enable the generation of homogeneous temperature regions, and even highly accurate local temperature gradients. Apart from these external approaches, a number of integrated methods have also been developed, for instance using micro-Peltier elements [81, 82], local Joule heating [83, 84], microwaves [85, 86], chemical reactions [87, 88], and integrated lasers [89, 90]. However, since our application does not necessarily require the generation of extremely accurate local gradients or temperature fields, the main focus is on the external approaches.

The most common external approach to control the temperature of a microfluidic chip is to place the chip in a temperature controlled environment, such as an incubation box or a temperature controlled room. A cold room has for instance been used to generate Matrigel beads inside a microfluidic chip [70]. Incubation boxes are generally used for any type of cell culturing experiment where live imaging is required, such as dengue inhibition experiments [91] or sperm motion measurements [92]. The disadvantages of these methods are that only homogeneous temperatures can be achieved and the equilibration time is typically long.

A method that does enable inhomogeneous temperature distributions is the attachment of active heating elements onto the chip. This method has for instance been applied to continuous-flow PCR on a chip [93], where two temperature zones 67°C and 95°C were realized using heating elements. Similarly, temperature controlled copper blocks have been used to create multiple temperature zones [36]. In this example, the temperature was regulated with active feedback on the heating elements, combined with passive cooling using cooling fins. The advantage of this approach is the simplicity of the heating process, for which all energy is obtained directly from an electrical source. However, cooling the chip is impossible with these elements.

In a more advanced approach that can also actively cool the chip, Peltier elements are employed to transfer heat. These rely on the Peltier effect, in which an electrical current carries heat from one side of the element to the other. These systems can typically achieve very high cooling rates compared to the previous method, since they are not limited by passive convective cooling. Peltier elements have for instance been used to generate a temperature gradient for TGF [79], and to thermocycle on a microfluidic PCR chip [94, 95]. Peltier-based thermocycling systems for microfluidics have also been used in commercially available PCR equipment [38]. The downside of this method is that transferred heat still has to be dissipated into the environment, which is typically achieved using large, actively cooled heat-sinks, which increases the size of the setup significantly. Moreover, Peltier elements can only control heat transport, such that local temperature measurement and active feedback is necessary in order to locally maintain a set temperature.

The final approach treated in this section is based on heat exchange between the chip and an externally heated or cooled liquid. By integrating a channel into the microfluidic chip, and pumping this liquid through, the local temperature can be controlled. This method has for instance been used in a high-resolution live cell imaging study, where the temperature could be switched between 5°C and 45°C in less than 10 seconds [96]. It was also applied to generate a linear temperature gradient over several microchannels [97], and in a highly advanced silicon chip for controlled production of semiconductor nanocrystals [98]. An advantage of this approach is that temperature regulation of liquids can be performed off-chip, reducing the volume of the chip itself. However, more fluidic interfaces have to be integrated into the chip.

In this chapter, the relevant physics at the microscale have been discussed, including viscous flow properties, interfacial effects, and diffusion. In the context of cell encapsulation, microfluidic methods for droplet generation were discussed in more detail, after which cell encapsulation methods from literature were briefly reviewed. Additionally, several temperature control methods for microfluidic applications were reviewed. Using this information, a device with integrated temperature control is designed for the encapsulation of cells in Matrigel beads in chapter 3.

Chapter 3

Device design

For the encapsulation of single cells in Matrigel beads, a microfluidic device is designed, which consists of two parts: A microfluidic side that contains the channel geometry for encapsulation, and a second part that facilitates local temperature control. First, the design of the microfluidic channel geometry for cell encapsulation is treated in section 3.1. Second, the temperature control method is selected and designed in section 3.2. Finally, the fabrication methods used to realize the complete design are discussed in section 3.3.

3.1 The microfluidic channel geometry

Initially, the aim is to generate beads with a diameter of approximately 100 µm, such that the inter-cellular spacing in culture is in approximately the same range. Connections between neurons should therefore have a similar length, which is between two and four times the size of a SH-SY5Y cell body [32], such that they will be clearly discernible. The droplet generation inherently enables the generation of beads with other diameters as well, such that the design is not limited to this diameter alone.

The microfluidic design has two parts: The flow-focusing section, in which cells are encapsulated in Matrigel microdroplets, and a section in which the droplets are gelated at an elevated temperature. The on-chip gelation of the beads is convenient for a number of reasons. First, droplets tend to coalesce when transitioning from a microfluidic channel to a macroscopic outlet tube. If the beads have already solidified at this stage, coalescence will not lead to the formation of larger diameter beads. Second, by inducing bead gelation in a microfluidic channel, more control over the local conditions is possible, which leads to a more homogeneously treated set of beads. Third, prolonged exposure of cells to low temperature could negatively influence their viability, as discussed in section 2.3. The time during which cells are exposed to low temperature is greatly reduced when the temperature is raised for on-chip gelation. Last, on-chip gelation introduces the possibility to integrate post-processing steps in the same microfluidic chip, such as bead sorting, oil removal, and possibly even the assembly of the final culture.

In order to design the chip, some knowledge on the fluids to be used is required. Especially the density and viscosity of the continuous phase are relevant to compute the relation between flow-rate and pressure. Therefore, these materials are selected first. For the continuous phase, a fluorinated oil is most desirable because of its biocompatible properties. However, due to the limited availability of synthesized fluorosurfactants, a hydrocarbon oil is selected: Mineral oil. This oil has been used successfully for droplet generation in the past, in combination with ABIL EM 90 surfactant. The materials are not necessarily biocompatible, such that a critical assessment of their impact on the encapsulated cells is needed. The material properties of mineral oil, shown in Table 3.1, are used for the chip design.

The dispersed phase is liquid Matrigel, which essentially is a protein mixture in water. The density of this mixture is not accurately known, due to the inter-batch variability in this product.

Table 3.1 – The properties of the mineral oil used (Sigma, M8410), relevant to the chip design.

density	0.84	g/mL
viscosity	$< 30 \cdot 10^{-3}$	Pa s

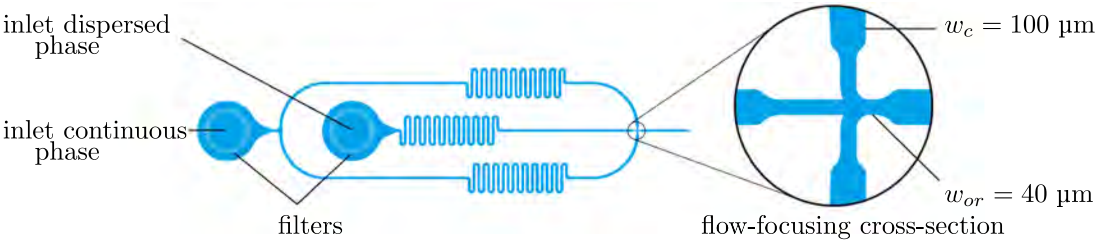

Figure 3.1 – A schematic illustration of the flow-focusing section, showing the inlets of the dispersed and continuous phase, small meandering channels for temperature equilibration, and the flow-focusing cross-section. Both inlets contain a filtering pillar array with a spacing of 20 µm. The widths of the orifice w_{or} and continuous phase channel w_c are also indicated. The dispersed phase channel has a width w_d equal to the continuous phase channel width.

However, an estimate of the density can be made, based on the typical protein concentration ranging from 8 to 12 mg/mL: $\rho_{MG} \approx 1.01$ g/mL. As discussed in section 2.2, the viscosity of the dispersed phase does not have a large influence on the droplet generation process.

The chip is made using standard photo-lithography and soft-lithography processes, as described in section 3.3, and designed to fit on a standard glass microscope slide (75x25 mm), such that it can easily be used on a microscope.

3.1.1 Flow-focusing section

As discussed in section 2.2, no analytical method exists to compute the droplet diameter and generation frequency inside a flow-focusing device. Therefore, the flow-focusing cross-section (Figure 3.1) is designed based on literature. The flow-focusing section should facilitate the encapsulation of cells inside spherical droplets with a diameter of approximately 100 µm, so the channel height (h) is set to 100 µm.

Data from a similarly dimensioned device from Ward et al. with $h = 75$ µm indicates that droplets with a diameter ranging from the orifice width w_{or} to $3 \times w_{or}$ can be manufactured using mineral oil [56]. In this work, an orifice width of 50 µm is used to generate droplet diameters between 50 and 150 µm, comparable to the diameter of 100 µm that is aimed for in this thesis.

In order to correct for the difference in channel height between the current design and the design from Ward et al., the modified flow-focusing capillary number in equation 2.9 is used to scale the orifice width. For an equal capillary number, the orifice should be slightly smaller than 50 µm. Based on the continuous and dispersed phase channel widths of 100 µm, the orifice width is set to 40 µm, compensating for the factor of 0.75 difference in the modified capillary number.

The inlets contain a 20 µm filter, which should prevent any large particles from entering the chip (Figure 3.1). The SH-SY5Y cells have a diameter of approximately 10 µm in suspension, so they should be able to pass the filter.

In addition to the flow-focusing cross-section and the inlets, three small meandering channels are included in the design. These are included to slightly delay the fluids on the chip, such that more time is available for temperature equilibration. However, this is not enough to cool the liquids completely, such that additional pre-cooling is necessary. The method for pre-cooling the liquids is discussed in section 3.2.3.

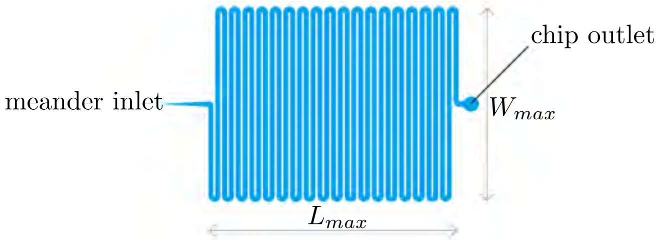

Figure 3.2 – A schematic illustration of the meandering channel section. On the left, generated droplets enter the meander inlet, and on the right droplets leave the meander through the chip outlet. The footprint dimension W_{max} is 20 mm, based on the size of a microscope slide. The footprint dimension L_{max} is 26 mm, based on the need for spacing between the hot and cold regions on the chip.

3.1.2 Gelation section

The main goal of this section is to keep the generated droplets at an elevated temperature for the time required for gelation. However, the exact time that is required for this process is unknown. In order to increase the chances of a full gelation on-chip, the residence time of droplets inside this section is maximized, for which a meandering channel design is selected. This also ensures that the residence time of each droplet is the same. Incorporating such a design in the chip influences the pressure drop over the system, which can lead to failure of the chip by delamination due to a high internal pressure. The maximum pressure drop that can be withstood by a plasma-bonded PDMS chip is approximately 0.5 MPa, as determined from previous experience, which should not be exceeded by design. The meandering channel section (Figure 3.2) has a maximum width (W_{max}) of 20 mm due to the limited size of a microscope slide. The maximum length (L_{max}) is set to 26 mm, to keep a sufficient amount of space between the cold and hot section on the chip.

As discussed in section 2.1.1, the pressure drop in the system is related to the flow-rate via the hydraulic resistance. Thus, in order to determine the pressure drop, the flow-rate in the system has to be known. However, the flow-focusing device does not enable direct computation of the flow-rates required to achieve a certain droplet generation rate and diameter (see section 2.2). A reasonable estimation of the maximum flow-rate can be made based on the desired droplet size, an estimate for the generation rate, and an estimate of the continuous phase flow-rate. The estimates are made based on the work of Ward et al., used previously to design the flow-focusing section. Assuming that the device generates droplets with a diameter of 100 µm, at a maximum rate of 500 Hz, the maximum dispersed phase flow-rate is approximately 15.7 µL/min. If we assume that this occurs when the flow-rate ratio ϕ defined in section 2.2 is 2, the total maximum flow-rate is approximately 50 µL/min.

Several channel dimensions are already fixed, such as the channel height (100 µm). Additionally, the spacing between the straight channels is set to 200 µm, in order to have sufficient surface area for glass-PDMS bonding. Combined with the constraints on the meander footprint, the remaining pressure tuning parameter is the channel width.

For each channel width, the maximum channel length that fits inside the maximum footprint area ($W_{max} \times L_{max}$) is selected, since this corresponds to the maximum achievable residence time for this width. Using this length, the hydraulic resistance is computed according to equation 2.5, which is used to compute the pressure drop. The minimum channel width for which the maximum pressure is not exceeded is then selected, corresponding to approximately 500 µm. The total meandering channel length is 766 mm. Using these dimensions, the droplet residence time (t_{res}) for each flow-rate can be estimated, based on the total meandering channel length and the average flow-velocity. For the chosen dimensions, this corresponds to a residence time of 46 seconds at the maximum total flow-rate of 50 µL/min. The entire channel geometry, including the flow focusing section, fits on a single microscope slide (Figure 3.3).

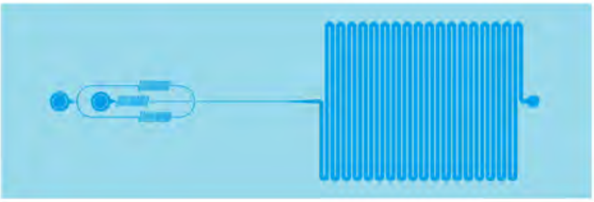

Figure 3.3 – A schematic illustration of the complete channel geometry, showing the position of the channels on the microscope slide.

3.2 Temperature control design

In order to encapsulate cells in Matrigel, the temperature of the encapsulation device has to be controlled. In this section, the temperature control method for the encapsulation chip is selected and designed. The selection and design are based on two main requirements that follow from the selection of Matrigel, and the fact that live cells are involved.

The first requirement is that in the droplet generation section, where the gel has to be in liquid form, the temperature has to be kept between 0°C and 4°C. If either one of these limits is surpassed, the Matrigel will solidify and impair the stable formation of droplets, either due to freezing below 0°C or gelation above 4°C.

The second requirement is that unnecessary thermal stresses on the cells should be avoided. Therefore, the temperature in the gelation section should not be much more than the physiological temperature of 37°C, but above 10°C [35].

3.2.1 Method selection

For our application, a temperature control method that can both cool down and heat the fluids inside the microfluidic channels is required, since the temperature range is partly below room temperature. Therefore, any method that uses Joule heating is not applicable, which leaves Peltier elements and liquid temperature control as the most viable options. The choice between these two alternatives is made based on two other, more practical requirements: The compatibility with microscopic observation, which is essential for droplet diameter tuning, and the complexity and size of the encapsulation setup.

For the first requirement, a transparent and compact solution is essential, since most microscopes rely on light transmission through the sample and do not offer much space. Although Peltier based chips have been adapted for transmission microscopy, by moving the sample towards a transparent region [94], they are generally non-transparent and difficult to fit under a microscope. Fluidic temperature control on the other hand, can be integrated in the same chip, without losing transparency or adding much material. Therefore, liquid based temperature control seems to be the most viable option.

This is also in agreement with the second requirement: To have a setup that requires the least complexity on the chip. Peltier elements require integrated temperature sensors and active feedback, which adds to the chips complexity. For liquid based control, the temperature is controlled externally, which renders temperature sensors or feedback obsolete, apart from an initial calibration of the system. Therefore, a simpler microfluidic chip can be used to obtain the same control over the local temperature.

3.2.2 Fluid based design

The key working principle of liquid based temperature control is heat transfer between a low volume stream of fluid (in microfluidic channels) and a high volume stream of another liquid at a set temperature. Due to the large difference in volume, the microfluidic side can equilibrate to the same temperature as the temperature controlled liquid, without significantly influencing the temperature of the other liquid. This enables the generation of a large region in which the temperature inside microfluidic channels can be regulated by a single high volume stream of liquid. In this design, water is chosen as the heating and cooling liquid.

A simple approximation of the required heat is made to illustrate the insignificant influence on the heating source. The heat capacity of water is approximately $4.2 \cdot 10^3$ J/kgK between 0 and 37°C [99]. The heat capacity of mineral oil is approximately $1.9 \cdot 10^3$ J/kgK [100]. Again assuming that flow-rate ratio ϕ is 2, the average heat capacity can be computed: $c_{p,av} = 2.66 \cdot 10^3$ J/kgK. By combining this with the maximum occurring temperature difference of 37°C and the maximum flow-rate of 50 µL/min in the microfluidic channels, the required heat transfer rate can be estimated: $Q_{required} \approx 0.072$ J/s. A temperature drop of only 0.005°C in the heating water can be realized at a flow-rate of just 150 mL/min.

Although heating the contents of the microfluidic channels has no impact on the temperature of the heating water, it could locally influence the temperature distribution. In order to assess this influence, the thermal entrance length is estimated. It takes some time for the liquids in the microfluidic channels to heat up. The timescale at which this happens is estimated by neglecting convective heat-transfer and approaching the system as purely conductive one-dimensional system. In that case, the characteristic length-scale over which heat has to diffuse is equal to the channel height (100 µm). The thermal diffusivity in the microfluidic channels is estimated using $\alpha = k/\rho c_p$, where k is the average thermal conductivity, ρ the average density, and c_p the average heat-capacity. The thermal conductivity of water is approximately 0.6 W/mK [99] and the thermal conductivity of mineral oil is $0.12 - 0.15$ W/mK [101]. The timescale of heat diffusion is estimated using $\tau = L_c^2/\alpha$, where L_c is the characteristic length scale. This results in an estimated timescale of 20.7 ms, during which the liquids travel 0.35 mm on average, which is short compared to the length of the meandering channel (766 mm). This indicates that the microchannel flow also has negligible impact on the temperature distribution within the chip. Thus, we can safely conclude that this strategy is feasible.

The channels transporting the water should comply to the following requirements: First, in order to achieve a high flow-rate, without large pressure losses, channels with a large cross-sectional area are preferred. Second, the thermal resistance between the water and the contents of the microchannels should be low to facilitate fast heat transfer.

The larger channels could have been integrated into the PDMS material in which the microfluidic channels reside. However, the high flow-rates for heating and cooling require large channel dimensions in order to minimize pressure losses. Integration of larger channels would complicate both the chip design and the required fabrication methods. Additionally, PDMS has a low thermal conductivity (0.18 W/mK [102]), such that very thin walls would be required in order to achieve a sufficiently low thermal resistance. Therefore, it is decided to attach temperature control chambers directly to the glass bottom of the chip. By doing so, the only material separating the two liquids is a glass microscope slide, which has a higher thermal conductivity ($1 - 1.4$ W/mK) relative to PDMS [99, 102]. Moreover, the chambers can cover a large section of the microscope slide, without interfering with the microfluidic channel geometry.

The 20×30 mm footprint of the high temperature chamber overlaps with the meandering channel section in the microfluidic design (Figure 3.4), in order to maintain a constant temperature for each passing droplet. Part of the meandering channel does not overlap the hot chamber, such that the temperature increase is gradual. The low temperature chamber (20×25 mm) covers the area in which the droplets are generated. In order to minimize heat transfer between the high and cold liquid, there is 15 mm of solid material between the two chambers. The total height of the added layers is kept below 4 mm, with 3 mm chamber height and 1 mm bottom thickness, to enable focusing on the microchannels with the inverted microscope used.

3.2.3 Auxiliary equipment and connections

In order to feed the two thermal chambers with water at a set temperature, two thermal reservoirs are required. For the high temperature reservoir, a 500 mL glass beaker on a hot-plate with active temperature control is used (Yellowline, yellow MAG HS 7). For the low temperature reservoir,

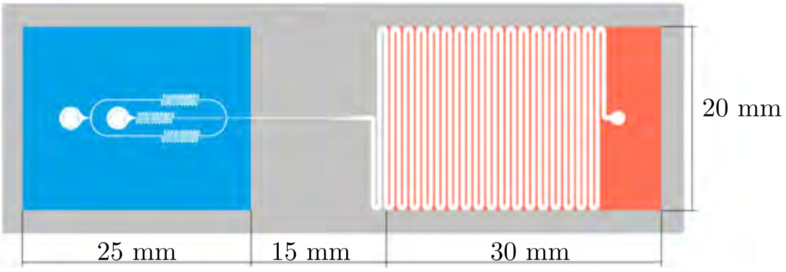

Figure 3.4 – A schematic overlay of the microfluidic design on the thermal chambers, showing the positioning of the channel geometry relative to the cold (blue) and hot (red) thermal chambers.

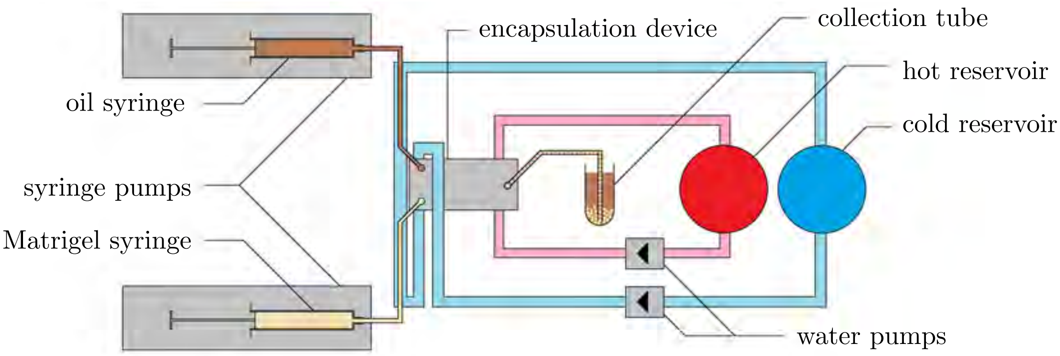

Figure 3.5 – A schematic overview of the encapsulation setup, including syringes, pumps, tubing connections, and the hot and cold reservoirs. The different components are not to scale.

a 500 mL glass beaker filled with ice water is used. By regularly adding ice to this reservoir, a temperature very close to 0°C can be maintained for the duration of an experiment. It is important to note that using ice water does not facilitate temperature tuning at the cold side of the chip. The temperature at this side is essential for keeping the Matrigel in liquid state, such that droplets can be generated.

Both reservoirs are fitted with magnetic stirrers in order to achieve a homogeneous temperature throughout the reservoirs. Water is pumped through each chamber using two micro-pumps (RS, 480-188) connected to the chip and reservoirs via silicone tubing (Tygon, E3603). This tubing is connected to the 2 mm holes using a trimmed pipette tip (VWR, 613-0578) and some epoxy (Bison, Kombi Snel).

The tubing used for cold water is also used to pre-cool the oil and Matrigel before entering the microfluidic chip (Figure 3.5). For both microchannel inlets, 20 cm of microfluidic tubing (SCI, BB31695-PE/5) is fed through holes in a larger diameter silicone tube (Tygon, E3603), such that the cool water flows around the chip inlet tubing. This tube is connected directly to the outlet of the cold chamber, providing a constant source of cold water. The 20 cm long microfluidic tube also creates a cool reservoir in which the Matrigel can be injected before starting the droplet generation process. In order to prevent too much heating of the cooling water, the tubing between the cold reservoir and the chip is insulated using clean-room tissue (Texwipe, TX609) and electrical tape.

3.3 Fabrication methods

The device was made of multiple layers (Figure 3.6), using standard photo- and soft-lithography processes, combined with laser-cutting and gluing for the temperature control chambers.

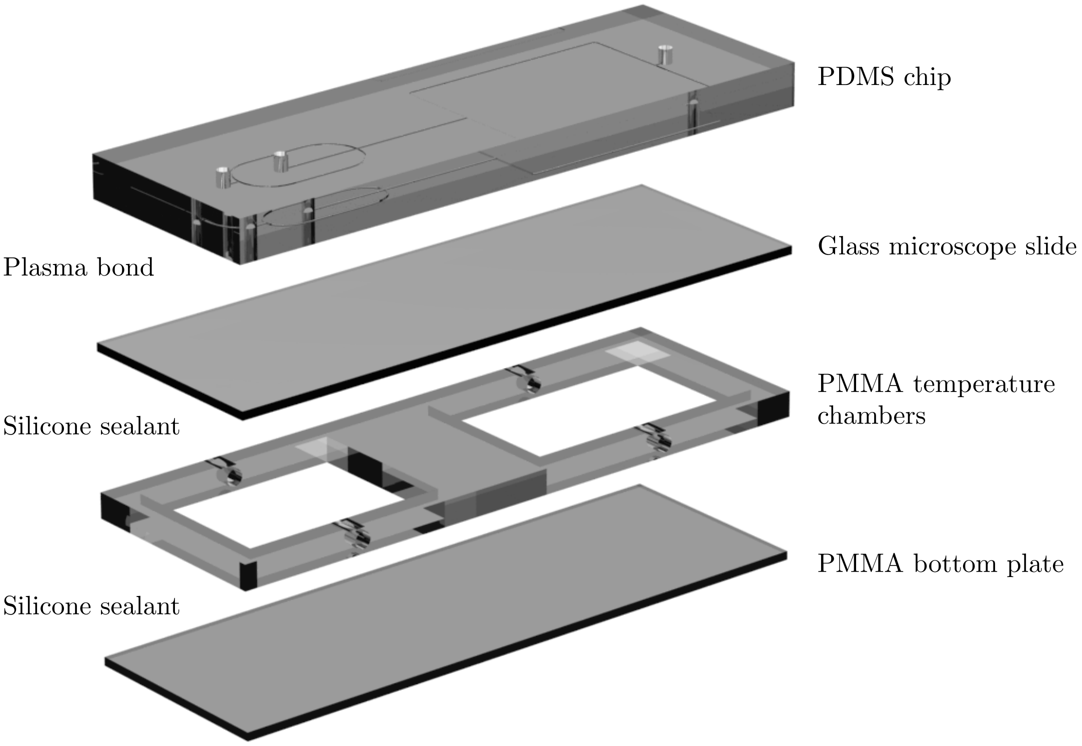

Figure 3.6 – A schematic representation of the four layers that form the complete encapsulation chip, indicating the bonding types between the layers.

3.3.1 Microfluidic chip fabrication

First, a master-mold was made using photolithography, after which it was replicated in PDMS. This replica was then bonded to a microscope slide to finalize the microfluidic side of the device.

Photo-lithography

A wafer was cleaned by subsequently rinsing it with acetone, isopropanol (IPA), and ethanol, after which the wafer was dried with nitrogen gas. To further reduce the amount of liquid left on the wafer, it was put on a 95°C hot plate for about 2 minutes. A 100 µm layer of photoresist (Microchem, SU-8 3050) was coated onto the cleaned wafer using a spin-coater (Laurell, WS-400B-6NPP-LITE).

The coated wafer was then baked on a 95°C hot plate for 50 minutes, after which the photomask containing the channel design was placed on top of the wafer. The mask was covered by a clean glass plate and exposed to UV-light for 18 seconds, at 14 mW/cm^2. After exposure, the wafer was placed on a hot plate at 65°C for 1 minute, followed by a 5 minute bake on a 95°C hot plate to initiate cross-linking.

The wafer was then developed in a bath filled with developer (Micro Resist Technology, mr-dev 600) under constant agitation by an orbital shaker (Cole-Parmer, EW-51300-05). After 10 minutes, the developer was refreshed, and the wafer was developed for another 5 minutes. Finally, the finished master was rinsed with IPA and dried with a nitrogen jet.

Soft-lithography

PDMS base and curing agent (Sylgard, 184) were mixed at a 10:1 ratio using a planetary centrifugal mixer (Thinky, ARE-250) at 2000 rpm for 1.5 minutes, followed by a degassing step at 2000 rpm for

1 minute. The mixed PDMS was poured onto the master, and put under vacuum for approximately 1 hour, to remove any air bubbles from the cast. The filled mold was then put in an oven at 65°C for at least 3 hours to cure the PDMS.

After curing, the PDMS was removed from the master and cut to separate the different devices. Inlet and outlet holes were punched using a 1.2 mm biopsy punch. The PDMS slabs were then bonded to a glass slide using a plasma surface activation method. Dust was removed from the PDMS slabs and microscope slides using some standard tape, after which both were exposed to an air plasma for 45 seconds (50 W, 0.6 mbar) in a plasma asher (Emitech, K1050X). The plasma treated slides and PDMS slabs were then carefully connected and put in an oven at 65°C for 1 hour to finalize the bonding process.

3.3.2 Temperature chamber fabrication

The walls of the temperature control chambers were made of Poly(methyl methacrylate) (PMMA), which has a thermal conductivity that is similar to that of PDMS. The bottom of the device was laser-cut into the shape of a microscope slide (25 × 75 mm) from 1 mm thick extruded PMMA plate. The layer forming the sidewalls of the temperature chambers was laser-cut from 3 mm thick extruded PMMA plate. In and outlets with a diameter of 2 mm were carefully drilled into the sides of the cut chamber sections. The two parts were then glued together using a slow curing silicone sealant (Dow Corning, Multi-purpose Sealant 732), which was applied using a 5 mL plastic syringe. After leaving the sealant to cure for at least 24 hours, the microfluidic side of the device was bonded to the assembled bottom section using the same sealant.

In this chapter, a device with integrated temperature control for the encapsulation of cells in Matrigel was developed. First, a microfluidic chip was designed, consisting of a flow-focusing section for Matrigel droplet generation, and a meandering channel section where droplets are gelated to form beads. Temperature control chambers were added to this chip, to achieve a temperature below 4°C at the flow-focusing section, such that liquid Matrigel droplets can be generated, and a temperature above 10°C at the meandering channel section to induce gelation. Finally, the fabrication methods used to manufacture the complete device were described. The temperature control chambers are validated in chapter 4, after which the device is tested for the generation of Matrigel beads in chapter 5, and for cell encapsulation in chapter 6.

Chapter 4

Validation of microfluidic temperature control method

In this chapter, the temperature control design for the microfluidic encapsulation chip is evaluated using both simulations and experiments. The main goal is to show that it works at a level that is sufficient for Matrigel droplet formation, bead gelation, and cell encapsulation whilst retaining cell viability. First, both the temperature distribution and flow field properties are investigated using a COMSOL simulation model in section 4.1. Next, the outcome of the simulations are compared to measurements and the temperature control chambers are calibrated in section 4.2. Finally, the results are discussed in section 4.3.

4.1 Simulations of temperature control strategy

In order to evaluate the temperature control method, simulations were performed using a 3D model of the complete chip designed in chapter 3. The model included the PMMA temperature chambers, the glass microscope slide, and the PDMS layer that normally contains the microchannels. The channels were omitted from the simulation, since their influence on the temperature distribution is negligible as argued in section 3.2. The water flow in the heating and cooling chambers was also taken into account. The simulation setup is described in more detail in appendix A.

The simulations were performed for water temperatures of 0°C at the cold side of the chip, and 50°C at the hot side of the chip. The temperature of 50°C was chosen instead of 37°C since heat-losses are bigger at higher temperatures, such that a worst-case scenario could be investigated. Moreover, some hydrogels such as agarose require a similar temperature to either gelate, or remain liquid. Thus, including this temperature in the analysis ensures that the method is also feasible for alternative gels. The steady-state temperature distribution throughout the entire chip was simulated for several different flow-rates for water, ranging from 0.6 mL/min to 120 mL/min. This range was chosen since the maximum specified flow-rate of the pumps used is 350 mL/min, and coupling to the chip reduces the flow-rate, estimated to be close to 120 mL/min. First, the complete temperature profile was assessed for the minimum and maximum simulated flow-rate (Figure 4.1).

The simulations show that homogeneous temperature zones form at the high flow-rate of 120 mL/min, while a very inhomogeneous temperature distribution forms at 0.6 mL/min. Clearly, there is a certain minimum flow-rate at which the temperature distribution becomes approximately homogeneous. One of the reasons for this difference is that at low flow-rates, heat transport through the device significantly changes the temperature of the water in both chambers. At a flow-rate of 120 mL/min, water inside the chambers is refreshed faster than heat losses can significantly impact temperature.

Another reason for the different temperature distribution is the different velocity field at these flow-rates (Figure 4.2). At 120 mL/min, two vortices can clearly be seen. These vortices distribute

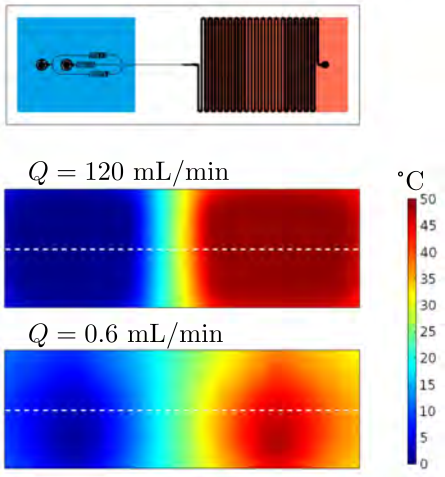

Figure 4.1 – Simulation of the temperature distribution on the microfluidic side of the glass slide, for water flow-rates of 0.6 and 120 mL/min. A schematic of the position on the channels and both chambers is shown above. The dotted line indicates over which line the temperature profile is shown in Figure 4.3

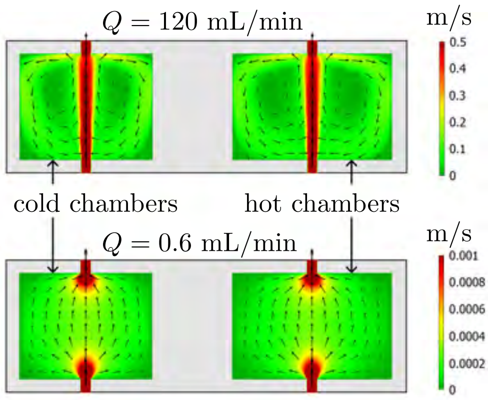

Figure 4.2 – Simulation of the velocity field inside the temperature chambers, in the center cross-section of the chambers, for water flow-rates of 0.6 and 120 mL/min. The scaling in both images is adjusted such that the flow properties are clearly visible. The maximum velocity for 120 mL/min is 1.31 m/s, and the maximum velocity for 0.6 mL/min is 0.0066 m/s. The arrows are scaled logarithmically with respect to the fluid velocity.

the water throughout the entire chamber, ensuring the spread of heat. At the low flow-rate of 0.6 mL/min, shear forces are too low to induce vortex formation, resulting in a poor distribution of heat.

The transition between the two states can be assessed by evaluating the temperature profiles for all simulated flow-rates, along the center of the chip (Figure 4.3). For the simulated flow-rates of 0.6 and 6 mL/min, it is clear that the temperature curve has absolutely no constant regions. However, for flow-rates of 30 mL/min and up, the graph shows two regions with nearly uniform temperature. Moreover, towards the higher flow-rates, the temperature profile seems to converge to a fixed solution, although it never fully reaches the set temperatures at the chip inlets (0 and 50°C). It is important to note that the temperature on top of the glass slide will never be equal to these temperatures, since the heat resistance of the slide prevents this from happening.

Another conclusion we can draw from these simulations is that the regions of constant temperature are slightly smaller than the temperature chambers. For the cold region this is acceptable, since the inlet and flow-focusing section are centered on the cold region, at sufficient distance from the edges. For the hot region, however, this means that the temperature is not constant over the entire meandering channel section. Especially near the bends in this section, temperature can be several degrees lower than in the center. Fortunately, this is negligible, since the exact temperature is not relevant for Matrigel gelation, as long as it is higher than 10°C [35]. Between the two temperature sections, there is an approximately linear transition between the low and high temperature, with a gradient that converges to approximately 2.9°C/mm.

Using these simulations, the feasibility of the temperature control strategy has been shown. At sufficiently high water flow-rates, vortices form inside the temperature chambers that distribute the heat or cold over the designated area. However, the simulations have only taken the chip itself into account, assuming perfect heat transfer between the materials that comprise the chip. In order to fully validate the approach, including possible heat losses in the auxiliary equipment and tube connections, temperature measurements are required. Additionally, calibration of the reservoir temperatures is essential for setting the correct temperature.

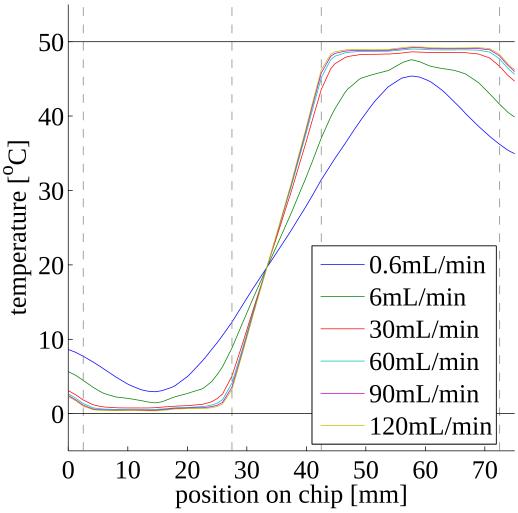

Figure 4.3 – Simulated temperature profile for flow rates between 0.6 and 120 mL/min. The gray dashed lines indicate the edges of the temperature chambers, and the solid black lines the set temperature at the inlets of these chambers: 0 and 50°C.

4.2 Experimental validation and characterization of temperature control strategy

Experiments were carried out with the purpose of both validating the temperature control approach, and calibrating the setup. First, the flow-rate through both chambers was measured, in order to confirm that the pumps produced a sufficiently high flow-rate for vortex formation. Second, the temperature profile (Figure 4.3) was measured in order to estimate the deviation from the performed simulations. Third, the independence of the temperature of the cold region from the temperature of the hot region was tested. Fourth, the temperature of the hot region was calibrated with respect to the reservoir temperature. Last, the calibration curve was validated at the settings as used in all encapsulation experiments.

4.2.1 Materials and methods

Flow-rate measurement

The flow-rate generated by the two water pumps is different from the flow-rate of 350 mL/min indicated in the specifications, due to the additional hydraulic resistance introduced by the attached tubing and temperature chambers. In order to measure the actual flow-rates generated by the hot and cold water pumps (RS, 480-188) at full power, two separate measurements were performed. One 1 L glass beaker was filled completely and put on a height-adjustable platform. Another 500 mL beaker was filled with 100 mL of water and placed on another height-adjustable platform. The platforms were adjusted in such a way that the water levels in both beakers were at equal height, as not to create any pressure differences. By avoiding pressure difference, the circulation of water from the temperature reservoirs is mimicked more accurately. For connecting the pumps, chip, and beakers, the same silicon tubing as in all other experiments was used (Tygon, E3603).

First, the inlet of the pump for the hot side was connected to the 1 L beaker using 35 cm of tube, the outlet of the pump was connected to the inlet of the chamber using 40 cm of tube, and the outlet of the chamber was connected to the 500 mL beaker using 65 cm of tube. Before submerging and fixing the tube ends with tape, the entire chain was filled with water from the 1 L beaker by aspiration with a 50 mL syringe (Terumo).

The tested pump was connected to a power source (Voltcraft, PS-2403D) at 4 V, starting the flow. The beaker that was being filled was continuously lowered using the adjustable platform, such that the water levels in both beakers remained at equal height. When 100 mL of water was pumped into the receiving beaker, the time was started in order to eliminate any start-up effects. The time was noted when the next 100 mL had been transferred. The flow-rate was then computed by dividing the transferred volume (100 mL) by the elapsed time. This measurement was repeated 8 times.

Next, the inlet of the pump for the cold side was connected to the 1 L beaker using 25 cm of tube that was insulated by wrapping it in cleanroom tissue (Texwipe, TX609) and electrical tape to minimize condensation. The outlet of the pump was connected to the inlet of the chamber using 40 cm of tube, insulated using the same materials. The outlet of the chamber was connected to the 500 mL beaker using 110 cm of tube, in which the microfluidic tubing as described in section 3.2.3 was already installed. The measurement procedure as described for the hot side was then repeated for the cold side.

Temperature measurement of simulated profile

All temperature measurements were performed on chips without the PDMS microchannels attached, using the same type of pumps and tubing as in the previous section (4.2.1). In order to measure the surface temperature on the glass slide, a measurement tool with 5 parallel temperature sensors (Amphenol Advanced Sensors, DC95F502W) was used. The design of this tool can be found in appendix B. The sensors were attached to the glass side of the chip with some thermal paste (Jürgen Armack GmbH, Thermal compound T12) and electrical tape, and all sensors were covered by insulating padding in order to mimic the insulation that is normally provided by the PDMS. A USB cable was used to connect the measurement tool to a PC.

For the hot thermal reservoir, a 500 mL glass beaker filled with deionized and filtered water was placed on a hot-plate with magnetic stirrer (Yellowline, yellow MAG HS 7) that was set to 50°C. A PT1000 temperature sensor was connected to the hot-plate, which yields a controller accuracy of ±0.5°C. For the cold thermal reservoir, a 500 mL glass beaker was filled with 300 mL deionized and filtered water, and put on a stirring plate (Thermo Scientific, 50094711). Ice was added until the water level reached the 500 mL mark, and constantly replenished during the measurements.

Since only 5 parallel sensors were available, three different measurements were used to cover the entire device. For the first measurement of the cold region of the chip, sensors were placed at 8, 13, 18, 25, and 31 mm from the edge of the device (Figure 4.4). For the second measurement of the gradient between both chambers, sensors were placed at 27, 31, 35, 39, and 43 mm. For the last measurement of the hot region, sensors were placed at 45, 49, 55, 61, and 68 mm. All measurements were taken along the centerline of the device.

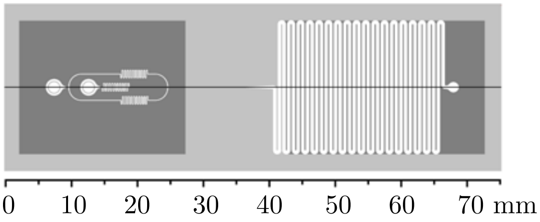

Figure 4.4 – A schematic image of the temperature control chambers, on which the channel geometry is superimposed. The centerline along which all temperature measurements were taken is indicated using a black line. The ruler shows the dimension along which the measurement positions are defined.

Both pumps were connected to the power source at 4 V in parallel, starting the flow, and the setup was left to equilibrate for 5 minutes. Next, the Matlab temperature logging software was started and data was collected for approximately 7 minutes for each of the three sensor placements. The temperature was logged every 10 seconds during that time.

Temperature measurements of cold region at different hot reservoir temperatures

Several measurements were performed to determine the influence of the temperature in the hot reservoir on the temperature of the cold region. The measurement procedure was the same as in the previous paragraphs, apart from the temperature of the hot reservoir, the position of the sensors, and the sampling frequency. The temperature was measured at 5, 10, 15, 20, and 26 mm from the side of the device, corresponding to the cold region on the chip (Figure 4.4). Each measurement was done for 5 minutes, during which the temperature was logged every 0.5 seconds. Measurements were performed for hot reservoir temperatures of 30, 32, 33.5, 34, 36, 39, 43, and 47 ±0.5°C.

Temperature measurements for calibration

Several measurements were performed to calibrate the temperature of the glass surface with respect to the temperature of the hot reservoir. This experiment was carried out the same way as the previous experiment, except for the temperatures of the hot reservoir and the measurement positions. The temperature was measured at 44, 49, 55, 61, and 68 mm from the side of the device, corresponding to the hot region on the chip (Figure 4.4). Measurements were performed for hot reservoir temperatures of approximately 39, 44, 46, 50, and 55 ±0.5°C.

Temperature measurement at encapsulation settings

For this experiment, The hot reservoir was set to 39°C, based on the calibration curve obtained from the previous experiment. The temperature was measured at 5 relevant positions, corresponding to the approximate position of the inlet of the dispersed phase, the flow-focusing section, and the start center and end of the meandering channel, at 16, 24, 42, 55, and 70 mm (Figure 4.4).

4.2.2 Results

Flow-rate measurements

Both the flow-rate through the cold and through the hot temperature chamber was measured. The flow-rate through the hot temperature chamber (Q_h) was 150 mL/min, with a standard deviation of 14. The flow-rate through the cold temperature chamber (Q_c) was 150 mL/min, with a standard deviation of 11. This confirms that in both chambers, the flow-rate was sufficiently high to induce the vortex formation that is necessary for an even temperature distribution, according to the simulations discussed in section 4.1.

Temperature measurement of simulated profile

Temperature measurements were performed on the temperature control chambers, for comparison with the simulated temperature profile (Figure 4.3). The temperature profile for reservoir temperatures of 0 and 50°C was in good agreement with the simulated profile in terms of the profile shape (Figure 4.5). Both regions of constant temperature and the linear temperature gradient are present in the data.

However, there are several deviations from the simulated profile, such as the higher temperature at the cold chamber (approximately 2.5°C higher), and the slightly lower temperature at the hot chamber (approximately 1°C lower). These differences between theory and practice can be attributed to both limits of the simulation and physical error sources. The simulation, for instance, does not take heat losses in the pumps and tubing into account: The temperature at the inlet of the chip is assumed to be equal to the reservoir temperature reservoirs. Moreover, heat-losses to the environment have been modeled as natural convection, neglecting any forced convective air-flows around the chip.

An important observation during the measurements was that, especially on the cold side of the chip, air bubbles could get trapped inside the chamber. These bubbles were formed mainly inside the pumps, which was determined by visually tracking bubbles through the transparent tubing.

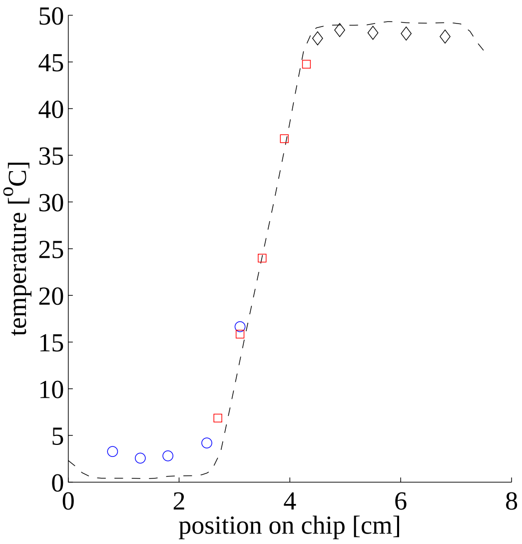

Figure 4.5 – The measured temperature profile on the chip for reservoir temperatures of 0 and 50°C. The profile was determined from 3 separate measurements: On the cold chamber (○), between the chambers (□), and on the hot chamber (◇). The temperature curve obtained from the simulation is shown as a dashed line.

They coalesced inside the vortices, and remained there until the chip was rotated in such a way that gravity pushed the bubbles towards the outlet. The fact that more bubbles got trapped inside the cold chamber, could be attributed to the temperature and pressure changes of the cooling water inside the pump, which changes the solubility of gases in water. Regular interventions were necessary to remove the air bubbles that impair the visibility under a microscope, but could also reduce heat transfer towards the microchannels.

The fact that the difference was larger on the cold side could be attributed to additional heat that is being generated inside the pump. Additionally, the cold reservoir was not exactly 0°C, but slightly warmer. However, this does not fully explain the difference, since the actual temperature of the cold reservoir was determined to be 0.3 ± 0.1°C. Therefore, the most likely cause is the water heating by the pump, and heat-transfer in the tubing before the chip.

Despite the deviations between the simulation and the measured profile, the temperature of the cold region is below 4°C, which is sufficient for having liquid Matrigel inside the device.

Stability of the cold region and temperature calibration

In order to investigate the stability of the cold region with respect to the hot region, measurements were done on the cold side for hot reservoir temperatures of 30, 32, 33.5, 34, 36, 39, 43, and 47°C (Figure 4.6). The average temperature of the cold region varied slightly around a mean temperature of 3.4°C, but there was no correlation between the temperature of the reservoir and the cold region. This indicates that the hot region can be calibrated for different temperatures, without having an impact on the cold chamber.

In order to calibrate the temperature of the hot region with respect to the temperature of the hot reservoir, the temperature of the hot side of the chip was measured for reservoir temperatures of 39, 44, 46, 50, and 55°C (Figure 4.7) At all reservoir temperatures, the measured temperature of the hot region was lower than the reservoir temperature by approximately 1°C, showing that there were heat-losses between the reservoir and the chip.

However, the temperature on the chip correlated linearly with the temperature of the reservoir on the measured range, such that a linear fit on the measured temperatures could be used for calibration. Using the calibration curve shown in equation 4.1, where T_{hc} is the temperature of

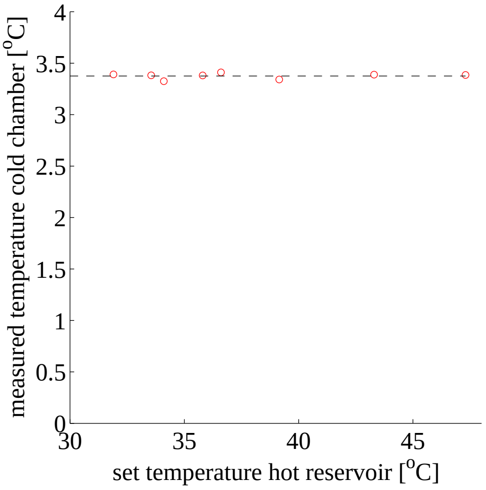

Figure 4.6 – The average temperature of the cold region of the chip as a function of the temperature of the hot thermal reservoir. The red circles show the measurements, and the dashed line is the average of these measurements (3.4°C).

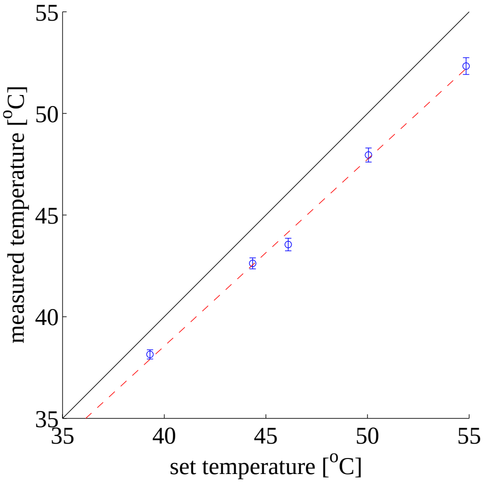

Figure 4.7 – The average temperature of the hot region on the chip as a function of the thermal reservoir temperature. Blue circles show the measurements, and the dashed red line a linear fit to these measurements. Error bars represent the standard deviation. The solid black line shows the theoretical, lossless case where the hot region temperature equals the reservoir temperature

the hot region on the chip, and T_{hr} the temperature of the hot reservoir, the temperature of the reservoir could be set to achieve a desired temperature on the chip.

$$T_{hr} = 1.08 \cdot T_{hc} - 1.73; \tag{4.1}$$

The temperature profile at calibrated temperatures

Using the calibration curve derived from the previous experiment, a measurement was performed on the system set to the temperatures to be used for all future experiments, with a hot region temperature of approximately 37°C. However, the hot reservoir could only be set to integer temperature values, such that a choice had to be made between 36.8 and 37.7°C as hot region temperature, considering equation 4.1. It was decided to aim for a temperature of 37.6°C, for which the hot reservoir was set to 39°C.

The temperature was assessed on five locations on the chip that were essential relative to the microchannels: Right after the Matrigel inlet, at the flow-focusing cross-section, and at the start, center, and end of the meandering channel (Figure 4.8). The measurements show that the temperature is 3.4°C at the inlet and the flow-focusing section, such that Matrigel will be liquid at these positions. Moreover, at the meandering channel, the temperature rises to approximately 37.4°C, which is close enough to the target temperature of 37.7°C: It is within tolerance of the temperature sensor array (±0.2°C) and the hot temperature reservoir (±0.5°C).

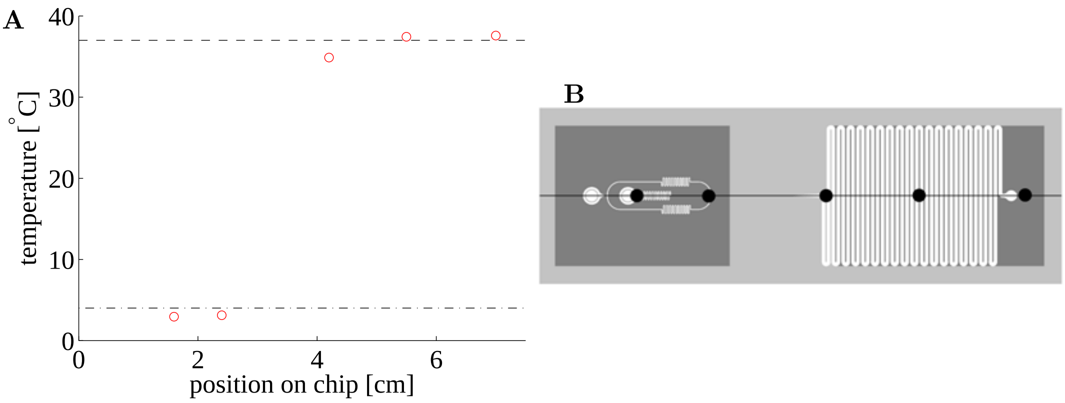

Figure 4.8 – The temperature measurements at cell encapsulation settings (A), at the approximate positions of the inlet of the dispersed phase, the flow-focusing section, and the start center and end of the meandering channel (B). The dashed line indicates the target temperature of the hot region of 37°C, and the dash-dotted line indicates the maximum allowable cold region temperature of 4°C. The temperature of the hot reservoir was set to 39°C.

4.3 Discussion

As discussed in section 3.2.3, the cold region on the chip is the most essential, since adjustment of the cold reservoir temperature is impossible and the temperature below 4°C is an absolute requirement to keep the Matrigel in a liquid state. The measurements have shown that an average temperature of 3.4°C can be achieved for hot reservoir temperatures between 39 and 47°C. This seems quite close to the 4°C limit imposed by the gelation of Matrigel. However, this relatively high temperature could also be caused by the measurement method itself. The temperature sensors were connected to the surface using thermal paste and tape, and covered with some isolation to represent the normally present PDMS. The measurement itself is thus not purely a measurement of the exact surface temperature, but will always deviate a bit towards room temperature.

Therefore, it is likely that the actual temperature of the cold region was lower, and the temperature of the hot region slightly higher. Especially the probably lower cold region temperature does not cause issues with Matrigel gelation. Thus, despite not knowing the exact surface temperature, the possible measurement error is not detrimental to the functioning of the chip. Most importantly, the cold region temperature is reproducible.

An important challenge is the prevention of bubble collection inside the thermal chambers as described in section 4.2.2, to increase visibility and prevent heat transfer issues. The most straightforward solution to this issue is to place the source of most bubbles, the pump, downstream of the chambers. However, the pumps used are not usable for negative pressures, so another pump is required for this solution. Alternatively, the thermal chambers could be redesigned as not to capture bubbles as easily. This could include removal of sharp corners, and measures to prevent vortex formation, without reducing the heat-transfer.

In this chapter, the temperature control chambers were validated using simulations and experiments. The temperature control chambers were shown to function as intended: A homogeneous temperature region below 4°C could be generated at the flow-focusing side of the chip, such that Matrigel droplets can be made. A homogeneous temperature region at approximately 37.4°C could be generated at the meandering channel section, such that the droplets can be gelated to form beads. Using the validated temperature control chambers, the generation of Matrigel beads is evaluated in chapter 5, after which the encapsulation of SH-SY5Y cells is tested in chapter 6.

Chapter 5

Bead generation

Using the microfluidic chip as designed in chapter 3 and the temperature settings obtained in chapter 4, Matrigel bead generation experiments were carried out. In this chapter, the main goal is to show that monodisperse Matrigel beads can be produced using the encapsulation chip. In order to do so, the generation of Matrigel droplets inside the designed chip is investigated first in section 5.2.1, focusing on the stability of the process. In order to improve the stability and dispersity, a surface coating is then introduced and adapted for the microfluidic chip in section 5.2.2. Next, the ability to reproducibly create monodisperse beads with this coating is shown using measurements in section 5.2.3, after which the relation between the motion of individual droplets in the meandering channel and observed coalescence events is investigated in section 5.2.4. The generated beads are then transferred to cell culture medium, and their radius and dispersity is assessed with respect to the measurements on droplets inside the device in section 5.2.5. Finally, the results are discussed in section 5.3.

5.1 Materials and methods

5.1.1 Matrigel bead generation

At the start of the experiment, Matrigel (VWR, 734-0269) was put on ice to thaw at low temperature to prevent the premature gelation of the material. Next, the temperature control section of the setup was filled with water and turned on at the encapsulation settings described in section 4.2.1.

First, the chip outlet tube was inserted into an Eppendorf tube. For the continuous phase, mineral oil (Sigma, M8410) containing 4 wt.% of a polysiloxane surfactant (Evonik Industries, ABIL EM 90) was aspirated into a 1mL plastic syringe (Terumo). The syringe was installed on a syringe pump (Chemyx, Nexus 3000), and connected to the continuous phase inlet using a 20 GA needle tip (Techcon Systems, TE720050PK). Most of the inlet tube was filled with the continuous phase, by briefly running the pump at 50 µL/min. For driving the dispersed phase (Matrigel), a 1mL plastic syringe (Terumo) was filled with mineral oil (Sigma, M8410). A 20 GA needle tip (Techcon Systems, TE720050PK) was attached to the syringe, which was installed on a syringe pump (Chemyx, Nexus 3000). The setup was now ready for injection of the Matrigel.

Using a pipette, 100 µL Matrigel was injected in the inlet of the dispersed phase, and the prepared syringe was inserted in the tube to push the Matrigel into the cooled tube section. In order to push all of the Matrigel in the cooled section, the pump was briefly switched on at 20 µL/min.

The chip was first filled with oil: The syringe pump of the continuous phase was turned on at 20 µL/min and left to fill the entire chip with oil and surfactant. After approximately 5 minutes, when oil started to flow from the outlet tube, the flow-rate was reduced to 10 µL/min. The pump for the dispersed phase was set to 5 µL/min, until the Matrigel had moved to a distance of about 5mm from the inlet of the chip. The flow-rate of the continuous phase was now set to 2 µL/min, and the flow-rate of the dispersed phase to 1 µL/min. Setting these final flow-rates before the gel entered the chip ensured that the equilibration time of the droplet generating process was minimized.

After the gel had reached the flow-focusing section, the collection of data from the bead generation process begun. Microscopic movies were made with a camera (The Imaging Source, DFK 31AU03) that was attached to an inverted microscope (WPI, INV-101). Movies were captured for 30 seconds approximately every 5 minutes, at a frame-rate of 15 Hz. These movies were made of both the flow-focusing section and a section of the meandering channel.

When all of the Matrigel had passed the flow-focusing section after approximately 1.5 hour, the pump for the dispersed phase was turned off. The pump for the continuous phase was set to 20 µL/min to remove all remaining beads from the chip. This also pushed any possible leftover Matrigel back into the dispersed phase inlet, which prevented any more droplet formation. After all beads had been moved into the collection tube, it was closed and the beads were retrieved from the oil according to the retrieval process described in 5.1.2.

5.1.2 Bead retrieval

After generation, Matrigel beads were suspended in the continuous phase comprised of mineral oil and surfactant. For bead stacking and cell culture experiments, however, the beads should be transferred to cell culture medium. In order to achieve this, several washing steps in mineral oil without surfactant and cell culture medium were performed. The oil washes were performed to reduce the surfactant concentration, which was necessary for beads to break through the oil-medium interface. The medium washes were performed to reduce the amount of oil in the sample.

First, an Eppendorf tube containing the collected beads in oil was centrifuged at 800 rpm for 1 minute, using a mini-centrifuge (Eppendorf, Minispin). This forced the beads to form a pellet at the bottom of the tube. The oil supernatant was removed from the tube by aspiration, and 300 µL of fresh mineral oil was added. By aspirating with and ejecting the mixture from a pipette, the beads were resuspended. The tube was then centrifuged again at 800 rpm for 1 minute. The oil addition, resuspension, and centrifugation steps were repeated twice, after which the remaining oil supernatant was removed from the tube by aspiration.

Next, the beads were washed several times with medium (Figure 5.1). First, 300 µL of cell culture medium was added to the Eppendorf tube. The beads were then resuspended by aspirating and ejecting the mixture several times using a pipette. At this point, most of the beads already transferred from the oil to the medium. A 2 minute centrifugation step at 1000 rpm was performed in order to force most of the beads from the remaining oil into the medium. The higher centrifugation speed was chosen to overcome the decreased density difference between the beads and the surrounding liquid. The medium addition, resuspension, and centrifugation steps were repeated twice.

The oil supernatant and most of the medium was removed from the tube by aspiration, and moved to another clean tube. Next, 300 µL of fresh cell culture medium was added to the first tube. The beads were again resuspended by aspirating and ejecting the mixture, and centrifuged at 1000 rpm for 1 minute. The result was three tubes filled with medium, from the three culture medium addition steps. These tubes are referred to as wash 1, 2, and 3 respectively in the rest of this thesis.

5.1.3 Surface coating experiment

A hydrophobic coating was applied to the microfluidic channels to ensure that the continuous phase was wall wetting on all channel sides. In order to test the effectiveness of a coating of octadecyltrichlorosilane (OTS) on both glass and PDMS, a contact angle experiment was carried out. Three microscope slides and three slabs of cured PDMS were subjected to different treatments, and the resulting contact angles of water and oil droplets were qualitatively assessed.

The first treatment was based on a glass chip coating procedure used by Roberts et al. [103], leading to OTS grafting on glass. First, the PDMS slab and a ±2 cm^2 section of the glass slide

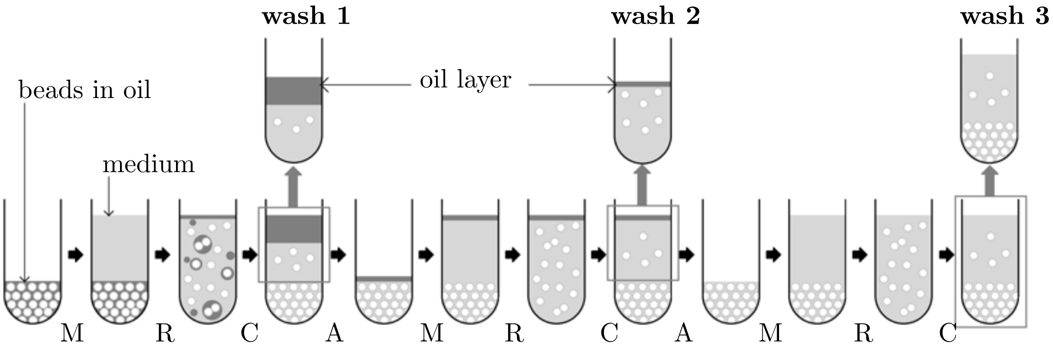

Figure 5.1 – Schematic representation of the bead washing process in medium, resulting in three sample tubes marked wash 1, 2, and 3. The medium addition steps are marked M, the resuspension steps with R, the aspiration steps with A, and the centrifugation steps with C.

were rinsed with 100 µL of anhydrous hexadecane (Sigma, 296317), after which 100 µL of a 2 vol.% solution of OTS (Sigma, 104817) in anhydrous hexadecane was pipetted onto the samples. The solution was left to react at room temperature for 5 minutes, and subsequently rinsed with 100 µL of hexadecane. The samples were thoroughly rinsed, first with isopropanol, then with ethanol, and dried with a nitrogen jet.

The second treatment included a plasma ashing step before adding the 2 vol.% solution of OTS in anhydrous hexadecane, in which the samples were subjected to a 50 W air plasma for 45 seconds using a plasma asher (Emitech, K1050X). The goal of this additional step was to also activate the PDMS surface for chemical bonding of OTS, by hydroxylizing the surface, leading to OTS grafting on both the glass and PDMS.

The third treatment was the control, where no OTS was added to the solution, but all rinsing steps were exactly the same as for the previous two treatments.

After all samples had been treated, 10 µL droplets of both de-ionized water and oil were pipetted onto the samples, and the resulting contact angle was recorded using a USB microscope (iTEZ, eScope DP-M01).

5.1.4 Surface coating of droplet device

The protocol for OTS-coating from the previous section was adapted for use in the encapsulation chip, where all liquids were injected using a 1mL plastic syringe (Terumo) with a 20 GA needle tip (Techcon Systems, TE720050PK). The chip was first flushed with approximately 200 µL of anhydrous hexadecane. It was carefully injected into the inlet for the continuous phase, until droplets formed at both the dispersed phase inlet and the outlet. Excess liquid was removed from the chip surface using a clean-room tissue (Texwipe, TX609). Approximately 200 µL of a 2 vol.% solution of OTS in anhydrous hexadecane was injected into the chip using another syringe, and left to react for 5 minutes. Next, the chip was flushed with 200 µL hexadecane, 400 µL isopropanol, and 400 µL ethanol. The device was partially dried by injection of nitrogen gas and left to dry completely overnight.

5.2 Results

5.2.1 Droplet generation in uncoated devices

Droplets were first generated in four devices without any surface modification. From recorded videos of moving droplets inside the meandering channel, droplet radii were determined over the course of the experiment (Figure 5.2). For more details on the image processing method used, see appendix C.

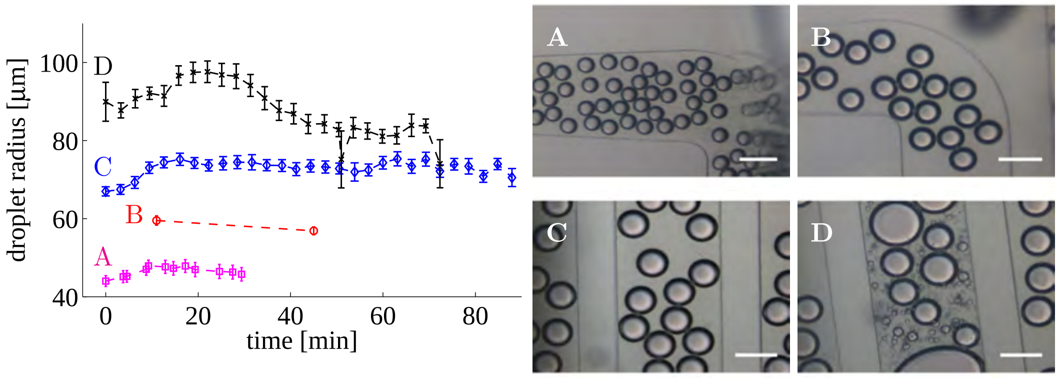

Figure 5.2 – Droplet generation data from four generation experiments using uncoated devices. All experiments were performed with the same flow-rates for the dispersed (1 µL/min) and continuous phase (2 µL/min). The error bars in the graph represent the standard deviation. Images A-C show a frame of the movies from which droplet radii for the corresponding curves were determined. Image D shows the droplet stream during one of the unstable phases at around 50 and 70 minutes in the corresponding data. Scale bars indicate 200 µm.

In experiment A, flow-rates were varied after 30 minutes. Therefore, only the short phase at the same flow-rates as used in the other experiments is shown. In experiment B, only two measurements were done. All experiments were performed in different devices, except for experiments C and D, for which the latter was performed in the same chip after experiment C.

In three of the four droplet experiments (A, B, and C), stable droplet generation was observed. This is most apparent in the radius data from experiment C, where the measured radius converged towards a constant average during the first 15 minutes. A similar convergence towards a steady state was observed in the data from experiment A. The same was observed during experiment B, although there is not enough data to show this.

In experiment D, radius drifting and unstable phases were observed: The average radius did not converge towards a steady state and at around 50 and 70 minutes high coalescence and dispersity were observed (Figure 5.2 D). This unwanted variation can be attributed to the fact that the device had been used before: Leftover Matrigel could have solidified on the sidewalls and interfered with the generation process.

Most importantly, however, there were huge differences between the average radii of the generated droplets in different devices: The droplet generation process was not reproducible across devices. As previously mentioned in section 2.2, the interactions between the liquids and the solid wall can greatly affect the droplet generation process. Since the glass side of the channel wall is hydrophilic, the dispersed phase is wall wetting on one side of the chip. This is suspected to be the cause for the high variability of the droplet radius.

Evidence for this theory is found in the droplet generation movies at the flow-focusing section, from which stills of two different generation modes could be identified (Figure 5.3). The first generation mode in the flow-focusing section, a dripping jet of approximately 400 µm had formed, through which droplets with a radius of a little over 50 µm were generated. Part of the dripping tail did not have a clear interface with the surrounding oil, which indicates a low contact angle between the gel and the glass bottom (Figure 5.3 A). In an extreme case, the dripping tail had progressed through the channel downstream of the flow-focusing section (Figure 5.3 B). In this mode, droplets with a very large diameter were generated. Moreover, since the dripping tail progressed through the downstream channel, the gel was subjected to a higher temperature, which caused it to solidify on the glass bottom. This effect rendered the progression of the tail irreversible.

It is clear that for reproducible droplet generation, a solution for the hydrophilic nature of the glass side of the device is necessary. Therefore, a coating of the glass surface is tested in the next section.

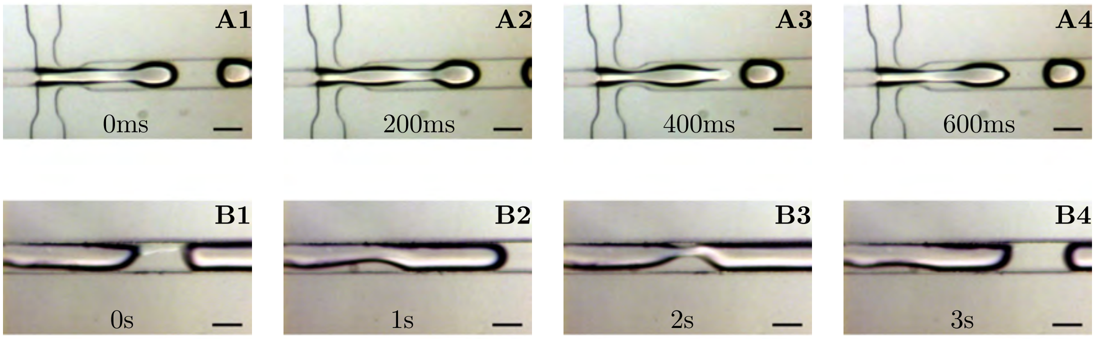

Figure 5.3 – Two droplet generation modes inside an uncoated device. In the first mode, a dripping jet of approximately 400 μm breaks into droplets downstream of the flow-focusing section (A). In the second mode, this jet has progressed several millimeters downstream and has become more irregular and asymmetric (B). This mode is associated with generation of very large droplets. It is important to note that these stills do not show a single droplet formation event, but rather an apparent slower droplet release. This is caused by temporal aliasing due to the limited camera frame-rate (15 Hz). The actual generation rate ranges from 15 to 30 Hz for these flow-rates. All scale bars indicate 100 μm

5.2.2 Hydrophobic coating

Several different treatments are available to render a glass surface hydrophobic, of which most are based on the grafting of a silane with a hydrophobic tail onto the surface. The most effective silanes that contain fluorinated carbon tails can render glass surfaces superhydrophobic. However, it is also important that the surfaces remain lipophilic, such that the mineral oil used is still wall wetting. Since octadecyltrichlorosilane (OTS) contains a long carbohydrate tail, it has lipophilic properties, and is selected for the chip coating.

In order to assess the influence of this coating on both glass and PDMS, a contact angle experiment was carried out using three different treatments. Treatment A is a control treatment, where no OTS is coated onto the materials, but all rinsing steps are performed as described in the methods section. Treatment B does contain a OTS coating step, and treatment C also adds a plasma treatment step that should lead to OTS grafting on the PDMS surface as well. Both a droplet of deionized water and mineral oil was pipetted onto each of the samples, and a picture was taken of the resulting contact angle between the droplet and the surface (Figure 5.4).

On the control sample (A), the hydrophilic nature of glass is clearly visible in image A3, where the water droplet shows a very small contact angle. The hydrophobic property of PDMS is visible in image A4, and the lipophilic properties of both glass and PDMS are visible in A1 and A2.

The contact angles of water on both glass and PDMS are more than 90° for both treatment B and C, which shows that both treatments make glass hydrophobic (see B3 and C3), while maintaining the natural hydrophobic state of PDMS (see B4 and C4). Both treatments also maintain the lipophilic properties of both glass and PDMS (see B1, B2, C1, and C2), although it seems to be slightly less so than in the control sample. Theoretically, treatment C should have grafted a layer of OTS on the PDMS surface as well, but this does not seem to enhance or deteriorate the hydrophobicity.

It can be concluded that both treatment B and C work, since the glass is hydrophobic after both treatments. Moreover, both methods produce a sufficiently stable coating, which was confirmed by an additional contact angle measurement 24 hours after coating (data not shown). In order to keep the coating protocol as simple as possible, treatment B is selected for adaptation to microfluidic chip coating.

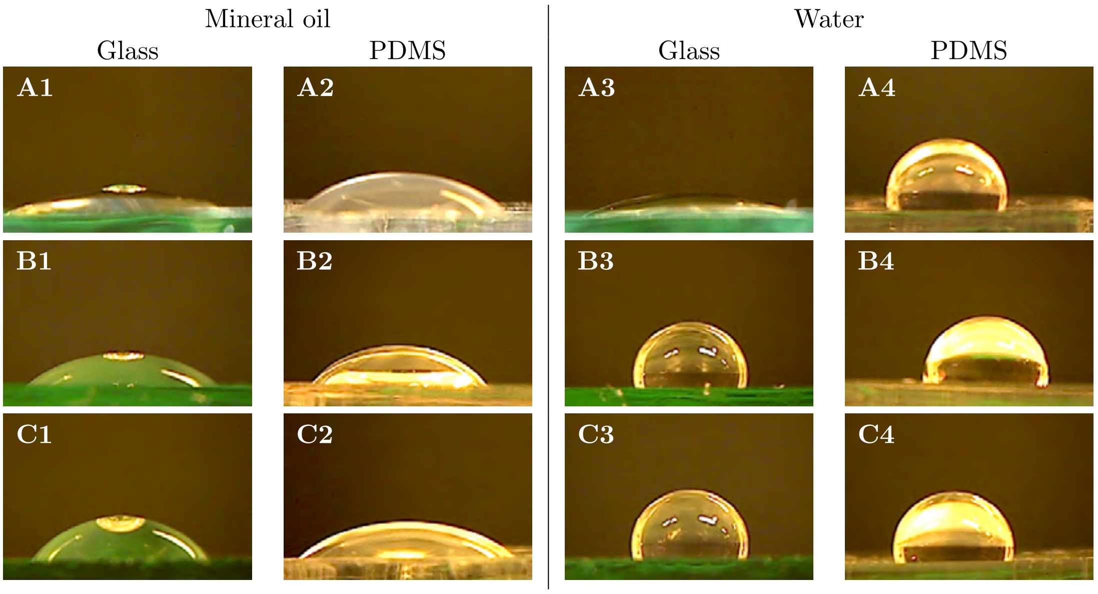

Figure 5.4 – Contact angle images of OTS treated and untreated PDMS and glass for treatments A, B, and C. For treatment A, the control treatment, only washing steps were performed (A). For treatment B, the materials were subjected to a 2 vol.% solution of OTS for 5 minutes (B). For treatment C, the materials were first treated with an air plasma and then subjected to a 2 vol.% solution of OTS for 5 minutes (C).

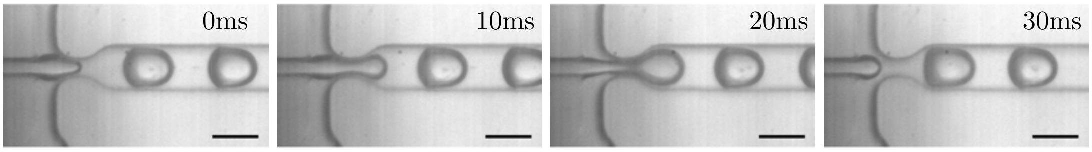

Figure 5.5 – High speed camera images of stable generation in an OTS coated device, taken during a cell encapsulation experiment. All scale bars indicate 100 μm

5.2.3 Reproducible droplet generation

After coating the encapsulation chip with OTS as described in the methods section, four more experiments were carried out in order to test the effectiveness of the hydrophobic coating. During these experiments, cells were also encapsulated, which is discussed in detail in chapter 6. High-speed camera images show that the hydrophobic coating functions as intended (Figure 5.5): Droplets are actually generated inside the flow-focusing section, without the formation of a progressing tail.

Again, droplet radii were determined over the course of the experiment from recorded videos of moving droplets inside the meandering channel. Additionally, the droplet generation frequency was derived by dividing the number of counted droplets by the duration of each movie (Figure 5.6). For a detailed description of the image processing method used, see appendix C.

When comparing the average radii of the four different experiments, major improvement in the reproducibility is observed: All devices generate droplets of almost exactly the same diameter. Moreover, all experiments are in a stable generation regime, since the droplet radii hardly vary over the duration of the experiment. The dispersity of the droplets, computed by dividing the standard deviation by the average radius, varies between 2 and 3% for all experiments. This shows that the droplets are highly monodisperse.

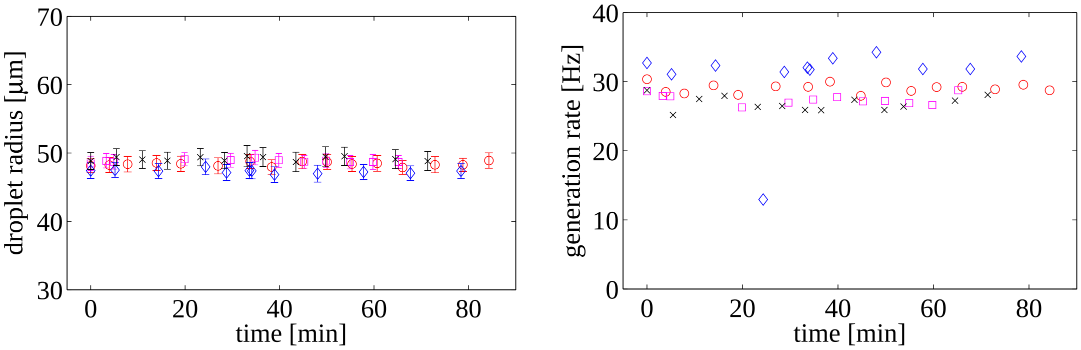

Figure 5.6 – Graphs of the average diameter and the droplet generation rate for 4 independent experiments, marked □, ◇, ○, and ×. Error bars indicate the standard deviation, which is approximately 1 µm for all radius measurements. The low ◇ generation rate value of 13 Hz is the result of a coalescence event, which is omitted from the average. The average droplet radii for □, ◇, ○, and × are 48.4 µm, 48.8 µm, 47.3 µm, and 49.1 µm respectively. The average generation rates and standard deviations for □, ◇, ○, and × are 29.1 ± 0.7 Hz, 27.5 ± 0.8 Hz, 32.5 ± 1 Hz, and 26.9 ± 1.1 Hz respectively.

The generation rate, much like the average radius, varies slightly between experiments. A lower droplet radius corresponds to a higher generation rate (Figure 5.6). This is in agreement with the fact that all experiments were conducted with the same flow-rates. It is important to note that one of the frequency measurements deviates significantly from the others. This is the result of a coalescence event upstream of the measurement position, which causes temporary blockage of the meandering channel, and therefore temporary depletion of droplets in the measurement section. Since in this section, the droplet generation rate and dispersity are investigated, this measurement is excluded from all the computed averages. However, the coalescence event does influence the dispersity of the beads that are retrieved from the device, which is discussed in more detail in the next sections.

In conclusion, the coated encapsulation device enables the stable, reproducible generation of monodisperse droplets with a dispersity $< 3\%$. The overall average droplet generation rate is 29 Hz, which means that for the duration of an entire experiment (± 90 minutes), approximately $1.57 \cdot 10^5$ droplets are generated, with an average radius of 48.4 µm. Since the aim was to produce beads with a diameter of 100 µm, and an average diameter of 96.8 µm is achieved, this design is usable for further experiments.

5.2.4 Droplet velocity, residence time, and coalescence

As revealed in the previous section, some coalescence events occurred inside the meandering channel section, which resulted in droplet depletion downstream of this event. In this section, the relation between the movement of droplets through the meandering channel and these coalescence events is investigated.

Large coalesced droplets that block the channel and cause the formation of a densely packed droplet train were observed (Figure 5.7). This is caused by a discrepancy between the velocity of a large and regularly sized droplet: When droplets stabilized with a surfactant coalesce to form a larger droplet, their velocity with respect to the average fluid velocity typically decreases [104]. In order to quantify the difference, the velocity of a large, channel blocking droplet (Figure 5.7B) is compared to the velocity of unconstrained droplets (Figure 5.8).

Droplets normally move with a velocity between 500 and 1000 µm/s. In the center of the channel, droplets have a velocity that is equal to or less than the average fluid velocity of 1000 µm/s. Droplets near the sidewall have a lower velocity, due to the lower local fluid velocity in this area. However, the velocity of a channel blocking droplet is approximately 630 µm/s. The velocity difference between free droplets and a large coalesced droplet causes the formation of the densely

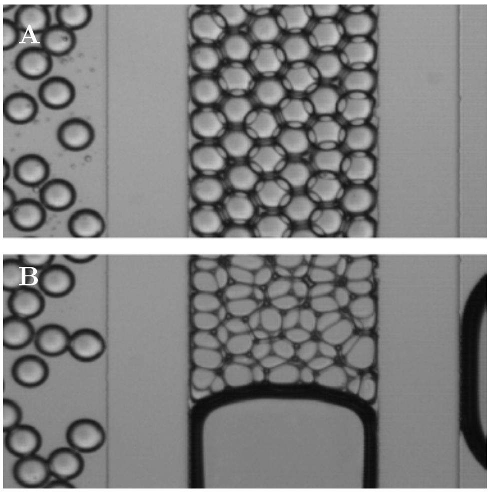

Figure 5.7 – A large droplet that blocks the entire meandering channel, followed by a densely packed train of droplets (B). Droplets in this region are prone to coalesce, despite the surfactant, increasing the large droplets size. More upstream, the droplets are less densely packed (A).

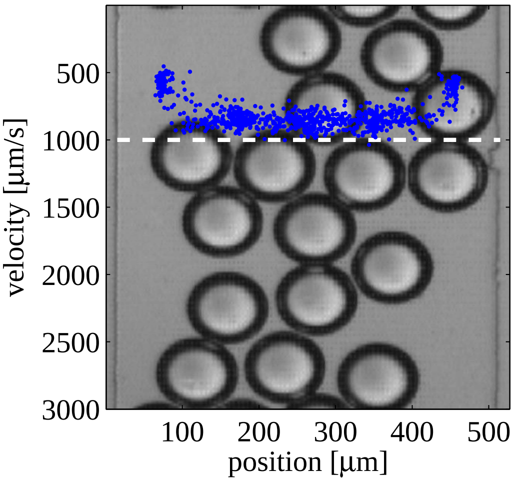

Figure 5.8 – The velocities of individual droplets inside the meandering channel as a function of their position in the channel, marked with blue dots. The dotted line shows the mean fluid velocity in this channel, computed based on the flowrate and channel dimensions. For this graph, the velocity of 833 droplets was measured.

packed particle train. Since droplets become very closely packed (Figure 5.7 B), coalescence is more likely to occur. This can increase the size of the leading droplet during its residence in the meandering channel. Typically, this leads to a number of relatively large beads in the outlet of the encapsulation chip.

Another important conclusion is that the residence time within the device can be very different for particles near the wall and in the center. Especially since droplets typically do not move from the wall to the center due to the laminar flow inside the device. For example, a droplet at the lowest measured velocity (454 µm/s) takes approximately 14.5 minutes to travel through the entire meandering channel section, while a droplet at the highest velocity (1037 µm/s) takes just 6.3 minutes. For the generation of Matrigel beads, this is not detrimental as long as the beads are solidified within the minimum residence time.

5.2.5 Bead retrieval

Beads were retrieved from the continuous phase, and transferred to cell culture medium using several washing steps, as described in section 5.1.2. In this section, the washing protocol is evaluated with respect to the yield and the radius and dispersity of the obtained beads.

In the oil washing steps, some beads always remain in the continuous phase, which is the result of the manual handling required for washing. This is undesirable, as it decreases the number of beads available, but completely avoiding this from happening is very difficult. Fortunately, only few beads are lost in this process.

The medium washes are more problematic in terms of bead losses. Due to the low density difference between the beads and the surrounding liquid, centrifugation does not lead to pellet formation as rapidly as in oil. Moreover, the beads are no longer contained within and oil-water interface, such that they can interact with the walls of the tube and the pipette tips used for handling. Part of the beads generally sticks to these surfaces, leading to significant bead losses. This was observed as a visible layer of beads on the pipette tips used, indicating that a high number of beads is lost in the retrieval process. In order to still retain enough beads for cell culturing, all medium washing steps were used for these experiments.

The radius of the washed beads is quantified by manual measurement of microscopic images, since automated processing was impossible due to a lack of contrast between the beads and medium. It is important to note that for this measurement, a bead generation run with a very low level of coalescence was used, such that the effect of droplet coalescence is not incorporated in this analysis. Based on the measurement of 87 beads obtained from the final wash of one of the bead generation experiments (Figure 5.6), the average *bead* radius is equal to 46.06 µm, with a standard deviation of 2 µm. This is slightly lower than the average *droplet* radius of 47.3 µm, with a standard deviation of 1.2 µm. However, the difference is insignificant with respect to the standard deviation.

The bead dispersity is 4.4%, which is higher than the 2.4% for droplets. However, the commonly used definition of a monodisperse distribution is that the dispersity should be less than 5%, such that the beads can still be considered monodisperse [65]. The increase in dispersity when the beads are retrieved can be attributed to a number of factors, such as the fact that the washing steps could compress and deform the beads, or that beads from the still equilibrating starting phase also end up in the bead mixture. Another possible cause for the difference is the significantly smaller sample size for the measurement of the *bead* radius: Only 87 beads were measured, as opposed to 11026 droplets.

5.3 Discussion

In this chapter, the stable and reproducible generation of Matrigel droplets with diameter of approximately 100 µm has been shown. These droplets solidify inside the device, and can be retrieved for culture experiments in medium. However, some challenges for optimal bead generations remain and some general platform improvements are possible. These are discussed in this section.

For future experiments, it is desirable to have full control over the diameter, in order to vary the inter-cellular spacing between encapsulated cells. Here, only a reproducible diameter of 100 µm is shown, but smaller radii are also possible in the current device, as indicated by the radius scaling discussed in section 2.2. For producing larger droplet diameters, the height of the device should be adjusted, as not to create non-spherical beads.

One challenge is the reduction of coalescence in the meandering channel, which introduces polydispersity in the final bead suspension. Although coalescence is difficult to prevent completely, some changes to the design of the meandering channel could significantly reduce the impact on other droplets. Since the main issue is a discrepancy between the velocity of larger coalesced droplets and regular droplets, reducing the width of the channel could help. This should remove the difference in velocity completely when regular droplets are also fully constrained by the channel walls, although care has to be taken as not to generate non-spherical beads. Alternatively, the flow-rate of the continuous phase can be increased, such that the spacing in between droplets increases.

The most important challenge is increasing the yield of the bead retrieval method. Especially in the cell culture medium washing steps, significant numbers of beads were lost due to their tendency to stick to solid surfaces. Unfortunately, no quantitative measurements of the yield were possible, but the visible layer of beads on used pipette tips indicates that a high number of beads were lost in the retrieval process. Moreover, centrifugation of the bead suspension did not result in the same level of separation as in oil. In order to improve the yield, the tubes and pipette tips used could be coated with a material that prevents Matrigel adhesion, such as poly(ethylene glycol). Additionally, an emulsion destabilizing agent could be introduced into the oil before centrifugation, to facilitate droplet breaking [59]. However, integration of the oil washing and medium transferring steps into the chip itself holds greater promise of a more controlled retrieval method. For instance, a channel geometry could be incorporated that forced the beads through co-flowing streams of clean oil (washing), and culture medium (transferring), using a micro-post array as used by Iwai et al. [105] (Figure 5.9). Due to the slow diffusion at this scale, as discussed in section 2.1.2, mixing of the co-flowing streams could be prevented by applying a high enough flow-rate. Alternatively, a hydrodynamic oil replacement method similar to the method used by

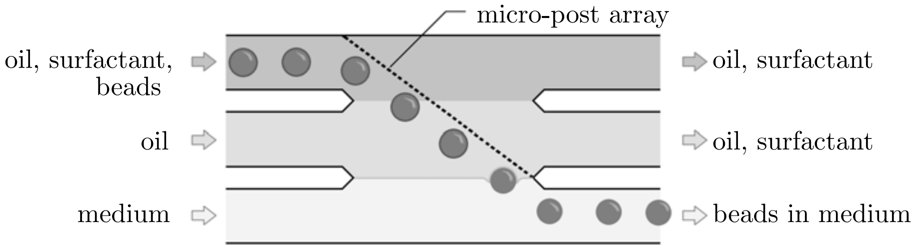

Figure 5.9 – A schematic image of the retrieval concept used by Iwai et al. to recover nanoparticles from micro-droplets [105]. Beads are forced through a co-flowing stream of clean oil by a micro-post array, to reduce the surfactant concentration at the interface. This enables bead release into another co-flowing stream of medium.

Kim et al. [60] could also be employed to wash the beads on-chip.

A possible improvement for this platform is faster generation of beads: Currently, the beads are fabricated at relatively low rates (±29 Hz), which could be increased to several kHz. If the flow-rates are tuned well, beads of the same diameter could be generated. This would decrease the time that cells are exposed to non-physiological conditions, and enable the fabrication of far more beads within the same time span. However, care has to be taken as not to over-pressurize the system, or subject the cells to too high stresses.

Another possible improvement of the platform is re-usability of the chip: The encapsulation chip has not been successfully used for more than one bead generation experiment. The main reason for this is that Matrigel can bond to the walls when temperature rises in between experiments, interfering with the velocity field and wetting properties of the fluids in the next experiment. For future work, re-usability of the devices is desirable, as the fabrication of one chip is quite labor intensive. For achieving a re-usable platform, either a good device cleaning method, or another coating that prevents Matrigel adhesion should suffice.

In this chapter, the generation of Matrigel beads was tested in the device designed in chapter 3. First, the device was shown to generate Matrigel beads in an unstable manner. In order to overcome this, an OTS surface coating method was tested to make the chip completely hydrophobic. This resulted in stable and reproducible generation of Matrigel droplets with diameter of approximately 94.6 µm, which is close to the 100 µm diameter as intended in the design. These droplets were gelated on-chip, and the formed beads could be recovered from the continuous phase and transferred to cell culture medium. Next, the encapsulation of SH-SY5Y cells in Matrigel beads is tested in chapter 6.

Chapter 6

Cell encapsulation

The generation of Matrigel beads has been achieved in chapter 5, such that the encapsulation of SH-SY5Y cells can be tested in this chapter, using the same microfluidic chip. First, the cell density is chosen based on theory on the statistics of encapsulation from section 2.3.1 in section 6.1. Next, the efficiency of the encapsulation is assessed in section 6.3. Finally, the experimental results are discussed in section 6.4.

6.1 Selecting the cell density

As discussed previously in section 2.3.1, the distribution of cells in our device follows a Poisson distribution, which is dependent on the average number of cells per droplet (λ). This parameter can be tuned as a function of the cell density n_c, as described by equation 2.11 in section 2.3.1.

As common in literature on cell encapsulation, the aim is to maximize the number of droplets containing a single cell, while ensuring that the number of droplets with more than one cell is less than 4%. In our chip, the droplet generation rate at an inner flow-rate (q_d) of 1 µL/min and an outer flow-rate (q_c) of 2 µL/min is approximately 29 Hz. This leads to the selection of a cell density of $5 \cdot 10^5$ cells/mL, corresponding to an average number of cells per droplet λ of 0.29. From the Poisson distribution, we can derive that 21.8% of the droplets should contain a single cell, and only 3.5% more than one cell (Figure 2.4).

6.2 Materials and methods

6.2.1 Cell culture

SH-SY5Y cells (Sigma Aldrich, 94030304) were cultured in T75 culture flasks, under 10 mL of DMEM-F12 medium (Biowest, L0093) supplemented with 10% Fetal Bovine Serum (FBS) (Bovogen, SFBS, lot 11113) and 1% Penicillin-Streptomycin (P/S) (Westburg, LO DE17-602E). This mixture is referred to as *culture medium* in the rest of the report. Culture medium was refreshed every 3-4 days and the cells were passaged at about 80% confluence.

6.2.2 Cell suspension preparation

In order to obtain a set concentration of SH-SY5Y cells in liquid Matrigel, cells were cultured in a T75 culture flask until they were approximately 80% confluent, as described in section 6.2.1. These cells were used between passage 19 and 26. Before preparing the cells, Matrigel was put on ice for it to thaw at a temperature close to 0°C. Cells were then detached from the culture flask by adding 2 mL of Trypsin to the flask, and incubating for 5 minutes, after which the Trypsin was neutralized by adding 8 mL of medium. The cell suspension was then aspirated and transferred to a 15 mL falcon tube. The cells were spun into a pellet by centrifugation at 900 rpm for 5 minutes.

All medium was removed from the tube, and the cells were resuspended in 200 µL of medium. This suspension is referred to as the *original suspension* in the rest of this section.

From this suspension, 10 µL was diluted in 90 µL of medium, and used for cell counting using a NucleoCounter (Chemometec, NC-200). The cell concentration of the original suspension was computed, and adjusted to 10x the desired cell concentration in Matrigel by adding medium to the tube. 100 µL of this suspension was then left on ice for a minute to let it cool before mixing it with Matrigel. Next, 20 µL of this cell suspension was added to an Eppendorf tube containing 180 µL of thawed Matrigel, and carefully mixed using a pipette. This dilution in Matrigel resulted in the desired concentration, which was left on ice until used for encapsulation.

Cells from the original cell suspension were passaged to a new T75 culture flask: Approximately 20 µL of this high density suspension was mixed with 10 mL of medium in a 15 mL falcon tube. This more dilute suspension was then transferred to the flask and left in an incubator at 37°C and 5% CO_2. These cells could be cultured towards 80% confluence again, and used in future experiments.

6.2.3 Encapsulation

Cells were encapsulated using the setup designed in chapter 3 (Figure 3.5). Before cell encapsulation, the temperature control section of the setup was filled with water and turned on at the encapsulation settings described in section 4.2.1. First, the chip outlet was connected to a sterile Eppendorf tube, and covered with a layer of Parafilm (Parafilm, PM-996) to reduce the chance of infection. For the continuous phase, mineral oil (Sigma, M8410) containing 4 wt.% of a polysiloxane surfactant (Evonik Industries, ABIL EM 90) was aspirated into a 1 mL plastic syringe (Terumo). The syringe was installed on a syringe pump (Chemyx, Nexus 3000), and connected to the continuous phase inlet using a 20 GA needle tip (Techcon Systems, TE720050PK). Most of the inlet tube was filled with the continuous phase, by briefly running the pump at 50 µL/min. For driving the dispersed phase (the Matrigel suspension), a 1 mL plastic syringe (Terumo) was filled with mineral oil (Sigma, M8410). A 20 GA needle tip (Techcon Systems, TE720050PK) was attached to the syringe, which was installed on a syringe pump (Chemyx, Nexus 3000). The setup was now ready for injection of the Matrigel suspension, prepared as described in section 6.2.2.

Right before injection of the suspension, it was homogenized by slowly aspirating and ejecting it using a 100 µL pipette. Using this pipette, 100 µL of the Matrigel suspension was injected in the inlet of the dispersed phase, and the prepared syringe was inserted in the tube to push the Matrigel into the cooled tube section. In order to have the complete suspension in the cooled section, the pump was briefly switched on at 20 µL/min.

The chip was first filled with oil: The syringe pump of the continuous phase was turned on at 20 µL/min and left to fill the entire chip with oil and surfactant. After approximately 5 minutes, when oil started to flow from the outlet tube, the flow-rate was reduced to 10 µL/min. The pump for the dispersed phase was set to 5 µL/min, until the Matrigel suspension had moved to a distance of about 5mm from the inlet of the chip. The flow-rate of the continuous phase was now set to 2 µL/min, and the flow-rate of the dispersed phase to 1 µL/min. Setting these final flow-rates before the gel entered the chip ensured that the equilibration time of the droplet generating process was minimized.

After the gel had reached the flow-focusing section, the collection of data from the encapsulation process was initiated. Microscopic movies were made with either a regular camera (The Imaging Source, DFK 31AU03), or with a high-speed camera (Vision research, Phantom V9). Regular movies were captured for 30 seconds approximately every 5 minutes, at a frame-rate of 15 Hz. These movies were made of both the flow-focusing section and a section of the meandering channel. High-speed camera movies of the flow-focusing section were captured at a frame-rate of 3000 Hz.

When the last of the Matrigel had passed the flow-focusing section after approximately 1.5 hours, the pump for the dispersed phase was turned off. The pump for the continuous phase was set to 20 µL/min to remove all remaining beads from the chip. Beads were recovered as described in section 5.1.2.

6.3 Results

Using the high speed camera images, three different cell encapsulation modes could be identified in the encapsulation chip (Figure 6.1). As expected, both single cells and multiple cells were encapsulated in the chip. However, some cells had formed an aggregate of two or more cells, either in the Matrigel suspension, or upstream of the flow-focusing section. This also resulted in the encapsulation of multiple cells (Figure 6.1 C).

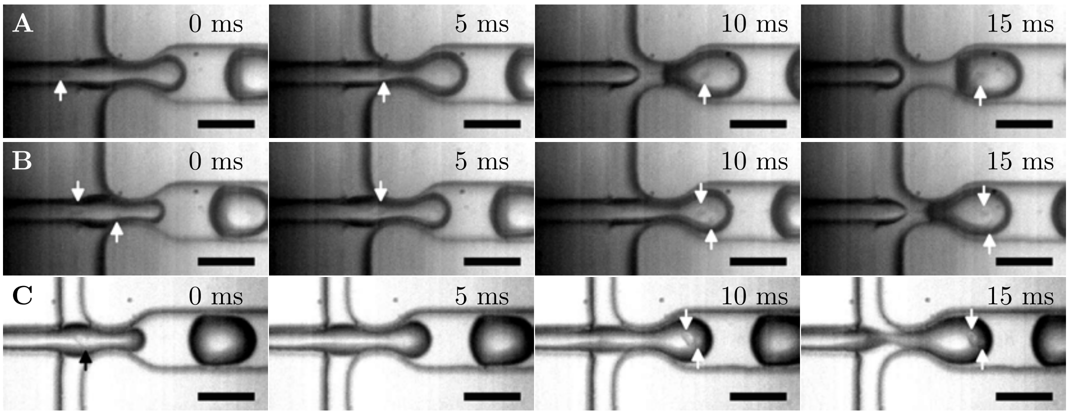

Figure 6.1 – Three different cell encapsulation modes as captured by high-speed camera. Encapsulation of a single cell, indicated with a white arrow (A). Encapsulation of two separate cells, indicated with white arrows (B). At 5 ms, the second cell is not indicated since its position of is not clear. Encapsulation of an aggregate of two cells, indicated with a black arrow at 0 ms (C). At 5 ms, the cluster is not indicated since its position is not clear. At 10 and 15 ms, the two cells are discernible, as indicated by white arrows. Scale bars indicate 100 µm.

In order to quantify the encapsulation efficiency, dark field images of a section of the meandering channel were analyzed. The distribution of cells over all droplets was estimated by counting the number of droplets containing a single cell, the number of droplets containing more than one cell, and the total number of droplets. From this analysis, it followed that only 10.6% of the droplets contained a single cell, while 4.1% contained more than one cell. This is very different from the theoretical percentages of 21.8% and 3.5%, which is most likely caused by two effects that occur inside the setup.

First, the aggregation discussed before lowered the total number of encapsulation targets in suspension, such that the total number of droplets containing any cells decreased. Additionally, the chance of multiple-cell encapsulation was increased, which explains the higher than expected percentage of droplets containing more than one cell (4.1% instead of 3.5%).

Second, the cells also sedimented or attached to the bottom of the inlet tubing, which decreased the concentration of cells in the dispersed phase. This was confirmed by an event that occurred at the end of every experiment: When the oil-water interface that pushed the dispersed phase swept through the device, an extremely high density cell suspension arrived at the flow-focusing section (Figure 6.2).

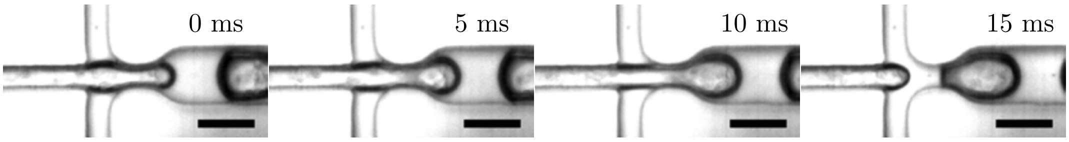

Figure 6.2 – Extremely high cell density encapsulation at the end of an encapsulation run. All scale bars indicate 100 µm.

It is clear that the efficiency of this encapsulation method is not very high, since over 85% of the generated droplets are empty. However, since part of the droplets did contain single cells, the method is usable for further analysis.

6.4 Discussion

In this chapter, it has been shown that cells can effectively be encapsulated into Matrigel droplets. However, the efficiency of the encapsulation process is not very high, and different from theory. This could be attributed to several different causes, including cell aggregation and cell sedimentation in the inlet tube. In order to improve the efficiency of encapsulation and produce a higher number of encapsulated single cells, several improvements are possible.

The issue of cell aggregation could be addressed by incorporating an aggregate-splitting microchannel design before the flow-focusing section. Mechanisms that can be used to achieve this are generally based on subjecting the aggregates to a rapidly fluctuating velocity field, effectively tearing them apart. Some examples to achieve this are a micro-pillar filled chamber [106], a splitting and merging channel section [107], and a channel of rapidly varying width to induce pinched flow [44]. Since none of these methods require any additional inlets or outlets, they could be integrated into the channel design in a straightforward manner.

The issue of cell sedimentation could be resolved by optimizing the angle of the inlet tube with respect to gravity. By aligning the inlet more with gravity, cells would be driven towards the inlet of the chip instead of the tube wall. Additionally, possible cell adhesion to the tube walls could be prevented by applying an anti-adhesive coating, such as poly(ethylene glycol).

Although these improvements would increase the efficiency of the current device, a more rigorous redesign has the potential of overcoming the limits dictated by Poisson statistics. This can either be achieved through pre-encapsulation cell ordering, or through post-encapsulation bead sorting. Several microfluidic approaches have been developed for cell ordering, such as close-packed ordering [108], pinched-flow ordering [44], and hydrodynamic ordering in Dean-flow [76] or high aspect-ratio channel flow [71]. Using these methods, single-cell encapsulation efficiencies between 55% and 80% have been reported, which is a huge improvement compared to the theoretical optimum of 21.8%.

However, encapsulating with 100% efficiency has not been reported anywhere in literature, which is mainly due to the natural variability in cell size and shape. Therefore, post-encapsulation sorting is necessary for improving the yield even further. This can either be performed on-chip, using a fluorescent signal to distinguish between empty and filled droplets [63], or in a commercial FACS machine [42]. Using this approach, combined with fluorescent cell labeling, would also improve the ease of analysis. Currently, the efficiency of single-cell encapsulation is assessed based on analysis of microscopic movies. However, the lack of contrast between the cells and their environment makes reliable analysis a challenging task. Fluorescent labeling of the cells would increase contrast, enabling more accurate detection of cells inside beads.

Using the encapsulated SH-SY5Y cells, the assembly of a spatially organized culture is tested in chapter 7, with additional focus on the viability and differentiation potential of these cells.

Chapter 7

Cell culture

In this chapter, both the assembly of a 3D culture out of the generated beads and the culturing of encapsulated cells is discussed. First, the stacking behavior of Matrigel beads in different environments, including mineral oil, culture medium, and a fluorinated oil, is tested in section 7.2.1. Using the cultures assembled in culture medium, the viability and differentiation potential of the encapsulated SH-SY5Y cells is investigated in section 7.2.2 and 7.2.3 respectively. The obtained results are discussed in section 7.3.

7.1 Materials and methods

7.1.1 Bead stacking in mineral oil

Before retrieving the beads from mineral oil as described in section 5.1.2, an experiment was carried out to test the stacking of beads in oil. The beads used in this experiment came from a generation run in an uncoated device, and had an average radius of 70.5 µm, with a dispersity of 3.3%.

These beads were sedimented inside a tube, and could be collected at high concentration using a pipette. 50 µL of bead suspension was pipetted into a 96 well plate (Greiner bio-one, 655180), after which 200 µL of mineral oil was added. This additional layer of oil prevented the oil-air interface from pushing all beads towards the walls. The well plate was then imaged using an inverted microscope.

7.1.2 Cell encapsulation and stacking in a fluorinated oil

Cells were encapsulated in perfluoropentane (PFP) (Strem, 09-6182) to test the oil evaporation approach described by Fan et al. [68]. In order to achieve this, the encapsulation method described in 6.2.3 was used with some slight modifications. PFP with 4% PFPE-PEG surfactant was used as the continuous phase instead of mineral oil. The PFPE-PEG surfactant was kindly provided to us by dr.ir. T.F.A. de Greef. The mineral oil used to push the Matrigel suspension was also replaced by PFP. Additionally, the temperature of the hot region was kept at a moderate 22°C during encapsulation, since the boiling point of PFP is at 29°C.

The resulting suspension of encapsulated cells in PFP was then used to test the stacking of beads, in combination with evaporative oil removal. In this suspension, beads were floating on top of the suspension, due to the high density of PFP: 1.63 g/m^3. Two methods of assembly were tested inside a 96 well µ-Plate (Ibidi, 89646). In the first method, the encapsulated cells were transferred by first adding approximately 5 µL of the beads, and covering them with 50 µL of culture medium. In the second method, the encapsulated cells were transferred *after* filling the well with 50 µL of culture medium. The samples were then placed inside an incubator at 37°C and 5% CO$_2$, imaged after 1 hour, and imaged again after leaving the oil to evaporate for 12 hours.

7.1.3 Culture assembly in medium

Cells were encapsulated as described in section 6.2.3, with two modifications. First, culture medium was prepared with 1% Matrigel to prevent bead disintegration and cell migration out of the beads, as described by Dolega et al. [70]. This medium was used for both bead and control samples. Second, 3D control samples were established from the same cell suspension in Matrigel as used for cell encapsulation. These samples were prepared in parallel with the beads, using the cell suspension remaining after injecting 100 µL into the encapsulation device: In 6 of the 15 wells on a 15 well µ-slide (Ibidi, 81506), 10 µL of Matrigel cell suspension was pipetted. The samples were then incubated at 37°C and 5% CO_2 for 15 minutes, after which 50 µL of cell culture medium was added.

The encapsulation process was finished approximately 1 hour after establishing the control cultures, such that the bead cultures could be assembled. All three washes were used to establish these cultures, since the yield of the retrieval protocol was too low. The tubes filled with the three washes were first centrifuged at 1000 rpm for 1 minute, to force all beads towards the bottom. Three wells on a 15 well µ-slide (Ibidi, 81506) were filled with 10 µL from wash 1. By aspirating the bead suspension from the bottom of the tube, the highest possible number of beads was transferred to each well. The same was done for wash 2 and 3. After adding the beads, 50 µL of cell culture medium was carefully pipetted on top of the assembled beads.

The leftover bead suspension was used to establish a culture in a 96 well plate (Greiner bio-one, 655180), in order to collect more data on the encapsulated cells. Again, all three washes were used, but since the wells were larger, 50 µL of bead suspension was injected. After adding the beads, approximately 200 µL of cell culture medium containing 1% Matrigel was carefully pipetted on top of the assembled beads.

7.1.4 Cell differentiation and continued culture

In order to differentiate the encapsulated SH-SY5Y cells, retinoic acid (RA) (Sigma, R2625) was added to the culture medium at a concentration of 10 µM [33], which is referred to as differentiation medium in the remainder of the thesis. At least 2 hours after establishing the cultures as described in section 7.1.3, the medium was replaced with differentiation medium. This was left on the cultures for a total of 72 hours, with a differentiation medium refreshing step after approximately 48 hours.

After the RA treatment, half of the samples received additional treatment with brain derived neurotrophic factor (BDNF) (Life Technologies, 10908010), to enhance the differentiating effects of RA [109]. The differentiation medium was replaced with medium containing 50 ng/mL BDNF, which was left on the samples for 24 hours. During the rest of the cultures lifetime, regular culture medium was used, and refreshed every other day.

7.1.5 Cell viability staining

In order to probe the viability of each sample, a ReadyProbes Cell Viability Imaging Kit (Life Technologies, R37609) was used. This kit contained Nucblue Live reagent (Hoechst, 33342) that stained cells with an intact membrane blue, and Nucgreen Dead reagent that stained cells with a compromised membrane green. Samples were stained for the first time on day 3, after which the sampled were re-stained every other day, starting either at day 5 or day 6.

For the first staining, 2 drops/mL of both reagents were added to culture medium according to the protocol provided in this kit. For all other stainings, only 1 drop/mL was added. In order to add the reagents, 50 µL of medium was aspirated from each well on the µ-slide, and 50 µL of the staining medium was added. Next, the µ-slide was incubated at 37°C and 5% CO_2 for 15 minutes, according to protocol. The samples were then imaged with a fluorescent microscope (EVOS, AMF4300) with standard blue (DAPI) and green (GFP) fluorescent filters.

7.1.6 Fixation and staining

Samples were stained for the presence of the neuron-specific protein β-tubulin III, using monoclonal mouse anti-β-tubulin III (Sigma, T8578) as primary antibody, and goat anti-mouse IgG (H+L) Alexa 555 (Molecular probes, A21424) as secondary antibody.

Samples were fixed by washing them three times with phosphate-buffered saline (PBS), subjecting them for 15 minutes to a fixing solution of 1% glutaraldehyde (GA) (Sigma, G-6257) and 1.85% formaldehyde (FA) (Merck, 104003.1000) in PBS, and washing them three more times with PBS. The GA was added to prevent depolymerization of the Matrigel matrix [35]. Next, the samples were permeabilized by subjecting them to a 0.5% solution of Triton X-100 (Merck, 1.08603.1000) in PBS for 15 minutes. Subsequently, the samples were washed two times for 5 minutes with PBS, after which a blocking solution of 10% normal horse serum (NHS) (Invitrogen, 16050-122) was put on the samples for 30 minutes. After two more 5 minute washes with PBS, a 1:200 solution of the primary antibodies in PBS with 1% NHS was left to incubate on the sample overnight.

The next day, the samples were washed 3 times for five minutes with PBS, after which a 1:200 solution of the secondary antibodies in PBS was left to incubate for 1 hour. Subsequently, the samples were washed 3 more times with PBS. The last wash was left on the sample, and it was wrapped in aluminum foil and stored in a fridge until imaging. Images were either made using a regular fluorescent microscope (EVOS, AMF4300), or a confocal microscope (Zeiss, LSM510 META NLO).

7.2 Results

7.2.1 Culture assembly: Organized bead stacking

In order to investigate the ability of Matrigel beads to self-organize in different environments, several experiments were carried out. The self-assembling properties were investigated in three different environments: Mineral oil, cell culture medium, and an evaporative fluorinated oil. Stacking was assessed in mineral oil to test whether beads were monodisperse enough to form a regularly spaced packing. However, for live cell culturing, the encapsulated cells had to be in culture medium, such that nutrient and waste transport was possible. The fluorinated oil was tested based on an approach for evaporative oil removal from literature [68], which should enable self-organization in an oil environment, and subsequent transfer to culture medium.

In mineral oil, each bead was surrounded by an oil-water interface, stabilized by a surfactant. As a result, the interaction between particles was repulsive. The driving force for bead sedimentation and packing was provided by gravity, combined with the density difference between the beads ($\rho \approx 1$ g/mL) and the surrounding oil ($\rho \approx 0.84$ g/mL). Additionally, the beads were deformable, which enabled close packing despite the slight size variation between beads. The combination of this deformity, the driving force, and repulsive interactions resulted in organized stacking of Matrigel beads with an average diameter of 141 µm and a dispersity of 3.3% (Figure 7.1).

Both double layers and triple layers of beads were present in the assembly. Locally, the beads had self-organized into a highly ordered hexagonal close packing (HCP) (Figure 7.1). A more loose hexagonal double-layered packing was also found. The fact that both loose and tight packing occurred in the same well was likely the result of the oil-air interface, which was curved such that it pushed on the beads in the center of the well.

It is clear that a dispersity of 3.3% or lower is enough to form an organized 3D stacking in mineral oil. However, for cell culturing the beads have to be in medium to facilitate interaction between cells, and nutrient and waste transport. In this situation, the driving force and bead interactions changed, such that the stacking was not as regular (Figure 7.2 A). Only locally and in one layer, some hexagonal ordering was observed (Figure 7.2 B).

This can be attributed to several differences between the culture medium and the mineral oil. First, the driving force for sedimentation was a lot less than in mineral oil, due to the smaller density difference between the beads and the surrounding medium: The medium is assumed to

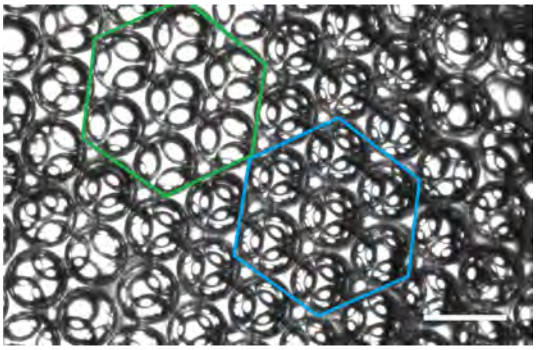

Figure 7.1 – The stacked Matrigel beads in mineral oil, with some highlights: A loose hexagonally packed double layer of beads is traced in green, a triple layer of hexagonally close-packed beads is highlighted in blue. The scale bar indicates 200 μm.

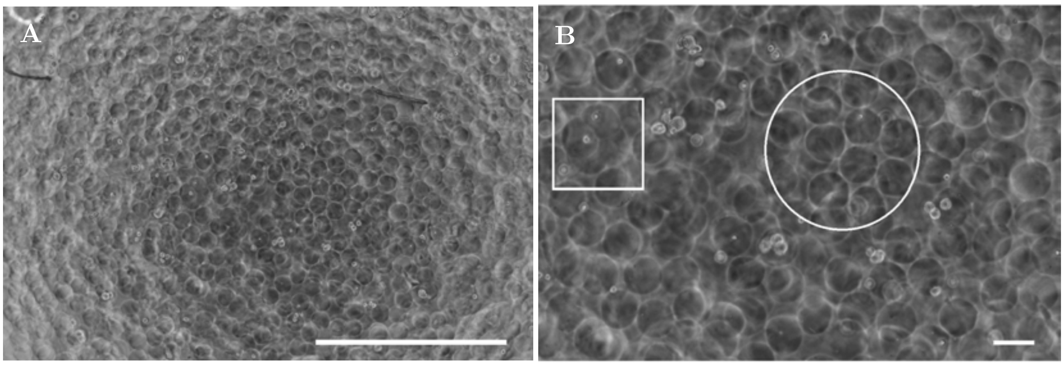

Figure 7.2 – Encapsulated cells stacked in culture medium, showing both organized and random bead distribution (A). The scale bar indicates 1000 μm. Close packed beads can be found inside the white circle, and aggregated beads can be found inside the white square (B). The scale bar indicates 100 μm.

have the same density as water ($\rho_w \approx 1$ g/mL), and the Matrigel density was estimated to be ±1.01 g/mL in section 3.1, based on the average protein concentration of 10 mg/mL. Using these densities, the driving force can be estimated using Archimedes principle. This results in a driving force of 0.05 nN in medium as opposed to 0.87 nN in mineral oil, indicating a reduction in force of over an order of magnitude.

Second, since the beads are not separated by two oil-water interfaces, matrix proteins in different beads can interact with each other. This makes beads attractive instead of repulsive. Third, the beads do not assume a spherical shape that is as smooth as in mineral oil, which could be the result of plastic deformations during the centrifugation steps, or the lack of an interface that forces the beads in shape by surface tension. Although the deviations seem to be small, it could just be enough to limit the free rotation and movement of the beads. Finally, some of the beads have aggregated into irregular shapes (Figure 7.2 B).

For the cell culturing experiments discussed in sections 7.2.2 and 7.2.3, it is important to note that not all wells contained an equally high number of beads. Some wells contained only a few beads, which is a result of the manual pipetting steps involved. The samples with high bead density were used for further analysis.

It is clear that the presence of a significant driving force and repulsive bead interactions are important for self-organization. Therefore, a preliminary experiment was carried out to test the assembly in an oil phase, followed by oil removal through evaporation as previously demonstrated by Fan et al. [68]. In order to achieve this, the continuous phase was replaced by perfluoropentane

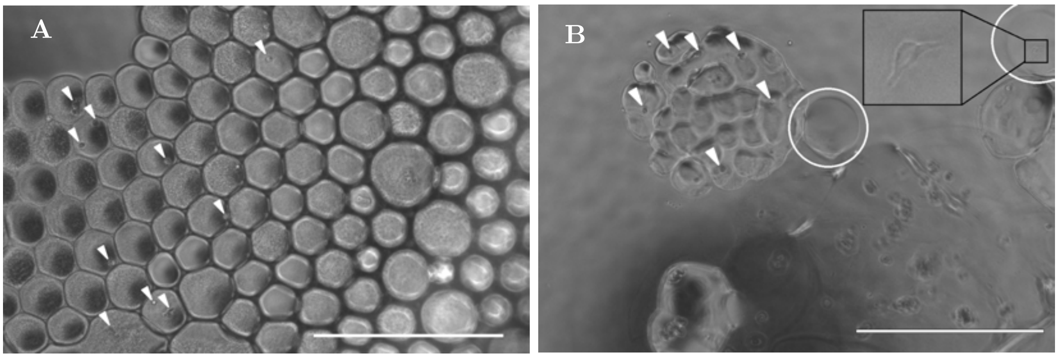

Figure 7.3 – Encapsulated cells stacked in PFP after 1 hour of incubation, showing a monolayer of organized beads (A). The beads have a relatively high dispersity compared to those made in mineral oil. The positions of cells are indicated using white arrows. Encapsulated cells stacked in PFP after 12 hours of incubation (B). Most of the beads have coalesced, and some beads have become smaller and seem to be squeezed in an oily substance. Two beads, circled in white, seem to have moved from the PFP to the cell culture medium. The enlarged view shows a single live cell inside one of these beads. All scale bars indicate 400 µm.

(PFP), which has a boiling point at 29°C, with a PFPE-PEG surfactant to stabilize the beads. Since this oil is much denser than the beads ($\rho_{PFP} \approx 1.63$g/mL), the beads will rise to the oil-medium interface instead of sinking to the bottom. Unfortunately, some practical difficulties during cell encapsulation in PFP lead to the generation of a very low number of encapsulated cells. Therefore, only a small scale experiment could be carried out. Additionally, the beads were more polydisperse, as a relatively large number of beads was generated in the initial (unstable) phase.

Two different methods of establishing the culture were tested: Pipetting the beads in a µ-plate and then adding medium, or first adding the medium and then the beads. The latter method resulted in the least amount of coalescence, but the reason for this is yet unknown. The beads collected at the oil-water interface, and organized in a similar manner as in mineral oil (Figure 7.3 A). The fact that only a single layer of beads is visible can be attributed to the low number of beads in the suspension. The beads seem more deformed than in mineral oil, which could be attributed to three factors. First, the mechanical properties of the beads might have changed, since the encapsulation had to take place at a lower temperature of 20°C. Second, the density difference between the beads and PFP is larger than in mineral oil, which leads to a higher buoyancy force of approximately 3.18 nN as opposed to 0.87 nN in mineral oil. This could have increased the load on the beads, leading to more deformation. Third, the surface tension of PFP is lower than of mineral oil due to the lower surface energy associated with fluorinated materials, which reduces the tension that forces droplets to become spherical.

The beads were left in an incubator at 37°C and 5% CO_2 for 12 hours (Figure 7.3 B). Two beads seemed to have moved from the PFP to the culture medium. In one of these beads, a viable cell also seemed to be present. However, lots of beads had coalesced or reduced in size and aggregated. The cells that still remained in these beads were most likely dead, due to nutrient depletion and buildup of toxic metabolites. Apart from this, an oily substance remained in the wells, which was likely the remaining PFPE-PEG surfactant. Clearly, this approach is not yet usable for establishing an organized cell culture in medium. However, the transfer of some beads to medium and the survival of one encapsulated cell seem to indicate that this method could be feasible in the future.

From the performed stacking experiments, we can conclude that full spatial organization of live cells is not yet achievable using one of the tested methods. However, we have shown that a culture can be assembled from the encapsulated beads, by transferring them to medium and letting them settle in a µ-slide. Moreover, the stacking experiments in both oils show that high levels of organization can be reached under the right conditions.

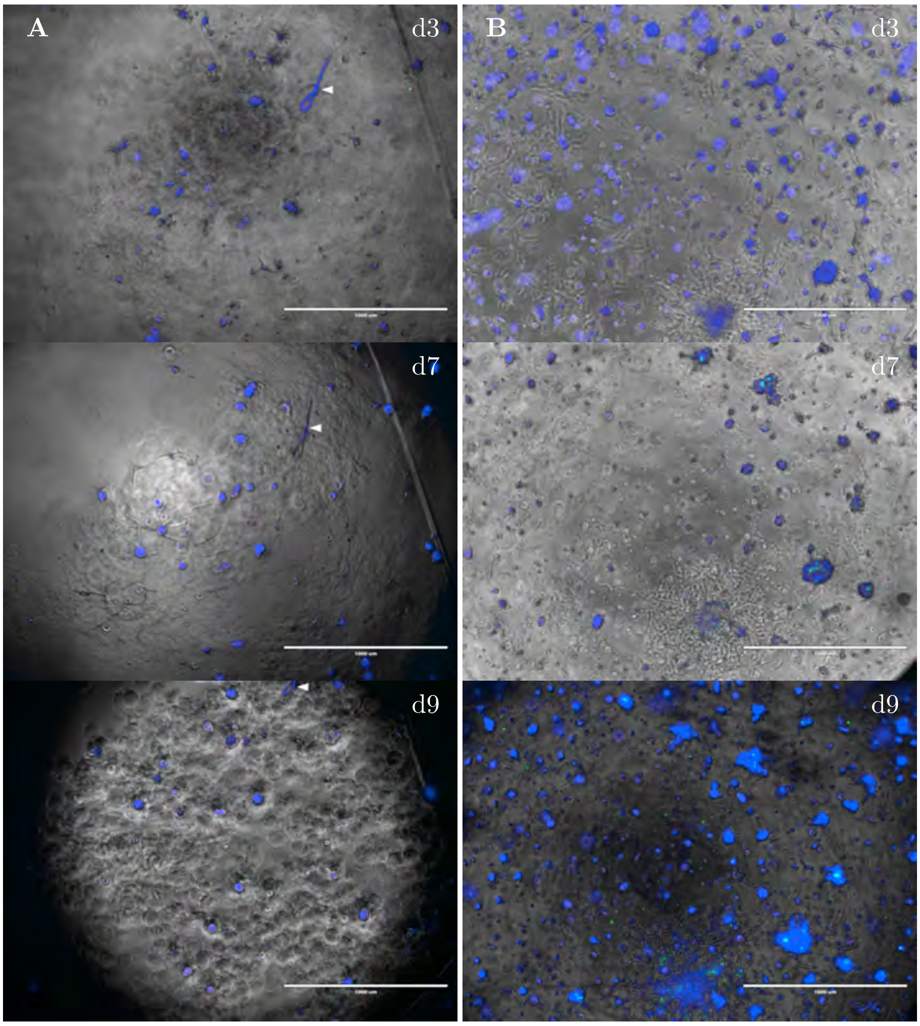

Figure 7.4 – SH-SY5Y cells stained for viability in a culture from encapsulated cells stacked in culture medium (A), and a 3D Matrigel control sample from the same batch of cells and Matrigel (B). The samples were stained on day 3, 5 (not shown), 7, and 9, blue/green indicates an intact/compromised cell membrane. Some variations between the images, such as the dark edges and lighter/darker center regions, are caused by optical distortions as a result of the lens effect of the medium air interface. A dust particle is visible (A), indicated with a white arrow. All scale bars indicate 1000 µm.

7.2.2 Cell viability: A qualitative analysis

For the successful formation of a 3D neuronal culture, it is essential that enough cells survive the encapsulation process. In this section, the viability of encapsulated cells is assessed with respect to 3D Matrigel control samples.

Unfortunately, a quantitative analysis of the viability was not possible for two main reasons: First, the bead density varied between wells, which did not facilitate systematic sample comparison. Second, the cultures were all in 3D, which made quantification of the total number of live and dead cells very difficult. Due to the limited depth of field of the microscope used, only part of the 3D sample could be imaged at a time. In addition, cells that were out of focus could significantly impact the signal-to-noise ratio, by introducing lens-distorted background noise.

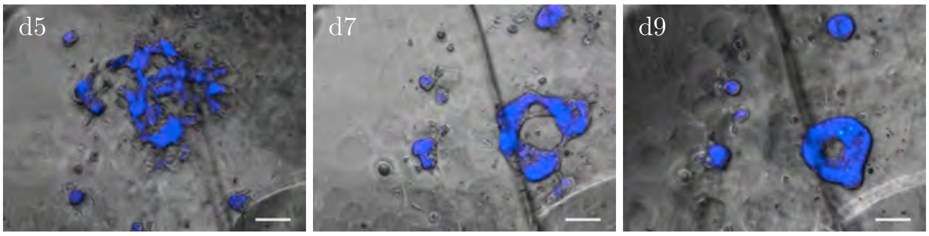

Figure 7.5 – A culture from encapsulated SH-SY5Y cells stacked in culture medium, stained for viability on day 5, 7, and 9, where blue/green indicates an intact/compromised cell membrane. Cells seem to have started to form outgrowths on day 5, but these have completely disappeared on day 9. All scale bars indicate 100 μm.

Therefore, a qualitative analysis was performed on a typical successful culture of encapsulated cells, and a control sample in a 3D Matrigel matrix (Figure 7.4). Both samples were generated on the same day, from the same culture flask, using the same batch of Matrigel.

The most important observation is that almost all cells in the bead culture were alive on day 3, indicating that the encapsulation and retrieval procedure was not detrimental to cell viability. Given that both the used oil and surfactant are not classified as biocompatible materials for cell encapsulation, this is a very good result. Their negligible effect on cell viability can be attributed to the relatively brief 1.5 hour exposure to the surfactant. Moreover, isolation from nutrients and gas exchange by the oil was just as brief.

Additionally, compared to the Matrigel control sample (Figure 7.4 B d3), similar numbers of dead cells were found relative to the total number of cells. In both samples, especially isolated single cells seemed to have died, which was expected based on the need of neurons for interaction with neighboring cells. On day 7 and 9, especially the viability in the control sample was decreasing, although some additional cell death was also observed in the bead culture. This indicates that the bead culture is at least as viable as the control samples.

However, some experimental differences between the two samples could have influenced the result, limiting the validity of the comparison above. The first notable difference between the two samples is the total number of cells: The gel control sample contained many more cells and cell clusters than the bead sample. This difference had a number of causes, related to the way cells were encapsulated and the beads were stacked. First, the cell encapsulation method was not optimal, partially due to the loss of cells in the device inlet, as discussed in chapter 6. As a result, the total number of encapsulated cells was lower than the initial total number of cells in Matrigel suspension. Second, the total volume of gel was lower in the bead culture, due to the variability of the number of beads that were transferred when establishing the culture. Finally, the stacking of beads inherently resulted in a lower volume of gel in the culture, since the densest possible packing of spheres fills only 74% of the total volume. As a result, the overall cell density reduces with 26%, even at an encapsulation efficiency of 100% and dense packing.

The higher cell density in the control sample is expected to be the main cause of the higher amount of cell death, since both samples received fresh medium at equal intervals. At the higher cell concentration, less nutrients are available per cell, and the buildup of toxic waste products is faster. Another factor that could have contributed is the seemingly higher proliferation rate in the control sample. This is most apparent in the larger cell clusters in this sample. This can lead to nutrient depletion and waste buildup in the core of the cluster, locally inducing cell death. This was observed in many of the larger clusters (Figure 7.4 B d7 and d9).

Another notable thing is that the morphology of the cells changed over time. On day 3, irregular cell clusters that formed outgrowths were observed in both samples, but on day 9 these outgrowths seemed to have disappeared. A large cluster of cells in another bead culture was followed from day 5 until day 9 to study this in more detail (Figure 7.5). Both the cell morphology and distribution in the 3D environment changed significantly, leading to tight clusters of cells with no extensions.

A probable cause for this cell behavior is the viability staining, which could have interfered

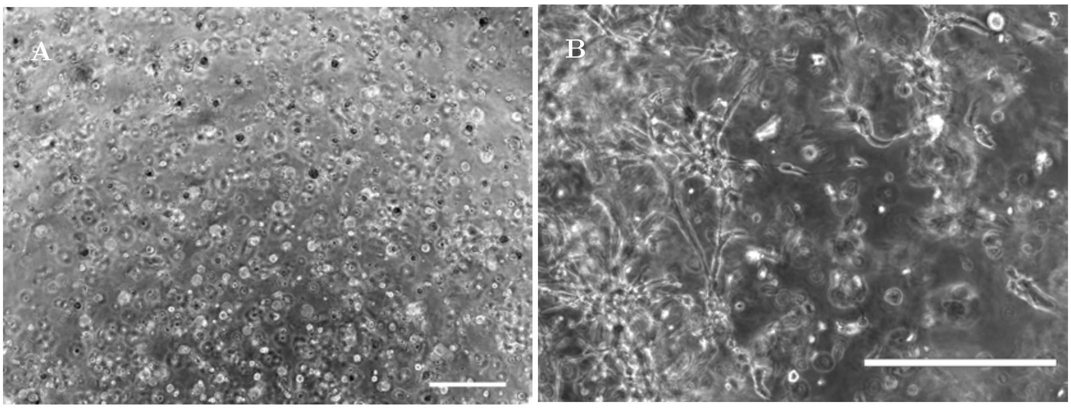

Figure 7.6 – Two samples from the same batch of SH-SY5Y cells in a 3D Matrigel matrix, treated with RA and imaged on day 7. One sample in a µ-slide, which had repeatedly been stained for viability, contained cells that had not formed connections and had a spherical morphology (A). The other sample in a 69 well plate, which had not been stained, contained cells that formed neurites and connections (B). Scale bars indicate 400 µm.

with the cell development. This becomes apparent when comparing a Matrigel control sample that had been stained for cell viability with a sample that had not been stained (Figure 7.6). While the untreated sample showed cells that were spread throughout the culture, with an abundance of extensions and connections, the stained sample showed mostly isolated, spherical cell clusters. The viability live-staining seems to have affected the cell culture, influencing both the morphology (no outgrowth formation) and cell distribution (cells formed tight, spheroid-like cultures).

Despite this detrimental impact on cell morphology, it is clear that the encapsulation, retrieval, and assembly processes enable the creation of a 3D culture from encapsulated SH-SY5Y cells. The bead culture remains viable for at least 9 days, which should be enough for neuronal differentiation, discussed in the next section.

7.2.3 Cell differentiation

Each culture was treated with RA to drive differentiation, such that the SH-SY5Y started to form neurites, and connect to one another. Differentiation was assessed based on morphological properties of the cultured cells in the form of neurite outgrowth and antibody staining for β-tubulin III, which is a neuron specific component of the cytoskeleton. In this section, the main goal is to determine if the encapsulated cells did not only remain viable, but also retained their differentiation potential. This is an essential part of the formation of a neuronal network by SH-SY5Y cells.

Phase contrast images were made of beads containing single SH-SY5Y cells that were treated with RA. Single cells inside beads had formed outgrowths on day 3, indicating that the cells were driven to form neurites by RA (Figure 7.7 A-C). Although these images were made on day 3, which was too early to determine whether the outgrowths were neurites, the first developments seem to indicate that the cells are in the right environment for differentiation. A cell that had formed two outgrowths, of which one had fully penetrated a neighboring bead, was also observed on day 4 (Figure 7.7 D). This indicates that the formation of connections between beads is possible, if neighboring beads contain cells. In cultures that were not treated with a viability staining, outgrowths were also observed on day 7 (Figure 7.7 E), including very long ones that penetrated the environment outside of the bead (Figure 7.7 F). This shows that SH-SY5Y cells can also differentiate over a longer time span, as long as no viability staining is performed.

In two cultures in a 69 well plate, cells were close enough to form connections (Figure 7.8). Two cultures are shown: One with a relatively high number of beads (A, B), and one with a very low number of beads (C, D). In the culture with many beads, local clusters of cells with many

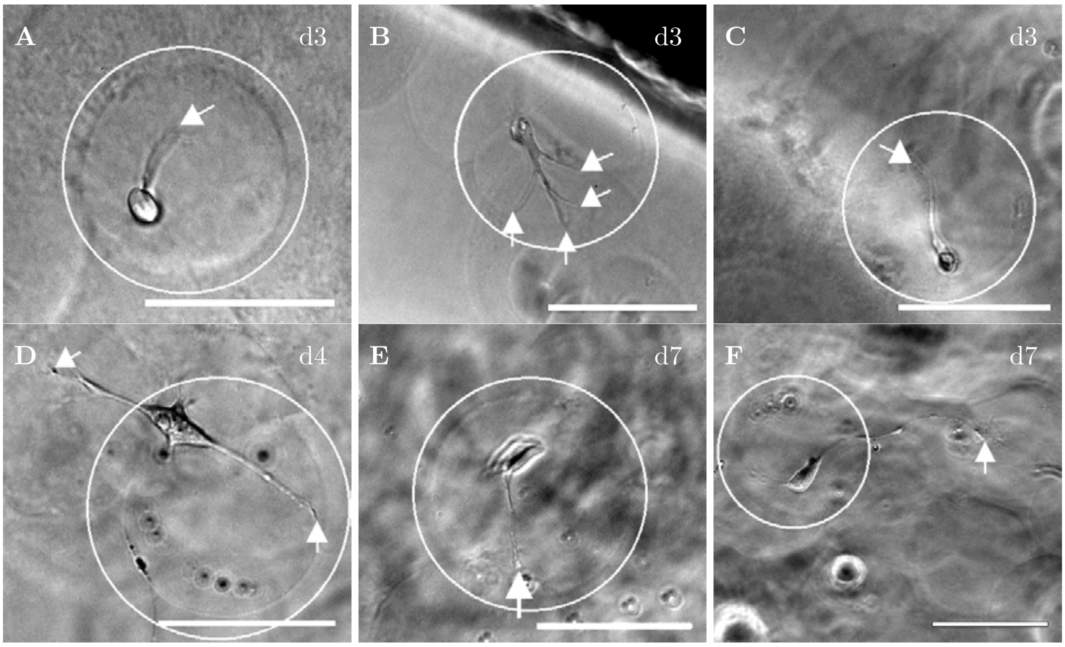

Figure 7.7 – Encapsulated SH-SY5Y cells treated with RA for 72 hours, showing developing neurites. The encapsulating beads are surrounded by a white circle, and the approximate endpoints of developing neurites are indicated with a white arrow. Single-cells with developing neurites were captured in different wells from a sample in a μ-slide on day 3 (A-C), in a 96 well plate on day 4 (D), and in a μ-slide that had not been stained for viability on day 7 (E, F). All scale bars indicate 100 μm.

connections had formed. These cells formed a network in a 3D environment, which was most apparent where one cell cluster with several neurites connected to a cell cluster that was not in focus (Figure 7.8 B). It is not completely clear whether these connected cells were all original cells that were present during encapsulation, or whether they were the result of proliferation inside the culture.

In the dilute bead culture, something interesting happened: Again cells seem to have formed a network, but seemingly *around* the few beads that were present in the well (Figure 7.8 C, D). From this position, the cells connected to other cells that were in a 2D conformation (Figure 7.8 D). This cell behavior can possibly be exploited to create a different type of 3D culture, where cells locally are in a 3D configuration, while communicating with other isolated 3D cultures. However, within the context of this thesis, this behavior is unwanted.

It is important to note that half of the culture samples was also treated with BDNF, but no notable difference was observed. This might have been a result of the issues related to the viability staining, or due to the culture stacking variability between different samples.

In order to determine whether the observed morphological changes are actually showing differentiation into neurons, an antibody staining was performed. Unfortunately, many samples were lost in the fixation process, due to depolymerization of the Matrigel hydrogel when only using formaldehyde as a fixation agent. By including GA in the fixation solution [35], this problem was circumvented, such that a sample could be fixed and stained for β-tubulin III. This sample did not contain a large number of beads, such that a true 3D stacking of encapsulated cells could not be observed. Despite having been treated with the viability staining once, some cells had formed outgrowths (Figure 7.9).

Several cells were stained positively for β-tubulin III (red) (Figure 7.9 A, B), indicating that the cells had indeed differentiated into neurons. The larger red spheres that appear in the image are actually Matrigel beads that have become auto-fluorescent due to the GA used for fixation. Interestingly, most cells seem to lie in the same plane, which indicates that they have migrated

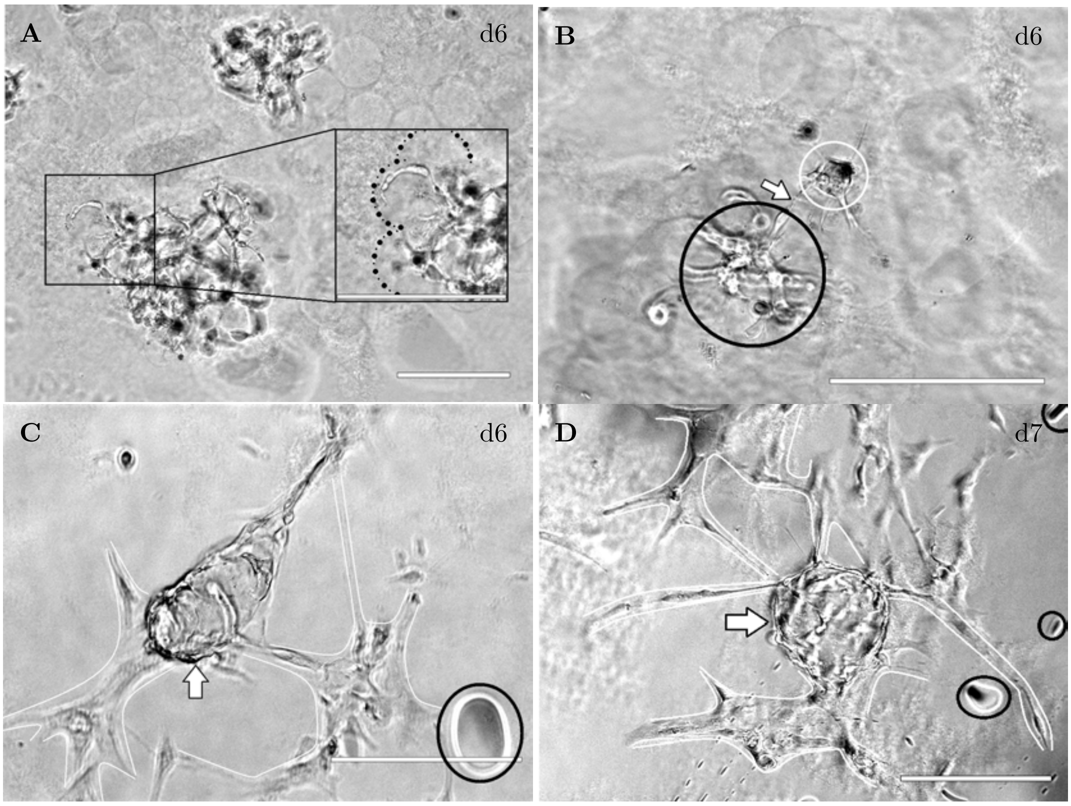

Figure 7.8 – Encapsulated SH-SY5Y cells in bead culture in a 69 well-plate, treated with RA for 72 hours. Morphologically differentiated cells that locally form networks can be found in a culture containing many beads (A, B). In the enlarged view in (A), bead edges are outlined using black dots. 3D connectivity was observed in a cell cluster with several neurites, which connected to cells in a different focal plane (B). The cell cluster is circled in white, and the cells it connects to are circled in black. The neurite connection is indicated with an arrow. In a dilute bead culture, neuronal cells were found to grow around beads (C, D), while connecting to neuronal cells in 2D conformation. The beads are indicated with an arrow, and the 2D neuronal cells are roughly outlined in white. Some oil residue was also found in this culture, as indicated by black circles (C, D). All scale bars indicate 200 μm.

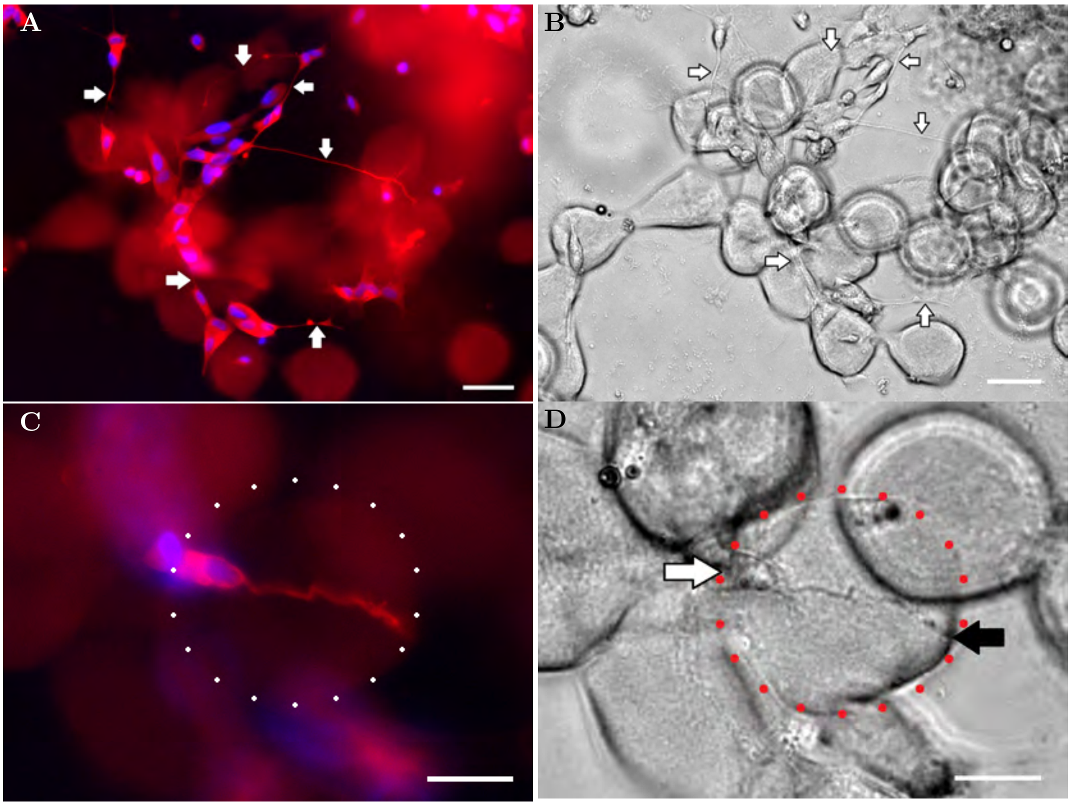

Figure 7.9 – Fluorescent and phase contrast image of differentiated SH-SY5Y cells in Matrigel bead culture, fixed on day 10. Cells were stained for the DNA inside the nucleus (blue) and the neuron specific protein β-tubulin III (red). The fixation protocol caused some autofluorescence of the beads (red). Several differentiated cells forming neurites and connections were found (A, B). Some neurites are indicated using white arrows. The scale bar indicates 100 μm. In the same culture, a single differentiated cell with a neurite inside a Matrigel bead was also found (C, D). The approximate shape of the surrounding bead is indicated using white or red dots (C, D), the position of the cell body with a white arrow (D), and the neurite end with a black arrow (D) Here, the scale bar indicates 50 μm.

towards the bottom of the culture. Just one single cell that was clearly growing a neurite inside a bead can be identified (Figure 7.9 C, D).

In order to obtain a more complete image of the 3D morphology of the differentiated neurons, confocal images were made of a bead culture and a gel control culture (Figure 7.10). Due to limitations of the used confocal microscope, only the β-tubulin III staining is shown. Several neurons were found in a bead culture, with clearly discernible connecting neurites (Figure 7.10 A). Some cells had a spherical morphology without any processes, which is thought to be related to the viability staining as argued before. One neuron in particular had formed outgrowths that were clearly in 3D, which is especially visible in the projections that show the height. Multiple upward pointing extensions can be identified, which indicates the neuron is encapsulated inside a bead, although it is difficult to discern the bead itself.

Similarly, both cells with neurites and spherical cells are visible in the 3D Matrigel control sample (Figure 7.10 B). Interestingly, both cells that have formed neurites and the cells with spherical morphology stain positively for β-tubulin III, which could indicate that even the cells with no neuronal morphology have been driven to differentiate to some extent. However, since these cells do not form connections, they will never be able to form a neuronal network, as is the case with neurite carrying cells.

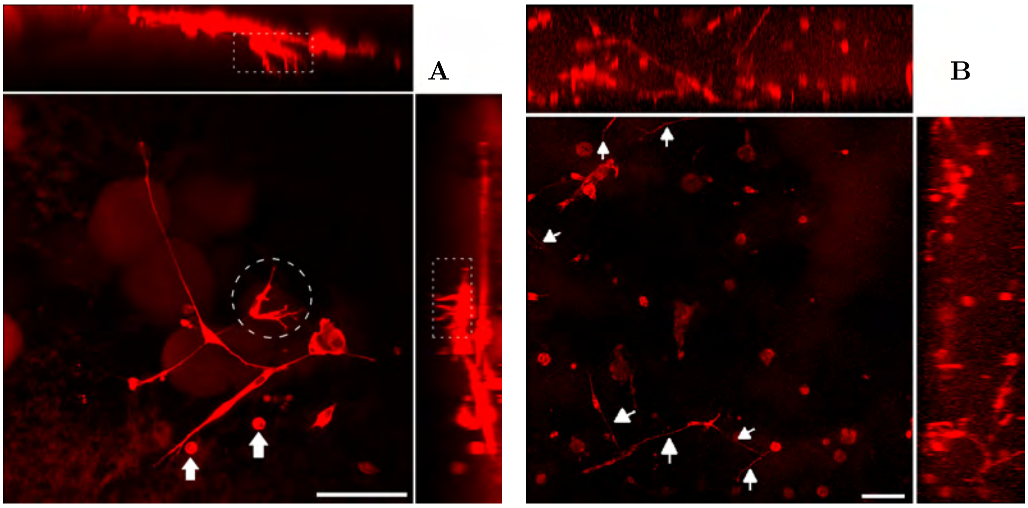

Figure 7.10 – Orthogonal highest-intensity projections of a z-stack of confocal images of encapsulated SH-SY5Y cells (A), and a 3D control sample from the same batch of cells and Matrigel (B) stained for β-tubulin III. In the sample from encapsulated cells ,a neuron that has formed outgrowths in 3D inside a bead is circled, and two cells that have not formed neurites, but did positively stain for β-tubulin III are indicated with white arrows (A). In the control sample, some neurites are indicated with arrows (B). The samples were fixed and stained on day 10. The scale bars indicate 100 μm.

7.3 Discussion

In this chapter, the assembly of a 3D culture from the encapsulated cells is shown. The cells are viable after encapsulation, and retain their differentiation potential. However, the spatial organization of encapsulated cells through bead stacking in cell culture medium has not been achieved yet. This is mainly the result of the lack of a driving force for self-organization, and the attractive interactions between beads. Possible solutions are therefore based on changing either the driving force or the interactions.

Currently, the only driving force for packing the beads is gravity, which leads to a net buoyancy force on each bead. For beads in medium, this driving force is very limited due to the small density difference between beads and medium. Since buoyancy scales linearly with acceleration, centrifugation could be employed to increase the net driving force for bead motion. However, this might damage the beads themselves, or even force cells out of beads. In order to specifically drive the beads, a bio-orthogonal method could also be applied. For example, small paramagnetic beads could be encapsulated in the beads, along with a cell. By applying a magnetic field gradient to the suspension, the beads could be forced in the direction dictated by the magnetic field. However, this method would complicate the setup, as local control over a magnetic field gradient is required. Moreover, the paramagnetic beads could have adverse effects on the encapsulated cells.

The most viable option for driving bead ordering might be the use of flow in a microfluidic device. Droplet self-assembly into an organized packing has already been demonstrated inside a microfluidic device [110]. By integrating a sieve structure into the assembly chamber, the self-assembled droplets could be captured. An interesting property is that the driving force becomes a function of the distribution of beads: If a certain area of the sieve is not covered in beads, the lower local hydraulic resistance will increase the flow into this area, leading to the addition of more beads. In addition to the previously demonstrated self-assembly, a reason for selecting this option as the most viable method is the fact that flow acts mostly on the boundaries of the beads. This should limit the possible damage or disturbances inside of a bead, which could be detrimental to the encapsulated cells.

In an attempt to assemble the culture in an oil that can be removed by evaporation, perfluoropentane was used for encapsulation. The experiment shows that high levels of self-organization can also be achieved in this environment. However, some challenges still have to be overcome before this method could be used to establish an organized culture. First, the encapsulation process itself has to be modified to work with a low boiling-point liquid, such that stable encapsulation is possible. Second, the coalescence of the beads during evaporation should be prevented, which could be possible by optimizing the surfactant concentration, or evaporation at a lower temperature. Third, there are still some uncertainties about the influence of evaporation on the beads, and the influence of the surfactant on the evaporation process. Therefore, more research is required to determine the feasibility of the method.

Alternatively, the interaction between beads could be modified by changing the encapsulation material. The fact that Matrigel gelates at temperatures above 10°C is thought to be the reason for the observed bead interactions; The protein constituents are still able to form bonds with the proteins in other beads. The most straightforward manner to avoid this would be to select a hydrogel that only gelates in the presence of a certain stimulus that is not present in culture conditions. An example of such a hydrogel is alginate, which gelates in the presence of divalent ions [62]. Other hydrogels that use a cross-linking molecule for gelation, such as hPG-PEG [69], could also be used. Another option is to add the other material as a layer around the beads, for instance by encapsulating the beads in this other material. However, the impact of using another hydrogel on the development of SH-SY5Y cells has to be carefully assessed before implementing such a solution.

When both the encapsulation efficiency and the stacking have been improved, the cell density and distribution is more controlled. However, for accurate comparison with a 3D Matrigel culture, the density of these control samples have to be tuned to take the 26% reduction in cell density due to the sphere packing into account.

For future work, it is essential that the differentiation and network formation of SH-SY5Y cells in bead culture is assessed over a longer time span. Since the viability staining used has been shown to affect both the morphology and distribution of cells, this staining is not to be used as a mid-point measurement, but rather as an end-point measurement.

In conclusion, both the viability and differentiation experiments have shown that cell encapsulation for the establishment of a 3D neuronal culture is feasible: The cell viability is not significantly affected by the encapsulation procedure or the retrieval process, and the SH-SY5Y retain their differentiation potential in the beads.

Chapter 8

Conclusions and recommendations

In this work, the main aim was to develop an approach to spatially organize neuronal cells in a 3D cell culture, based on the encapsulation of single cells into monodisperse hydrogel beads. To tackle this challenge, four sub-goals were defined in section 1.0.1 (Box 2).

BOX.2: The aims of this project.

1. Develop a temperature control method for a microfluidic droplet generator
2. Implement the developed temperature control method in a microfluidic device that can generate monodisperse Matrigel beads.
3. Achieve single-cell encapsulation in monodisperse Matrigel beads of live SH-SY5Y cells.
4. Assemble the encapsulated cells into an organized and viable culture, that can form a network.

In section 8.1, the main conclusions that can be drawn from the work presented in this thesis are discussed for each of the defined goals. Recommendations for the future development of this approach for spatially organizing neuronal cultures are provided in section 8.2.

8.1 Conclusions and outlook

Temperature control for Matrigel bead generation

Local control over temperature of the microfluidic device was necessary to generate monodisperse Matrigel beads. A cold region with a temperature between 0 and 4°C was required for droplet generation of liquid Matrigel. A hot region with a temperature of 37 °C was required for gelation of Matrigel, counteracting droplet coalescence, and maintaining cell viability. In this work, a temperature control device was designed based on the exchange of heat between the microchannels and two chambers below the chip. The design was validated using simulations of heat-transfer and temperature measurements on the device. Additionally, a calibration curve was derived based on temperature measurements. Using this curve, we have shown that the temperature control method enables the generation of a cold region below 4°C and a hot region at 37°C, as required for Matrigel droplet generation and on-chip bead gelation. Therefore, we can conclude that the first aim, the development of a temperature control method for a microfluidic droplet generator, has been achieved.

Reproducible monodisperse Matrigel bead generation

Using the validated temperature control chambers, monodisperse Matrigel beads were generated in the designed chip. A hydrophobic surface coating was applied to the device, such that the generation of monodisperse beads was reproducible across different devices. We have shown that Matrigel droplets can be generated with an average diameter of 94.6 µm and dispersity of 2.4%.

The droplets gelated on the microfluidic chip and could be retrieved from the continuous phase, using several washing steps with oil and culture medium. In the resulting bead suspension, a slight decrease of the average bead diameter was observed, resulting in a final average diameter of 92 µm. The dispersity increased to approximately 4.4%, which is below the 5% limit for monodispersity.

Several challenges still remain, such as reducing the observed coalescence of droplets on the chip, which is thought to be one of the causes for the increased dispersity. Another challenge is increasing the low yield of the bead retrieval process, during which a significant part of the generated beads was lost. Recommendations for overcoming these challenges are provided in section 8.2. Nonetheless, we can conclude that the second aim, the generation of monodisperse Matrigel beads, has also been achieved.

Single-cell encapsulation of SH-SY5Y cells

SH-SY5Y cells were encapsulated in Matrigel beads by suspending the cells in the Matrigel during droplet generation in the microfluidic chip. An optimal cell density was selected based on the Poisson statistics that govern encapsulation, such that a high number of beads (21.8%) should contain a single cell, and only 3.5% more than one cell. However, the measured percentage of beads containing a single cell was just 10.6%, and the percentage of beads containing multiple cells was 4.1%. This could be attributed to cell aggregation and sedimentation before encapsulation, which increased the chances for multiple-cell encapsulation and reduced the number of cells in suspension. Although we can conclude that the third aim has been achieved, given that single-cells were encapsulated, encapsulation at higher efficiency is necessary for the success of the approach for spatial organization. Recommendations for improving the efficiency are provided in section 8.2.

Spatially organized culture of viable and differentiated SH-SY5Y cells

Using the encapsulated cells, a 3D culture of SH-SY5Y cells has successfully been established. However, due to the aforementioned low encapsulation efficiency, single cells were too isolated to form a network in most cases. Additionally, the spatial organization of encapsulated cells in culture has not been achieved yet. When the beads were still in the continuous phase, near perfect hexagonal bead packing was observed. However, when the culture was assembled in cell culture medium, this level of organization was no longer achieved. This is expected to be the result of the lack of a significant gravitational driving force, due to the small density difference between the beads and the medium. Additionally, the beads seem to bond together, such that the self-organization process is disrupted.

Despite the low cell density and lack of spatial organization, the impact of the encapsulation on cell viability and differentiation potential could be assessed in the established bead cultures. Using a viability staining, the encapsulated cells were shown to be viable for at least 9 days after encapsulation, which indicates that this process is not detrimental for cell viability. In addition, neurite formation and positive antibody staining for β-tubulin III was observed in bead culture, which indicated that the SH-SY5Y also retain their differentiation potential. It is important to note that in one sample that contained groups of SH-SY5Y cells at a high enough density, local growth of a highly connected network was observed, indicating that the bead environment is supportive of network formation.

These results show that the use of microfluidic encapsulation and culture assembly are compatible with SH-SY5Y cells, which is essential for future development of this technology. Therefore, we can conclude that the fourth aim, assembly of a spatially organized and viable neuronal culture that is able to form a network, is partially achieved. Recommendations for improving spatial organization in future work are provided in section 8.2.

Outlook

In this work, we have shown that single-cell encapsulation in Matrigel can be achieved using the developed setup. Moreover, the cells survive this process and retain their potential to differentiate and even form a network. When the proposed improvements in the next section are implemented, full control over the spatial organization in a 3D neuronal culture should be achievable. This is a great step forward in developing brain tissue models to study the underlying mechanisms of brain diseases, in combination with a read-out of electrophysiology via MEA. In future work, the method could also be applied to co-culture different cell types, to further increase the relevance for studying more complex brain diseases. An example is Alzheimer's disease, which arises from the disruption of multiple cell types. Additionally, the approach is not limited to neuronal cultures, but could also be applied for achieving organization in other kinds of tissue.

8.2 Recommendations

Several challenges remain before the proposed approach for spatial organization is fully functional. In this section, recommendations are provided in order to address the main challenges, or improve the technology. Recommendations relevant to specific experimental details are provided in the discussion sections of chapters 4 – 7.

Expanding the radius range for future experiments
For future experiments, it is desirable to have full control over the diameter, in order to vary the inter-cellular spacing between encapsulated cells. Here, only a reproducible diameter of approximately 100 µm is shown, but smaller radii are also possible in the current device, as indicated by the radius scaling discussed in section 2.2. For producing larger droplet diameters, the height of the device should be adjusted, as not to create non-spherical beads.

Improving the yield of bead retrieval
A microfluidic approach is recommended for improving the yield of the bead retrieval process. Incorporation of a channel design that enables the transfer of beads from the oil phase to medium could greatly improve the controllability of the process. For instance, a channel geometry could be incorporated that forces beads through co-flowing streams of clean oil to reduce surfactant concentration, and culture medium, using a micro-post array [105]. Due to the slow diffusion at this scale, as discussed in section 2.1.2, mixing of the co-flowing streams could be prevented by applying a high enough flow-rate. Alternatively, a hydrodynamic oil replacement method similar to the one described by Kim et al. could be employed to wash the beads on-chip [60].

Preventing coalescence in the encapsulation chip
A design change to the meandering channel section is proposed to reduce the risk of coalescence. As described in chapter 3, this channel section was optimized to minimize the pressure drop, which resulted in a relatively wide channel. Since the device is operated at relatively low flow-rates relative to the designed maxium, the channel width could easily be reduced, in order to decrease coalescence due to collisions caused by different droplet velocities.
m

Reducing cell loss and aggregation in the encapsulation chip
Cell loss in the inlet of the device could be prevented by incorporating an anti-adhesive coating, such as poly(ethylene glycol). Alternatively, the inlet channel could be placed at a more vertical angle, such that gravity drives the cells towards the device instead of the tube walls. The issue of cell aggregation could be addressed by incorporating an aggregate-splitting microchannel design before the flow-focusing section. Examples to achieve this are a micro-pillar filled chamber [106], a splitting and merging channel section [107], and a channel of rapidly varying width to induce pinched flow [44]. All of these methods could be integrated into the channel design in a straightforward manner, since no additional inlets and outlets are required.

Increasing the single-cell encapsulation efficiency
The encapsulation efficiency can be improved using two different methods: Pre-encapsulation ordering of cells and post-encapsulation sorting of beads. For optimal yield of beads containing a single cell, a combination of both methods is recommended. Pre-encapsulation ordering methods overcome the Poisson statistics by ordering cells such that they arrive in sync with the droplet generation process. Several examples are close-packed ordering [108], pinched-flow ordering [44],

and hydrodynamic ordering in Dean-flow [76] or high aspect-ratio channel flow [71]. Using these methods, single-cell encapsulation efficiencies between 55% and 80% have been reported, which is a huge improvement compared to the theoretical optimum of 21.8%. Post-encapsulation sorting can then be applied to further refine the beads, which can either be performed on-chip, using a fluorescent signal to distinguish between empty and filled droplets [63], or in a commercial FACS machine [42].

Achieving organized packing of Matrigel beads in medium

As opposed to the challenges addressed above, a solution to the issue of a lack of organization is less straightforward. However, it is expected that a microfluidic approach is the most feasible option. By driving the beads to self-assemble inside a confined microfluidic chamber with integrated sieve, organized stacking is likely achieved. Using this flow-based approach, the driving force for bead organization becomes a function of the distribution of beads: If a certain area of the sieve is not covered in beads, the lower local hydraulic resistance will increase the flow into this area, leading to the addition of more beads. Alternatively, the evaporative removal of oil tested in chapter 7 could be investigated further.

Bibliography

[1] D C Hesdorffer, G Logroscino, E K T Benn, N Katri, G Cascino, and W A Hauser. Estimating risk for developing epilepsy: A population based study in Rochester, Minnesota. *Neurology*, 76(1):23–27, 2010. 1

[2] Cleusa P. Ferri, Martin Prince, Carol Brayne, Henry Brodaty, Laura Fratiglioni, Mary Ganguli, Kathleen Hall, Kazuo Hasegawa, Hugh Hendrie, Yueqin Huang, Anthony Jorm, Colin Mathers, Paulo R. Menezes, Elizabeth Rimmer, and Marcia Scazufca. Global prevalence of dementia: A Delphi consensus study. *Lancet*, 366:2112–2117, 2005. 1

[3] Peter J. Uhlhaas and Wolf Singer. Neural Synchrony in Brain Disorders: Relevance for Cognitive Dysfunctions and Pathophysiology. *Neuron*, 52:155–168, 2006. 1

[4] Frederico a C Azevedo, Ludmila R B Carvalho, Lea T. Grinberg, José Marcelo Farfel, Renata E L Ferretti, Renata E P Leite, Wilson Jacob Filho, Roberto Lent, and Suzana Herculano-Houzel. Equal numbers of neuronal and nonneuronal cells make the human brain an isometrically scaled-up primate brain. *Journal of Comparative Neurology*, 513(5):532–541, 2009. 1

[5] Marta Sidoryk-Wegrzynowicz, Michal Wegrzynowicz, Eunsook Lee, Aaron B Bowman, and Michael Aschner. Role of astrocytes in brain function and disease. *Toxicologic pathology*, 39:115–123, 2011. 1

[6] Helmut Kettenmann, Frank Kirchhoff, and Alexei Verkhratsky. Microglia: new roles for the synaptic stripper. *Neuron*, 77(1):10–18, 2013. 1

[7] N Baumann and D Pham-Dinh. Biology of oligodendrocyte and myelin in the mammalian central nervous system. *Physiological reviews*, 81(2):871–927, 2001. 1

[8] Premysl Jiruska, Marco de Curtis, John G R Jefferys, Catherine A Schevon, Steven J Schiff, and Kaspar Schindler. Synchronization and desynchronization in epilepsy: controversies and hypotheses. *Journal of Physiology-London*, 591(4):787–797, 2013. 1

[9] George Bartzokis. Age-related myelin breakdown: A developmental model of cognitive decline and Alzheimer's disease. *Neurobiology of Aging*, 25(1):5–18, 2004. 1

[10] a. M L Coenen and E. L J M Van Luijtelaar. Genetic Animal Models for Absence Epilepsy: A Review of the WAG/Rij Strain of Rats. *Behavior Genetics*, 33(6):635–655, 2003. 1

[11] Galit Pelled, Hagai Bergman, and Gadi Goelman. Bilateral overactivation of the sensorimotor cortex in the unilateral rodent model of Parkinson's disease - a functional magnetic resonance imaging study. *The European journal of neuroscience*, 15(2):389–394, 2002. 1

[12] Amir M. Ghaemmaghami, Matthew J. Hancock, Helen Harrington, Hirokazu Kaji, and Ali Khademhosseini. Biomimetic tissues on a chip for drug discovery. *Drug Discovery Today*, 17(3-4):173–181, 2012. 1

[13] W Loscher and Wolfgang Löscher. Critical review of current animal models of seizures and epilepsy used in the discovery and development of new antiepileptic drugs. *Seizure*, 20(5):359–368, 2011. 1

[14] Steve Perrin. Make mouse studies work. *Nature*, 507:423, 2014. 1

[15] Nicolas Daviaud, Elisa Garbayo, Paul C. Schiller, Miguel Perez-Pinzon, and Claudia N. Montero-Menei. Organotypic cultures as tools for optimizing central nervous system cell therapies. *Experimental neurology*, 248:429–40, 2013. 1

[16] Michael Wong. Epilepsy in a dish: An in vitro model of epileptogenesis. *Epilepsy Currents*, 11(5):153–154, 2011. 1

[17] Shreyas S Rao, John J Lannutti, Mariano S Viapiano, Atom Sarkar, and Jessica O Winter. Toward 3D Biomimetic Models to Understand the Behavior of Glioblastoma Multiforme Cells. *Tissue engineering. Part B, Reviews*, 00(4):314–327, 2013. 2

[18] G Xiang, L Pan, L Huang, Z Yu, X Song, J Cheng, W Xing, and Y Zhou. Microelectrode array-based system for neuropharmacological applications with cortical neurons cultured in vitro. *Biosens Bioelectron*, 22(11):2478–2484, 2007. 2

[19] Tobias Führmann, Lisa M. Hillen, Katrin Montzka, Michael Wöltje, and Gary a. Brook. Cell-Cell interactions of human neural progenitor-derived astrocytes within a microstructured 3D-scaffold. *Biomaterials*, 31(30):7705–7715, 2010. 2

[20] Alex L. Kolodkin and Marc Tessier-Lavigne. Mechanisms and molecules of neuronal wiring: A primer. *Cold Spring Harbor Perspectives in Biology*, 3(6):1–14, 2011. 2

[21] Jean-Philippe Frimat, Julia Sisnaiske, Subanatarajan Subbiah, Heike Menne, Patricio Godoy, Peter Lampen, Marcel Leist, Joachim Franzke, Jan G Hengstler, Christoph van Thriel, and Jonathan West. The network formation assay: a spatially standardized neurite outgrowth analytical display for neurotoxicity screening. *Lab on a chip*, 10(6):701–709, 2010. 2

[22] B M Baker and C S Chen. Deconstructing the third dimension: how 3D culture microenvironments alter cellular cues. *J Cell Sci*, 125(13):3015–3024, 2012. 2

[23] Grace N Li, Liane L Livi, Celinda M Gourd, Elizabeth S Deweerd, and Diane Hoffman-Kim. Genomic and morphological changes of neuroblastoma cells in response to three-dimensional matrices. *Tissue engineering*, 13(5):1035–1047, 2007. 2

[24] Monica Frega, Mariateresa Tedesco, Paolo Massobrio, Mattia Pesce, and Sergio Martinoia. Network dynamics of 3D engineered neuronal cultures: a new experimental model for in-vitro electrophysiology. *Scientific reports*, 4:5489, 2014. 2

[25] Tania Limongi, Fabrizia Cesca, Francesco Gentile, Roberto Marotta, Roberta Ruffilli, Andrea Barberis, Marco Dal Maschio, Enrica Maria Petrini, Stefania Santoriello, Fabio Benfenati, and Enzo Di Fabrizio. Nanostructured Superhydrophobic Substrates Trigger the Development of 3D Neuronal Networks. *Small*, 9(3):402–412, 2013. 2

[26] Susanna Bosi, Rossana Rauti, Jummi Laishram, Antonio Turco, Davide Lonardoni, Thierry Nieus, Maurizio Prato, Denis Scaini, and Laura Ballerini. From 2D to 3D: novel nanostructured scaffolds to investigate signalling in reconstructed neuronal networks. *Scientific Reports*, 5:9562, 2015. 2

[27] Jae Myung Jang, Si-Hoai-Trung Tran, Sang Cheol Na, and Noo Li Jeon. Engineering Controllable Architecture in Matrigel for 3D Cell Alignment. *ACS Applied Materials & Interfaces*, 7(4):2183–2188, 2015. 2

[28] Renee M Huval, Oliver H Miller, Jabe Lowry Curley, Yuwei Fan, Benjamin J Hall, and Michael Moore. Microengineered Peripheral Nerve-on-a-Chip for Preclinical Physiological Testing. *Lab Chip*, 15:2221–2232, 2015. 2

[29] Min Kyung Lee, Max H. Rich, Jonghwi Lee, and Hyunjoon Kong. A bio-inspired, microchanneled hydrogel with controlled spacing of cell adhesion ligands regulates 3D spatial organization of cells andtissue. *Biomaterials*, 58:26–34, 2015. 2

[30] Andries D. Van Der Meer and Albert Van Den Berg. Organs-on-chips: breaking the in vitro impasse. *Integrative Biology*, 4(5):461, 2012. 2

[31] Bart Schurink and Regina Luttge. Hydrogel/poly-dimethylsiloxane hybrid bioreactor facilitating 3D cell culturing. *Journal of Vacuum Science & Technology B*, 31(6):06F903, 2013. 3

[32] Jean-Philippe Frimat, Sijia Xie, Alex Bastiaens, Bart Schurink, Floor Wolbers, Jaap den Toonder, and Regina Luttge. Advances in 3D neuronal cell culture. *Journal of Vacuum Science & Technology B, Nanotechnology and Microelectronics: Materials, Processing, Measurement, and Phenomena*, 33(6):06F902, 2015. 3, 15

[33] Susan Dwane, Edel Durack, and Patrick a Kiely. Optimising parameters for the differentiation of SH-SY5Y cells to study cell adhesion and cell migration. *BMC research notes*, 6(1):366, 2013. 3, 46

[34] Marcus Innala, Ilse Riebe, Volodymyr Kuzmenko, Johan Sundberg, Paul Gatenholm, Eric Hanse, and Sara Johannesson. 3D culturing and differentiation of SH-SY5Y neuroblastoma cells on bacterial nanocellulose scaffolds. *Artificial Cells, Nanomedicine, and Biotechnology*, 42(5):302–308, 2014. 3

[35] Corning Matrigel Matrix, Frequently Asked Questions. Technical report, Corning, 2012. 4, 18, 24, 47, 53

[36] M U Kopp, a J Mello, and A Manz. Chemical amplification: continuous-flow PCR on a chip. *Science*, 280(5366):1046–1048, 1998. 5, 13

[37] Jing Cheng, Mann a. Shoffner, Georgi E. Hvichia, Larry J. Kricka, and Peter Wilding. Chip PCR. II. Investigation of different PCR amplification systems in microfabricated silicon-glass chips. *Nucleic Acids Research*, 24(2):380–385, 1996. 5

[38] Fiona M F Lun, Rossa W K Chiu, K. C Allen Chan, Yeung Leung Tak, Kin Lau Tze, and Y. M Dennis Lo. Microfluidics digital PCR reveals a higher than expected fraction of fetal DNA in maternal plasma. *Clinical Chemistry*, 54(10):1664–1672, 2008. 5, 14

[39] Ali Fallah-Araghi, Jean-Christophe Baret, Michael Ryckelynck, and Andrew D. Griffiths. A completely in vitro ultrahigh-throughput droplet-based microfluidic screening system for protein engineering and directed evolution. *Lab on a Chip*, 12(5):882, 2012. 5

[40] Jeremy J Agresti, Eugene Antipov, Adam R Abate, Keunho Ahn, Amy C Rowat, Jean-Christophe Baret, Manuel Marquez, Alexander M Klibanov, Andrew D Griffiths, and David a Weitz. Ultrahigh-throughput screening in drop-based microfluidics for directed evolution. *Proceedings of the National Academy of Sciences of the United States of America*, 107(9):4004–4009, 2010. 5

[41] James a. Stapleton and James R. Swartz. Development of an in vitro compartmentalization screen for high-throughput directed evolution of [FeFe] hydrogenases. *PLoS ONE*, 5(12):1–8, 2010. 5

[42] Ye Jin Eun, Andrew S. Utada, Matthew F. Copeland, Shoji Takeuchi, and Douglas B. Weibel. Encapsulating bacteria in agarose microparticles using microfluidics for high-throughput cell analysis and isolation. *ACS Chemical Biology*, 6(3):260–266, 2011. 5, 10, 11, 44, 62

[43] B. E. Debs, R. Utharala, I. V. Balyasnikova, a. D. Griffiths, and C. a. Merten. Functional single-cell hybridoma screening using droplet-based microfluidics. *Proceedings of the National Academy of Sciences*, 109:11570–11575, 2012. 5, 10, 11

[44] Ramesh Ramji, Ming Wang, Ali Asgar S Bhagat, Daniel Tan Shao Weng, Nitish V Thakor, Chwee Teck Lim, and Chia-Hung Chen. Single cell kinase signaling assay using pinched flow coupled droplet microfluidics. *Biomicrofluidics*, 8:034104, 2014. 5, 11, 13, 44, 61

[45] Bong Geun Chung, Kwang-Ho Lee, Ali Khademhosseini, and Sang-Hoon Lee. Microfluidic fabrication of microengineered hydrogels and their application in tissue engineering. *Lab on a Chip*, 12:45, 2012. 5

[46] Ali Khademhosseini and Geun Chung Bong. Microscale technologies for tissue engineering. *2009 IEEE/NIH Life Science Systems and Applications Workshop, LiSSA 2009*, 103(8):56–57, 2009. 5

[47] David J Beebe, Glennys a Mensing, and Glenn M Walker. Physics and applications of microfluidics in biology. *Annual review of biomedical engineering*, 4:261–286, 2002. 6

[48] Todd M Squires and Stephen R. Quake. Microfluidics Fluid physics at the nanoliter. 77(July), 2005. 6

[49] Frank M. White. *Viscous fluid flow*. McGraw Hill, 2nd. edition, 1991. 6

[50] Shia-Yen Teh, Robert Lin, Lung-Hsin Hung, and Abraham P Lee. Droplet microfluidics. *Lab on a chip*, 8:198–220, 2008. 8

[51] G F Christopher and S L Anna. Microfluidic methods for generating continuous droplet streams. *Journal of Physics D: Applied Physics*, 40(19):R319–R336, 2007. 8, 9

[52] Ralf Seemann, Martin Brinkmann, Thomas Pfohl, and Stephan Herminghaus. Droplet based microfluidics. *Reports on Progress in Physics*, 75(1):016601, 2011. 8

[53] Shelley L. Anna, Nathalie Bontoux, and Howard A. Stone. Formation of dispersions using ”flow focusing” in microchannels. *Applied Physics Letters*, 82(3):364–366, 2003. 8

[54] Shelley L. Anna and Hans C. Mayer. Microscale tipstreaming in a microfluidic flow focusing device. *Physics of Fluids*, 18(12):121512, 2006. 9

[55] Andrew S. Utada, Alberto Fernandez-Nieves, Howard A. Stone, and David A. Weitz. Dripping to Jetting Transitions in Coflowing Liquid Streams. *Physical Review Letters*, 99(9):094502, 2007. 9

[56] Thomas Ward, Magalie Faivre, Manouk Abkarian, and Howard a. Stone. Microfluidic flow focusing: Drop size and scaling in pressure versus flow-rate-driven pumping. *Electrophoresis*, 26(19):3716–3724, 2005. 10, 16

[57] Eric Brouzes, Martina Medkova, Neal Savenelli, Dave Marran, Mariusz Twardowski, J Brian Hutchison, Jonathan M Rothberg, Darren R Link, Norbert Perrimon, and Michael L Samuels. Droplet microfluidic technology for single-cell high-throughput screening. *Proceedings of the National Academy of Sciences of the United States of America*, 106:14195–14200, 2009. 10, 11

[58] Jean-Christophe Baret. Surfactants in droplet-based microfluidics. *Lab on a Chip*, 12(2001):422, 2012. 10

[59] Jenifer Clausell-Tormos, Diana Lieber, Jean Christophe Baret, Abdeslam El-Harrak, Oliver J. Miller, Lucas Frenz, Joshua Blouwolff, Katherine J. Humphry, Sarah Köster, Honey Duan, Christian Holtze, David a. Weitz, Andrew D. Griffiths, and Christoph a. Merten. Droplet-Based Microfluidic Platforms for the Encapsulation and Screening of Mammalian Cells and Multicellular Organisms. *Chemistry and Biology*, 15(May):427–437, 2008. 10, 11, 39

[60] Choong Kim, Kang Sun Lee, Young Eun Kim, Kyu-Jung Lee, Soo Hyun Lee, Tae Song Kim, and Ji Yoon Kang. Rapid exchange of oil-phase in microencapsulation chip to enhance cell viability. *Lab on a chip*, 9(9):1294–1297, 2009. 10, 11, 40, 61

[61] Choong Kim, Seok Chung, Young Eun Kim, Kang Sun Lee, Soo Hyun Lee, Kwang Wook Oh, and Ji Yoon Kang. Generation of core-shell microcapsules with three-dimensional focusing device for efficient formation of cell spheroid. *Lab on a chip*, 11(2):246–252, 2011. 10, 11

[62] Samin Akbari and Tohid Pirbodaghi. Microfluidic encapsulation of cells in alginate particles via an improved internal gelation approach. *Microfluidics and Nanofluidics*, pages 1–5, 2013. 10, 11, 57

[63] Liang Wu, Pu Chen, Yingsong Dong, Xiaojun Feng, and Bi Feng Liu. Encapsulation of single cells on a microfluidic device integrating droplet generation with fluorescence-activated droplet sorting. *Biomedical Microdevices*, 15(3):553–560, 2013. 10, 11, 13, 44, 62

[64] Wei Heong Tan and Shoji Takeuchi. Monodisperse alginate hydrogel microbeads for cell encapsulation. *Advanced Materials*, 19:2696–2701, 2007. 10, 11

[65] Chang Hyung Choi, Jae Hoon Jung, Young Woo Rhee, Dong Pyo Kim, Sang Eun Shim, and Chang Soo Lee. Generation of monodisperse alginate microbeads and in situ encapsulation of cell in microfluidic device. *Biomedical Microdevices*, 9(6):855–862, 2007. 10, 11, 39

[66] Eujin Um, Dae Sik Lee, Hyeon Bong Pyo, and Je Kyun Park. Continuous generation of hydrogel beads and encapsulation of biological materials using a microfluidic droplet-merging channel. *Microfluidics and Nanofluidics*, 5(4):541–549, 2008. 10, 11

[67] Alexander Kumachev, Jesse Greener, Ethan Tumarkin, Erika Eiser, Peter W. Zandstra, and Eugenia Kumacheva. High-throughput generation of hydrogel microbeads with varying elasticity for cell encapsulation. *Biomaterials*, 32(6):1477–1483, 2011. 10, 11

[68] Rong Fan, Kubra Naqvi, Krishna Patel, Jun Sun, and Jiandi Wan. Evaporation-based microfluidic production of oil-free cell-containing hydrogel particles. *Biomicrofluidics*, 9:052602, 2015. 10, 11, 45, 47, 48

[69] Torsten Rossow, John a. Heyman, Allen J. Ehrlicher, Arne Langhoff, David a. Weitz, Rainer Haag, and Sebastian Seiffert. Controlled synthesis of cell-laden microgels by radical-free gelation in droplet microfluidics. *Journal of the American Chemical Society*, 134(10):4983–4989, 2012. 10, 11, 57

[70] Monika E. Dolega, Fabien Abeille, Nathalie Picollet-D'hahan, and Xavier Gidrol. Controlled 3D culture in Matrigel microbeads to analyze clonal acinar development. *Biomaterials*, 52:347–357, 2015. 10, 11, 13, 46

[71] Jon F Edd, Dino Di Carlo, Katherine J Humphry, Sarah Köster, Daniel Irimia, David a Weitz, and Mehmet Toner. Controlled encapsulation of single-cells into monodisperse picolitre drops. *Lab on a chip*, 8:1262–1264, 2008. 11, 13, 44, 62

[72] Max Chabert and Jean-Louis Viovy. Microfluidic high-throughput encapsulation and hydrodynamic self-sorting of single cells. *Proceedings of the National Academy of Sciences of the United States of America*, 105:3191–3196, 2008. 11, 13

[73] Sarah Köster, Francesco E Angilè, Honey Duan, Jeremy J Agresti, Anton Wintner, Christian Schmitz, Amy C Rowat, Christoph a Merten, Dario Pisignano, Andrew D Griffiths, and David a Weitz. Drop-based microfluidic devices for encapsulation of single cells. *Lab on a chip*, 8(7):1110–1115, 2008. 11, 12

[74] Mingyan He, J. Scott Edgar, Gavin D M Jeffries, Robert M. Lorenz, J. Patrick Shelby, and Daniel T. Chiu. Selective encapsulation of single cells and subcellular organelles into picoliter- and femtoliter-volume droplets. *Analytical Chemistry*, 77(6):1539–1544, 2005. 11, 13

[75] Todd P Lagus and Jon F Edd. A review of the theory, methods and recent applications of high-throughput single-cell droplet microfluidics. *Journal of Physics D: Applied Physics*, 46:114005, 2013. 12

[76] Evelien W. M. Kemna, Rogier M. Schoeman, Floor Wolbers, Istvan Vermes, David a. Weitz, and Albert van den Berg. High-yield cell ordering and deterministic cell-in-droplet encapsulation using Dean flow in a curved microchannel. *Lab on a Chip*, 12(16):2881, 2012. 13, 44, 62

[77] Chunsun Zhang, Jinliang Xu, Wenli Ma, and Wenling Zheng. PCR microfluidic devices for DNA amplification. *Biotechnology Advances*, 24(3):243–284, 2006. 13

[78] Philippe Laval, Nicolas Lisai, Jean-Baptiste Salmon, and Mathieu Joanicot. A microfluidic device based on droplet storage for screening solubility diagrams. *Lab on a Chip*, 7(7):829, 2007. 13

[79] Takuya Matsui, Joachim Franzke, Andreas Manz, and Dirk Janasek. Temperature gradient focusing in a PDMS/glass hybrid microfluidic chip. *Electrophoresis*, 28(24):4606–4611, 2007. 13, 14

[80] Vincent Miralles, Axel Huerre, Florent Malloggi, and Marie-Caroline Jullien. *A Review of Heating and Temperature Control in Microfluidic Systems: Techniques and Applications*, volume 3. 2013. 13

[81] George Maltezos, Matthew Johnston, and Axel Scherer. Thermal management in microfluidics using micro-Peltier junctions. *Applied Physics Letters*, 87(15):154105, 2005. 13

[82] George Maltezos, Alvaro Gomez, Jiang Zhong, Frank a. Gomez, and Axel Scherer. Microfluidic polymerase chain reaction. *Applied Physics Letters*, 93(24):243901, 2008. 13

[83] Aj de Mello, M Habgood, Nl Lancaster, T Welton, and Rcr Wootton. Precise temperature control in microfluidic devices using Joule heating of ionic liquids. pages 417–419, 2004. 13

[84] E. Mavraki, D. Moschou, G. Kokkoris, N. Vourdas, S. Chatzandroulis, and a. Tserepi. A continuous flow μPCR device with integrated microheaters on a flexible polyimide substrate. *Procedia Engineering*, 25:1245–1248, 2011. 13

[85] Jerome P Ferrance, Qirong Wu, Braden Giordano, Casandra Hernandez, Yien Kwok, Karen Snow, Steve Thibodeau, and James P Landers. Developments toward a complete micro-total analysis system for Duchenne muscular dystrophy diagnosis. *Analytica Chimica Acta*, 500(1-2):223–236, 2003. 13

[86] B.C. Giordano, J. Ferrance, S. Swedberg, a.F.R. Hühmer, and J.P. Landers. Polymerase Chain Reaction in Polymeric Microchips: DNA Amplification in Less Than 240 Seconds. *Analytical Biochemistry*, 291(1):124–132, 2001. 13

[87] George Maltezos, Aditya Rajagopal, and Axel Scherer. Evaporative cooling in microfluidic channels. *Applied Physics Letters*, 89(7):074107, 2006. 13

[88] Rosanne M. Guijt, Arash Dodge, Gijs W. K. van Dedem, Nico F. de Rooij, and Elisabeth Verpoorte. Chemical and physical processes for integrated temperature control in microfluidic devices. *Lab on a Chip*, 3(1):1, 2003. 13

[89] Hanyoup Kim, Siarhei Vishniakou, and Gregory W. Faris. Petri dish PCR: laser-heated reactions in nanoliter droplet arrays. *Lab on a Chip*, 9(9):1230, 2009. 13

[90] Jinbo Wu, Wenbin Cao, Weijia Wen, Donald Choy Chang, and Ping Sheng. Polydimethylsiloxane microfluidic chip with integrated microheater and thermal sensor. *Biomicrofluidics*, 3(1):012005, 2009. 13

[91] Shih-Hao Huang, Yi-Syun Lin, Chih-Wei Wu, and Chang-Jer Wu. Assessment of the inhibition of Dengue virus infection by carrageenan via real-time monitoring of cellular oxygen consumption rates within a microfluidic device. *Biomicrofluidics*, 8(2):024110, 2014. 13

[92] M. D. C. Lopez-Garcia, R. L. Monson, K. Haubert, M. B. Wheeler, and D. J. Beebe. Sperm motion in a microfluidic fertilization device. *Biomedical Microdevices*, 10(5):709–718, 2008. 13

[93] Margaret Macris Kiss, Lori Ortoleva-Donnelly, N. Reginald Beer, Jason Warner, Christopher G. Bailey, Bill W. Colston, Jonathon M. Rothberg, Darren R. Link, and John H. Leamon. High-Throughput Quantitative Polymerase Chain Reaction in Picoliter Droplets. *Analytical Chemistry*, 80(23):8975–8981, 2008. 13

[94] Julia Khandurina, Timothy E. McKnight, Stephen C. Jacobson, Larry C. Waters, Robert S. Foote, and J. Michael Ramsey. Integrated System for Rapid PCR-Based DNA Analysis in Microfluidic Devices. *Analytical Chemistry*, 72(13):2995–3000, 2000. 14, 18

[95] Jianing Yang, Yingjie Liu, Cory B. Rauch, Randall L. Stevens, Robin H. Liu, Ralf Lenigk, and Piotr Grodzinski. High sensitivity PCR assay in plastic micro reactors. *Lab on a Chip*, 2(4):179, 2002. 14

[96] Guilhem Velve Casquillas, Chuanhai Fu, Mael Le Berre, Jeremy Cramer, Sebastien Meance, Adrien Plecis, Damien Baigl, Jean-Jacques Greffet, Yong Chen, Matthieu Piel, and Phong T. Tran. Fast microfluidic temperature control for high resolution live cell imaging. *Lab Chip*, 11(3):484–489, 2011. 14

[97] Hanbin Mao, Tinglu Yang, and Paul S. Cremer. A microfluidic device with a linear temperature gradient for parallel and combinatorial measurements. *Journal of the American Chemical Society*, 124(16):4432–4435, 2002. 14

[98] Jeffrey D Winterton, David R. Myers, Julian M. Lippmann, Albert P. Pisano, and Fiona M. Doyle. A novel continuous microfluidic reactor design for the controlled production of high-quality semiconductor nanocrystals. *Journal of Nanoparticle Research*, 10(6):893–905, 2008. 14

[99] Theodore L. Bergman, Adrienne S. Lavine, David P. Dewitt, and Frank P Incropera. *Fundamentals of Heat and Mass Transfer*. John Wiley & Sons., 7th edition, 2011. 19

[100] a. S. Varadarajan, P. K. Philip, and B. Ramamoorthy. Investigations on hard turning with minimal cutting fluid application (HTMF) and its comparison with dry and wet turning. *International Journal of Machine Tools and Manufacture*, 42(2):193–200, 2002. 19

[101] R Larsson, P O Larsson, E Eriksson, M Sjöberg, and E Höglund. Lubricant properties for input to hydrodynamic and elastohydrodynamic lubrication analyses. *Proceedings of the Institution of Mechanical Engineers, Part J: Journal of Engineering Tribology*, 214(July 1999):17–27, 2000. 19

[102] David Erickson, David Sinton, and Dongqing Li. Joule heating and heat transfer in poly(dimethylsiloxane) microfluidic systems. *Lab on a Chip*, 3(3):141, 2003. 19

[103] Christine C. Roberts, Rekha R. Rao, Michael Loewenberg, Carlton F. Brooks, Paul Galambos, Anne M. Grillet, and Martin B. Nemer. Comparison of monodisperse droplet generation in flow-focusing devices with hydrophilic and hydrophobic surfaces. *Lab on a Chip*, 12(8):1540, 2012. 32

[104] Michael J. Fuerstman, Ann Lai, Meghan E. Thurlow, Sergey S. Shevkoplyas, Howard a. Stone, and George M. Whitesides. The pressure drop along rectangular microchannels containing bubbles. *Lab on a Chip*, 7(11):1479, 2007. 37

[105] Kosuke Iwai, E Yegan Erdem, Ryan D Sochol, Jim C Cheng, Fiona M Doyle, Albert P Pisano, and Liwei Lin. Microdroplet-based synthesis and centrifuge-free retrieval of nanoparticles via a continuous flow micropost array railing system. In *Solid-State Sensors, Actuators and Microsystems (TRANSDUCERS & EUROSENSORS XXVII), 2013 Transducers & Eurosensors XXVII: The 17th International Conference on*, pages 2656–2659. IEEE, 2013. 39, 40, 61

[106] Kyun Joo Park, Kyoung G Lee, Seunghwan Seok, Bong Gill Choi, Moon-keun Lee, Tae Jung Park, Seok Jae Lee, and Do Hyun Kim. Microbial Single Cell Encapsulation in Hydrogel Through Enhanced Cell Dispersion By Micropillar. pages 427–429, 2014. 44, 61

[107] Choong Kim. Droplet-based microfluidics for making uniform-sized cellular spheroids in alginate beads with the regulation of encapsulated cell number. *BioChip Journal*, 9(2):105–113, 2015. 44, 61

[108] Adam R Abate, Chia-Hung Chen, Jeremy J Agresti, and David a Weitz. Beating Poisson encapsulation statistics using close-packed ordering. *Lab on a chip*, 9(May):2628–2631, 2009. 44, 61

[109] Mario Encinas, Montse Iglesias, Yuhui Liu, Hongyin Wang, Ashraf Muhaisen, Valentin Ceña, Carme Gallego, and Joan X. Comella. Sequential treatment of SH-SY5Y cells with retinoic acid and brain-derived neurotrophic factor gives rise to fully differentiated, neurotrophic factor-dependent, human neuron-like cells. *Journal of Neurochemistry*, 75:991–1003, 2000. 46

[110] Andrew C Hatch, Jeffrey S Fisher, Stephen L Pentoney, David L Yang, and Abraham P Lee. Tunable 3D droplet self-assembly for ultra-high-density digital micro-reactor arrays. *Lab on a chip*, 11(111):2509–2517, 2011. 56

[111] NTC Interchangeable Type 95 Series - Thermometrics Thermistors. Technical report, Amphenol Advanced Sensors, 2015. 74

[112] Sensor Temperature Resistance Curves - reference guide, rev. C. Technical Report November, Amphenol Advanced Sensors, St. Marys, PA, 2014. 74

Appendix A

COMSOL simulations of heat transfer and flow

A simulation model was built in COMSOL to evaluate the temperature distribution throughout the encapsulation device as a function of the cooling and heating water flow-rate. In this model, three different types of physics were integrated in the simulation: incompressible laminar flow, heat conduction in solids, and heat conduction in liquids. Laminar flow was assumed because the Reynolds number did not exceed 2300 for any of the simulated flow-rates. Only the steady-state solution was computed.

The solid part of the 3D simulation model consisted of three parts: a model of the temperature chambers, a model of the glass slide, and a model of the PDMS layer (Figure A.1). The temperature chambers were modeled as a single piece of PMMA, in which the chambers were formed by two cavities, neglecting the influence of the silicone sealant. The PDMS chip was modeled as a single slab assumed to be 4 mm thick, neglecting the influence of the microchannel geometry. The material properties of the simulated materials can be found in table A.1.

A natural convection boundary condition was applied to the outer surfaces of the device, assuming the surrounding air had a temperature of 20°C. This was implemented separately for the top, side, and bottom surfaces, such that the different modes of natural convection were taken into account.

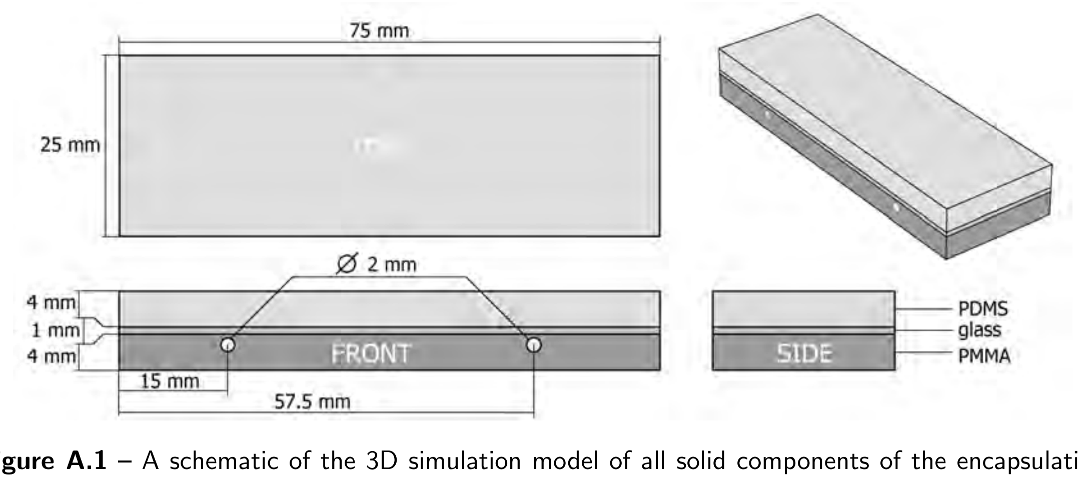

Figure A.1 – A schematic of the 3D simulation model of all solid components of the encapsulation device.

Table A.1 – Material properties of PDMS, glass, and PMMA in COMSOL

Material	Density [kg/m^3]	Heat capacity [J/kgK]	Thermal conductivity [W/mK]
PDMS	970	1460	0.16
glass	2203	703	1.05
PMMA	1190	1470	0.18

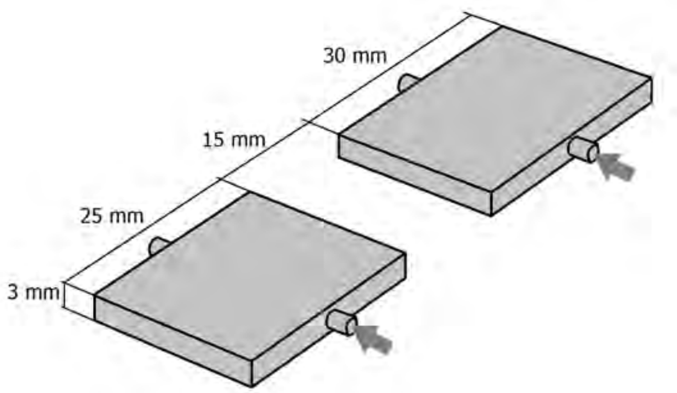

Figure A.2 – A schematic of the 3D simulation model of the fluid inside the temperature chambers of the encapsulation device. The arrows indicate where the water inlet is modeled. The outlets are on the other side of both chambers.

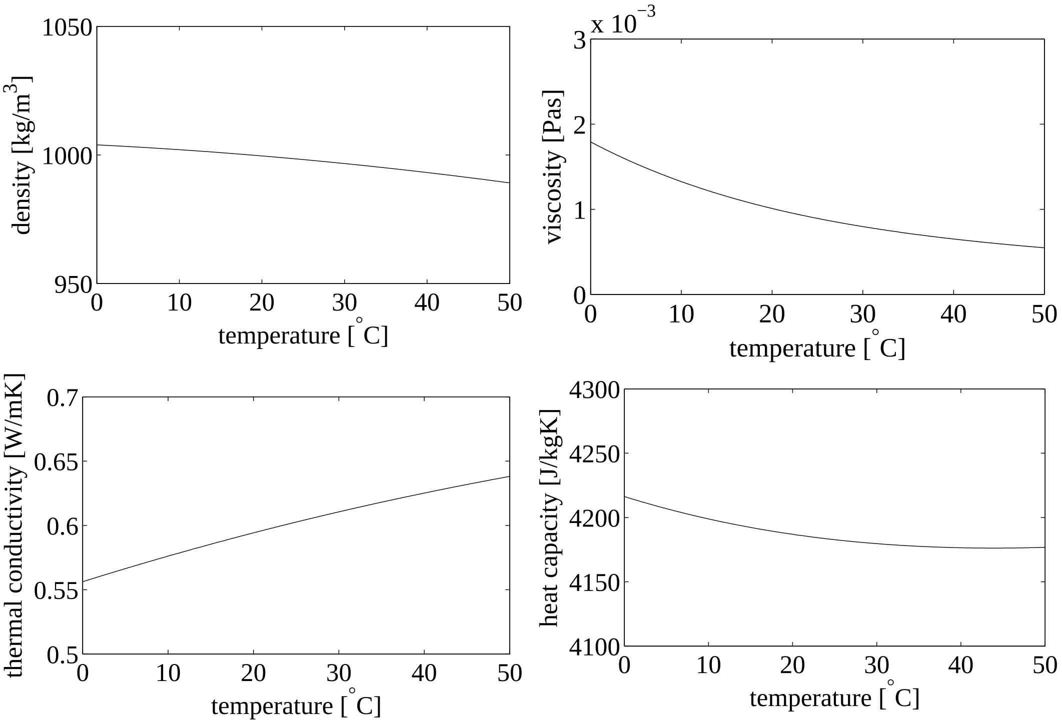

Figure A.3 – The physical properties of water in the COMSOL library, including the density, viscosity, thermal conductivity, and heat capacity as a function of temperature.

Inside the cavities of the solid part of the model, the heating and cooling fluid was modeled as well. The liquid model of the 3D simulation model consisted of two parts, representing the two temperature chambers (Figure A.2). The material was defined as water from the COMSOL library, in which the density, viscosity, thermal conductivity, and heat capacity were a function of temperature (Figure A.3).

At the inlets, a fixed flow-rate was prescribed, assuming fully developed flow. Here, the water temperature was set to a fixed value of 0°C at the inlet of the cold chamber, and 50°C at the inlet of the hot chamber. At the outlets, the pressure was set to atmospheric pressure. All other boundaries were modeled as solid boundaries on which a no-slip boundary condition was applied.

Appendix B

Arduino controlled temperature sensors

An array of temperature sensors was built to quantify a thermal gradient across a surface, that ranges from 0°C to 50 °C. The array consists of 5 independent thermistors coupled to an Arduino UNO board, which measures the resistance of each sensor and converts it to a temperature in Celsius. In this appendix, the properties of the used thermistors, the Arduino interface, and Matlab data logging code are presented.

Thermistor properties

In order to be able to measure the temperature range, thermistors with a negative temperature coefficient (NTC) are used (Amphenol Advanced Sensors, DC95F502W). This sensor type has an accuracy of ±0.2°C over a range between 0°C to 70 °C [111], and the relation between the NTC electrical resistance and their temperature is known (see equation B.1) [112].

$$T = \left[a + b \cdot ln\left(\frac{R_t}{R_{25}}\right) + c \cdot ln\left(\frac{R_t}{R_{25}}\right)^2 + d \cdot ln\left(\frac{R_t}{R_{25}}\right)^3\right]^{-1} \tag{B.1}$$

In this equation, T is the temperature in Kelvin, R_t the electrical resistance of the NTC in Ohm, and $R_2 5$ the electrical resistance of the NTC at 25°C, which is 5kΩ for this model. The values for constants a, b, c, and d are found in Table B.1.

Table B.1 – Sensor constants for DC95F502W thermistor

Constant	Value
a	$3.3540154 \cdot 10^{-3}$
b	$2.5627725 \cdot 10^{-4}$
c	$2.0829210 \cdot 10^{-6}$
d	$7.3003206 \cdot 10^{-8}$

Arduino wiring and code

In order to measure the resistance of an NTC, a voltage divider is used for each of the 5 sensors (Figure B.1). The Arduino board has 5 separate analog input ports (A0-A4), that are used to measure the output potential of each voltage divider. In this configuration, the resistance of the NTCs can be computed as a function of the voltage measured at the analog ports A_0-A_4, through equation B.2, where $R_{2,4,...}$ is the resistance of the NTC, $R_{1,3,...}$ the resistance of the static resistor, and $V_{A_{0,1,...}}$ the voltage measured in the analog port on the Arduino.

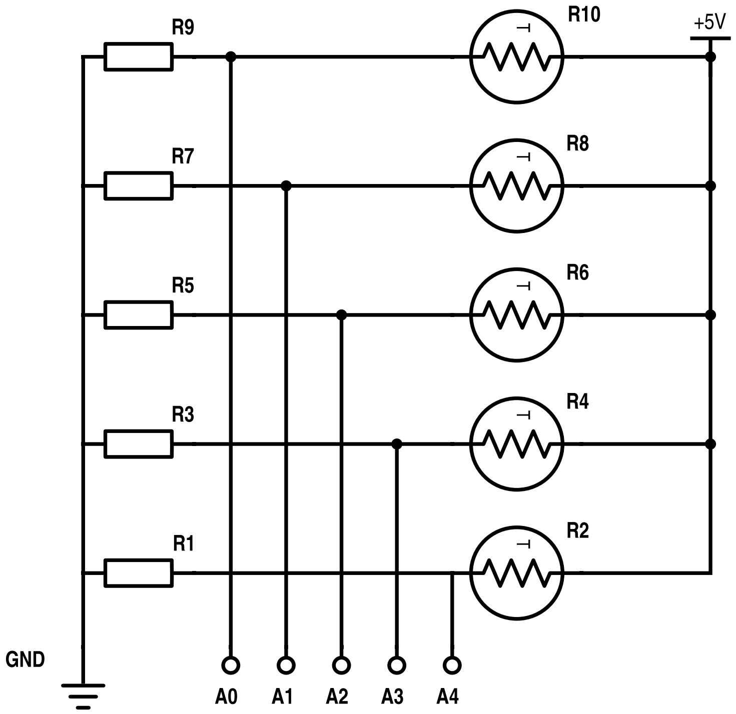

Figure B.1 – Wiring scheme of the parallel voltage dividers for the NTCs. R1 ,R3 ,R5 ,R7, and R9 have a resistance of $4.7\text{k}\Omega$, R2 ,R4 ,R6 ,R8, and R10 are the variable resistances of the NTCs, and A0-A4 correspond to the analog ports on the Arduino board.

$$R_{2,4,\ldots} = R_{1,3,\ldots} \cdot \left(\frac{5}{V_{A_{0,1,\ldots}}} - 1 \right) \tag{B.2}$$

The calculation of the temperature as measured by the individual NTCs takes place locally on the Arduino board, based on equations B.1 and B.2. The Arduino performs the computations and sends the measured temperature to a serial port each 0.5 second. The complete code used for this purpose is shown in below.

```
// File: Temperature_measurement.ino

void setup() {
Serial.begin(9600); // open serial port and set data rate to 9600 bps
Serial.println("Thermistor measurement:");
Serial.println("\n time T0 T1 T2 T3 T4");
}

// -- loop() is repeated indefinitely
void loop(){
int Thermistor0 = A0; // Analog input pin 0 for thermistor voltage
int Thermistor1 = A1; // Analog input pin 1 for thermistor voltage
int Thermistor2 = A2; // Analog input pin 2 for thermistor voltage
int Thermistor3 = A3; // Analog input pin 3 for thermistor voltage
int Thermistor4 = A4; // Analog input pin 4 for thermistor voltage
float R0 = 4700.0; // Fixed resistance in voltage divider 0
float R1 = 4700.0; // Fixed resistance in voltage divider 1
```

```
float R2 = 4700.0; // Fixed resistance in voltage divider 2
float R3 = 4700.0; // Fixed resistance in voltage divider 3
float R4 = 4700.0; // Fixed resistance in voltage divider 4
float R25 = 5000.0; // NTC Resistance at 25 degrees
float logRt_R25,Rt; // Float variables for temporary storage
int Vo; // Integer variable of voltage reading
float T0,T1,T2,T3,T4; // Float variables for temperature readings

// constants for Volt-Kelvin conversion
float c1 = 3.3540154E-03, c2 = 2.5627725E-04, c3 = 2.0829210E-06, c4 =
7.3003206E-08;

// Computing temperature of sensor 1
Vo = analogRead(Thermistor0);
Rt = R0*( 1023.0 / float(Vo) - 1.0 );
logRt_R25 = log(Rt/R25);
T0 = ( 1.0 / (c1 + c2 * logRt_R25 + c3 * logRt_R25 * logRt_R25 + c4 *
logRt_R25 * logRt_R25 * logRt_R25 ) ) - 273.15;

// Computing temperature of sensor 2
Vo = analogRead(Thermistor1);
Rt = R1*( 1023.0 / float(Vo) - 1.0 );
logRt_R25 = log(Rt/R25);
T1 = ( 1.0 / (c1 + c2 * logRt_R25 + c3 * logRt_R25 * logRt_R25 + c4 *
logRt_R25 * logRt_R25 * logRt_R25 ) ) - 273.15;

// Computing temperature of sensor 3
Vo = analogRead(Thermistor2);
Rt = R2*( 1023.0 / float(Vo) - 1.0 );
logRt_R25 = log(Rt/R25);
T2 =( 1.0 / (c1 + c2 * logRt_R25 + c3 * logRt_R25 * logRt_R25 + c4 * logRt_R25
* logRt_R25 * logRt_R25 ) ) - 273.15;

// Computing temperature of sensor 4
Vo = analogRead(Thermistor3);
Rt = R3*( 1023.0 / float(Vo) - 1.0 );
logRt_R25 = log(Rt/R25);
T3 = ( 1.0 / (c1 + c2 * logRt_R25 + c3 * logRt_R25 * logRt_R25 + c4 *
logRt_R25 * logRt_R25 * logRt_R25 ) ) - 273.15;

// Computing temperature of sensor 5
Vo = analogRead(Thermistor4);
Rt = R4*( 1023.0 / float(Vo) - 1.0 );
logRt_R25 = log(Rt/R25);
T4 = ( 1.0 / (c1 + c2 * logRt_R25 + c3 * logRt_R25 * logRt_R25 + c4 *
logRt_R25 * logRt_R25 * logRt_R25 ) ) - 273.15;

// The time and temperature readings are sent to the serial port
Serial.print(T0);
Serial.print(" "); Serial.print(T1);
Serial.print(" "); Serial.print(T2);
Serial.print(" "); Serial.print(T3);
Serial.print(" "); Serial.println(T4);
```

```
// A delay of 500ms
delay(500);
}
```

Matlab data logging code

In order to store the measured temperatures as a function of time, a Matlab script was written to log the data received from the Arduino board. The script continuously reads the incoming data, and produces a live-plot of the measured temperatures as a function of time. When the live-plot is closed, all data is saved to a Matlab data file. The complete Matlab script used for this purpose is shown in below.

```
%% DATA interface temperature measurements with Arduino ===================
% This scripts reads data from the Arduino controlled temperature sensor
% array, through the specified serial port. The data is displayed in a live
% plot, and saved to a .mat file after completing the session. Closing the
% live plot terminates the session.
% ========================================================================

%% clear all current data, plots, and command line info
clear all
close all
clc

%% Constants
serialPort = 'COM3';              % define COM port #
baudeRate = 9600;                 % define the transfer rate
plotTitle = 'Serial Data Log';    % plot title
xLabel = 'Elapsed Time (s)';      % x-axis label
yLabel = 'Data';                  % y-axis label
plotGrid = 'on';                  % 'off' to turn off grid
min = 0;                          % set y-min
max = 70;                         % set y-max
scrollWidth = 60;                 % the maximum displayed x-axis width
delay = 0.5;                      % the sample delay
save_name = 'data.mat';           % name of the save file

%% Definition of variables
time = 0;                         % time of measurement
temp1 = 0;                        % measurement of temperature sensor 1
temp2 = 0;                        % measurement of temperature sensor 2
temp3 = 0;                        % measurement of temperature sensor 3
temp4 = 0;                        % measurement of temperature sensor 4
temp5 = 0;                        % measurement of temperature sensor 5
count = 0;                        % the number of measurements

%% Initializing the live plot
plotGraph = plot(time,temp1,time,temp2,time,temp3,time,temp4,time,temp5);
legend('T1','T2','T3','T4','T5','Location','SouthWest');
hold on
title(plotTitle,'FontSize',25);
xlabel(xLabel,'FontSize',15);
ylabel(yLabel,'FontSize',15);
axis([0 10 min max]);
grid(plotGrid);

%% Open Serial COM Port
s = serial(serialPort, 'BaudRate',baudeRate);
disp('Close Plot to End Session');
fopen(s);

%% Loop for reading the data from the serial port
tic                                       % starting time is stored
while ishandle(plotGraph)                 % Loop while Plot is Active
```

```
    dat = fscanf(s,'%f');               % Read Data from Serial as Float

    if(~isempty(dat) && isfloat(dat))   % Check data type
        count = count + 1;              % Update the number of measurements
        time(count) = toc;              % Store elapsed Time
        temp1(count) = dat(1);          % Extract 1st temperature
        temp2(count) = dat(2);          % Extract 2nd temperature
        temp3(count) = dat(3);          % Extract 3rd temperature
        temp4(count) = dat(4);          % Extract 4th temperature
        temp5(count) = dat(5);          % Extract 5th temperature

        % Set plot axis according to Scroll Width
        if(scrollWidth > 0)
            numbers = time > time(count)-scrollWidth;
            plot_time = time(numbers);
            plot(plot_time,temp1(numbers), plot_time,temp2(numbers), ...
                 plot_time,temp3(numbers), plot_time,temp4(numbers), ...
                 plot_time,temp5(numbers));
            axis([time(count)-scrollWidth time(count) min max]);
        else
            set(plotGraph,'XData',time,'YData',temp1);
            axis([0 time(count) min max]);
        end

        % Allow MATLAB to update the plot
        pause(delay);
    end
end

%% Close the serial COM port and delete irrelevant variables
fclose(s);
clear count dat delay max min baudeRate plotGraph plotGrid plotTitle s ...
        scrollWidth serialPort xLabel yLabel numbers plot_time;

%% save data
save(save_name);
disp('Session Terminated...');
```

Appendix C

Image processing for droplet radius and frequency

In order to quantify the droplet generation rate, droplet radius, and droplet velocity, videos were made of the device during operation. These movies were made at the beginning of the meandering channel section, at 15 frames per second, for a duration of approximately 30 seconds. The videos were processed in Matlab, using an algorithm consisting of several steps.

First, the video is split into separate frames, after which droplet positions and radii are measured in each frame. Next, the displacement of each droplet is determined using a matching algorithm. The droplet radii are only recorded when their trajectories cross a fixed line, to prevent double counting of droplets. Additionally ,the displacement vectors are used to estimate the velocity of each droplet. Finally, the generation rate is determined by dividing the total number of droplets by the duration of the analyzed video. The droplet position and radius measurement, matching algorithm, and velocity measurement are discussed in more detail below.

Identifying droplet position and radius

In order to find droplets and measure their radius, a built in Matlab function was used: imfindcircles. This function returns the positions and radii of circles detected in an image, based on a user defined range. This range was defined based on manual measurement of all droplets in the first frame of each video. The droplets are assumed to be spherical, such that the measured radius in 2D is equal to the radius of the 3D droplet. The function could identify droplets in each video frame (Figure C.1 A, B).

The radii obtained from the circle detection function were in pixels, such that conversion to micrometers was necessary. The conversion ratio was obtained by performing several measurements on a photo-lithography mask with known dimensions. The radius in micrometers was then computed by multiplying the radius in pixels with the obtained conversion factor of 1.7857.

Tracking droplets

In order to reliably count droplets and determine their radius over the duration of the video, single beads had to be tracked. This was achieved by a matching algorithm that coupled the droplet positions in frame n with frame n-1. The algorithm was based on finding the nearest neighbor in frame n-1 of each droplet in frame n, assuming that this is the same, but displaced droplet.

This algorithm is accurate only if the droplet displacement between frames is less than one droplet diameter, such that no false matches between neighboring droplets occur. In order to prevent matching errors, two matching conditions were integrated into the algorithm, based on the computed displacement. First, the displacement had to be in the same direction as the flow. Second, the displacement perpendicular to the flow was limited to less than one droplet radius.

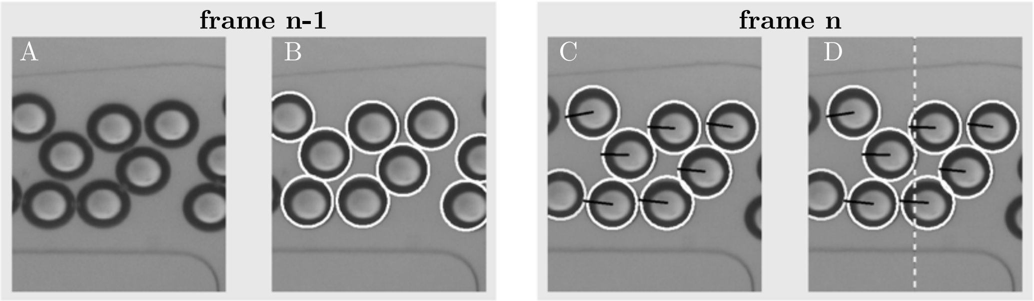

Figure C.1 – A schematic representation of the image processing method. Images are detected in frame n-1 (A), and indicated with a white circle (B). The same is done for the current frame n, and displacement vectors obtained from the matching algorithm are shown in black (C). Droplet velocity and radius is stored when the displacement vector crosses a fixed line (D).

By implementing these conditions, droplets could be successfully matched between frames, such that their displacement vectors could be determined (Figure C.1 C). These vectors were then used to determine when a droplet crossed a fixed line, such that its radius and velocity could be stored (Figure C.1 D).

Quantifying droplet velocity

The velocity of the droplets was estimated using the first order approximation in equation C.1, where v is the absolute velocity, $\vec{x}_n$ the position in the current frame, $\vec{x}_{n-1}$ the position in the previous frame, and Δt the time difference between the two frames.

$$v \approx \frac{|\vec{x}_n - \vec{x}_{n-1}|}{\Delta t} \tag{C.1}$$

Matlab code

The Matlab code for analyzing a single video can be found below.

```
%% Image processing code for droplet radius, generation rate, and velocity
% This code converts the avi video with the name FILENAME into separate tif
% frames, and measures the radius, generation rate, and velocity of the
% droplets.
% ==========================================================================

%% clear all current data, plots, and command line info
clear all
close all
clc

%% Constants
FILENAME = 'video_filename';        % the avi video filename
dt = 1/15;                          % the time difference between frames
search_radii = [13 30];             % the radius range for circle detection
circle_treshhold = 0.1;             % the threshold for circle detection
crop_array = [200 1 300 480];       % image cropping array

%% Creating image filter
f_type = 'gaussian';
f_size = [2 2];
f_sigma = 1/2;
filter = fspecial(f_type,f_size,f_sigma);

%% Determine file and save name
filename = strcat(FILENAME,'.avi');                 % the current filename
```

```
savename = strcat(FILENAME,'_processed.mat');       % the savename

%% converting video to separate frames
fprintf('Converting video to separate frames\n');
obj = VideoReader(filename);    % create the multimedia reader object
vid = read(obj);                % read the video that obj refers to
n_frames = obj.NumberOfFrames;  % retrieve the number of frames in video

for j = 1 : n_frames
    % For all frames: write the frame to a tif file called frame-#.tif,
    % where # is the frame number.
    imwrite(vid(:,:,:,j),strcat('frame-',num2str(j),'.tif'));
end

%% finding circles in the first frame
I1 = imread('frame-1.tif');             % read the image
I1 = rgb2gray(I1);                      % convert to grayscale
I1 = imcomplement(I1);                  % make image complementary
I1 = imcrop(I1,crop_array);             % crop the image
I1 = imadjust(I1,stretchlim(I1),[]);    % adjust contrast
I2 = imfilter(I1,filter,'same');        % filter image

% finding circles
[centers_old, radii_old] = imfindcircles(I2,search_radii, ...
                                         'EdgeThreshold',circle_treshhold);

%% Analyzing the complete video
N = 0;          % the number of beads is set to 0
Rsum = 0;       % the sum of all radii is set to 0
R_arr = [];     % the radius storage array is initialized
vel = [];       % the velocity storage array is initialized
xpos = [];      % the position storage array is initialized

for j = 2:n_frames
    framename = strcat('frame-', num2str(j), '.tif'); % create filename
    I1 = imread(framename);                 % read the image
    I1 = rgb2gray(I1);                      % convert to grayscale
    I1 = imcomplement(I1);                  % make image complementary
    I1 = imcrop(I1,crop_array);             % crop the image
    I1 = imadjust(I1,stretchlim(I1),[]);    % adjust contrast
    I2 = imfilter(I1,filter,'same');        % filter image

    % find circles
    [centers, radii, metric] = imfindcircles(I2,search_radii,...
                                         'EdgeThreshold',circle_treshhold);

    % matching algorithm: For all detected droplets in the current frame
    for k = 1:length(radii)

        % Only droplets that are over one diameter away from the limits of
        % the image are analyzed
        if centers(k,2) >= 2*radii(k) && centers(k,2) <= crop_array(4) - 2*radii(k)
            dist_old = 1e6;     % the distance is set to a huga value
            match = 0;          % there is no match

            % For all detected droplets in the previous frame
            for l = 1:length(radii_old)
                vec = centers(k,:)-centers_old(l,:);  % displacement vector
                dist = norm(vec,2);                   % total displacement

                % If this droplet is closer than the previous match, the
                % displacement is in positive direction, and the absolute
                % displacement perpendicular to the flow is less than one
                % droplet radius:
                if dist < dist_old && vec(2) > 0 && abs(vec(1)) < radii(k)
                    match = 1;           % the match is stored
                    dist_old = dist;     % the distance is updated
```

```
                end
            end

            % If a match is found
            if match ~= 0;

                % If the droplet passes the fixed line at 240 pixels
                if centers(k,2) > 240 && centers_old(match,2) < 240
                    N = N + 1;                  % the droplet is counted
                    Rsum = Rsum + radii(k);     % the radius is added
                    R_arr = [R_arr radii(k)];   % the radius is stored

                    % The displacement fro the match is computed again
                    vec = centers(k,:)-centers_old(match,:);
                    dist = norm(vec,2);

                    vel = [vel dist/dt];        % velocity is computed
                    xpos = [xpos centers(k,1)]; % the position is stored
                end
            end
        end
    end

    % Storing the data from the current frame for the next iteration
    centers_old = centers;
    radii_old = radii;
end

%% Computing final values
freq = N / (n_frames*dt);   % Droplet generation rate
Rmean = Rsum/N;             % Mean radius
R_std = std(R_arr);         % Radius standard deviation

%% Saving all relevant data
save(savename,'N','R_arr','freq','Rmean','R_std','n_frames','vel','xpos');

%% Deleting all stored tif frames
delete *.tif
```